Fatigue and Fracture of Medical Metallic Materials and Devices

M. R. Mitchell and K. L. Jerina
Editors

STP 1481

ASTM INTERNATIONAL
Standards Worldwide

STP 1481

Fatigue and Fracture of Medical Metallic Materials and Devices

M. R. Mitchell and K. L. Jerina,
editors

ASTM Stock Number: STP1481

ASTM
100 Barr Harbor Drive
PO Box C700
West Conshohocken, PA 19428-2959

Printed in the U.S.A.

ISBN: 978-0-80314511-5

Photocopy Rights

Peer Review Policy

Each paper published in this volume was evaluated by two peer reviewers and at least one editor. The authors addressed all of the reviewers' comments to the satisfaction of both the technical editor(s) and the ASTM International Committee on Publications.

The quality of the papers in this publication reflects not only the obvious efforts of the authors and the technical editor(s), but also the work of the peer reviewers. In keeping with long-standing publication practices, ASTM International maintains the anonymity of the peer reviewers. The ASTM International Committee on Publications acknowledges with appreciation their dedication and contribution of time and effort on behalf of ASTM International.

Printed in USA
September 2007

Foreword

This particular ASTM International publication contains research manuscripts from the First Symposium — Fatigue and Fracture of Medical Metallic Materials and Devices that was sponsored by ASTM Committees E08 on Fatigue and Fracture and F04 on Medical Devices held in Dallas, TX, November, 2005. It was the intent of this conference to bring together technical experts in both disciplines, in order to initiate a dialogue between the two groups that would further our knowledge and understanding of the cyclic deformation, of most specifically, nitinol-based medical devices and the physical environment in which they are expected to survive for considerable periods of time. The ultimate goal of this interaction is intended to (1) define the environments (i.e. duty cycle deformation-time histories) in body-specific locations such as the superficial femoral artery, carotid, abdominal and thoracic arteries (2) develop constitutive expressions for the deformation response of nitinol via specific test methodologies and data analyses (3) develop the appropriate mechanics analyses for cumulative damage calculations and to ultimately (4) ascertain the fatigue lifetime of medical devices in the human body. To this end, standards must be developed to define the subject matter listed above.

Contents

Overview

A conference held in Dallas, TX in November of 2005 addressed the unique thermal and mechanical properties of shape memory alloys (SMA's) and metallic medical materials and devices. Although the conference focused much attention on nitinol-based technologies, several other metallic medical materials and devices are included in the conference publications. The principle focus was on nitinol since these unique alloys offer the designer new dimensions in controlling the shape of devices used in medical and many structural applications. Shape memory devices such as valves, actuators, clutches and gaskets are proposed for monitoring units, drive systems and repair schemes. Biocompatible implanted medical devices rely on the hyperelastic response of these unique materials. Relative to conventional materials, little is known about the fatigue, fracture and deformation behavior of shape memory alloys particularly in a contemporary sense for fatigue lifetime predictions.

The primary intent of the conference was to provide a firm basis of fundamental mechanical response for development of ASTM standard procedures for determination of the constitutive relationships, the deformation behavior, the fatigue lifetime response and fracture behavior of metallic shape memory alloys. Also, the conference provided a forum for dissemination of knowledge and research on methodologies in the developments of constitutive models for fatigue and fracture behavior of metallic shape memory alloys. Such understanding and standards development are essential for determination of the *in situ* lifetime assessment of self-expanding medical devices that employ these unusual metallic materials. This ASTM STP features the work of knowledgeable and distinguished researchers in the emerging field of metallic shape memory alloys.

The contents of this STP elucidate on such topics as the metallurgical basics of martensitic transformations and fatigue behavior of nitinol as well as the influence of phase transformations on the mechanical properties and the thermoelastic transformational behavior of these alloys. Additional insight is provided on the mechanics and fatigue of stents as influenced by arterial deformations and a verification of the strain level determination for compressive-compressive response of nitinol. To improve recovery stress and recovery strain capabilities of of nitinol it is necessary to facilitate deformation by martensitic transformational mechanisms while avoiding a risk of plastic deformation. Included herein is a manuscript illustrating that such goals can be effectively reached by judicious thermal-mechanical processing of this alloy. Also included herein is a description of a rotating-bending test technique for rapid determination of the completely reversed fatigue response of thin nitinol wires.

Additional information is provided on low plasticity burnishing to improve the fatigue performance of Ti-6Al-4V femoral hip stems, lessons learned from an existing heart valve design with failure rates that have been followed for over 20 years and a comparison of the corrosion-fatigue characteristics of Mn-Cr-Mo and Cr-Ni-Mn stainless steels.

Because of the considerable audience response to this topical matter and the interest of both ASTM Committees E08 on Fatigue and Fracture and F04 on Medical Devices, a Second Symposium on the Fatigue and Fracture of Metallic Medical Materials and Devices is being held in Denver, CO in May 2008 with co-sponsorship of SMST (Shape Memory and Superelastic Technologies). It is anticipated that with such co-sponsorship within ASTM as well as with SMST, the

premier professional societal group involved in nitinol research and dissemination of technical information, we will be able to develop meaningful and much needed standards for proper testing, design and lifetime predictions for these important medical materials.

Dr. M. R. Mitchell,
Northern Arizona University,
Flagstaff, Arizona

Prof. Kenneth L. Jerina,
Washington University at St. Louis,
St. Louis, Missouri

SECTION I: PROCESSING, PROPERTIES AND ENVIRONMENT

Journal of ASTM International, Vol. 4, No. 7
Paper ID JAI100645
Available online at www.astm.org

P. H. Adler,[1] *J. Allen,*[2] *J. Lessar,*[3] *and R. Francis*[3]

Martensite Transformations and Fatigue Behavior of Nitinol

ABSTRACT: In addition to excellent biocompatibility and corrosion resistance, the unique flow behavior of NiTi pseudo-elastic alloys renders them ideally suited for several medical device applications utilizing minimally invasive technologies. For example, self-expanding stents are indicated chronic therapies for treatment of a variety of vascular diseases. Long-term device integrity is thus critical with the FDA recommending a minimum 10-year life. Historically, the majority of published fatigue data on NiTi alloys have been generated under strain-controlled conditions using wire or single-diamond cell samples designed to replicate the behavior of the repetitive unit within a stent. Resulting data are then presented on modified Goodman or Soderberg diagrams in order to define regions of acceptable device life. Consistent with their unusual monotonic flow characteristics these alloys are found to exhibit unique cyclic behavior in fatigue: published data clearly demonstrate that increasing mean strain often increases high-cycle fatigue life. This anomalous behavior is generally attributed to any of a number of possible microstructural or mechanical effects associated with the reversible stress-assisted austenite-to-martensite phase transformation. Although the majority of published work has focused on these macroscopic properties in order to characterize and adequately define device life, various efforts are currently underway to better understand the more fundamental metallurgical and mechanical aspects controlling fatigue life in this alloy. Such studies include crack initiation and propagation rates, determining the roles of absolute and relative inherent flow behavior of the transforming structures, mechanical instabilities resulting from the heterogeneous nature of the transformation, latent heat effects during cyclic transformation, as well as the effects of testing frequency, crystallographic texture, grain-shape anisotropy, and stress-state on fatigue life. A review of existing literature delineating these behaviors and current efforts is presented in light of known beneficial effects of transformation plasticity and toughening in enhancing fatigue and fracture properties of a variety of metallic and nonmetallic materials.

KEYWORDS: Nitinol, medical device, fatigue, stent, superelasticity, pseudoelasticity, shape-memory, transformation plasticity, transformation toughening

Introduction

The expanding use of NiTi, i.e., Nitinol, as a preferred material platform for disposable as well as implanted medical devices has prompted a growing interest in the long-term fatigue behavior of this unusual material. While Nitinol's unique nonlinear and highly reversible flow characteristics make this a material well suited for minimally invasive technologies, delivery protocols inherently subject devices to a variety of deformations resulting from initial catheter loading, deployment, and placement procedures which may adversely affect fatigue life. Once placed, devices such as stents experience *in-vivo* diametral fatigue cycling encountered in normal physiologic environments comprising 3–10 % vascular dilations [1] associated with normal sinus rhythms, as well as a variety of other deformations experienced in anatomical locations subject to chronic flexing, bending, or buckling such as under the inguinal ligament, within the femoropopliteal artery or coronary vessels as a result of the systolic cardiac expansions. Designed stent oversizing ensures maintenance of a chronic outward force (COF) for adequate vessel scaffolding as described by Duerig and Tolomeo [1], and mitigates migratory concerns by imposing nonzero operational mean strains which, fortuitously, a number of studies cite as the indicated regime for obtaining superior high-cycle fatigue life in the pseudoelastic condition [2–4].

Manuscript received May 17, 2006; accepted for publication May 6, 2007; published online July 2007. Presented at ASTM Symposium on Fatigue and Fracture of Medical Metallic Materials and Devices on 7–11 November 2005 in Dallas, TX; M. R. Mitchell and K. L. Jerina, Guest Editors.

[1] Senior Principal Scientist, Medtronic, 3576 Unocal Place, Santa Rosa, CA 95403.
[2] Senior Product Development Manager, Medtronic, 3576 Unocal Place, Santa Rosa, CA 95403.
[3] Distinguished Scientist and Principal Scientist, respectively, Medtronic, 710 Medtronic Parkway, Minneapolis, MN 55432.

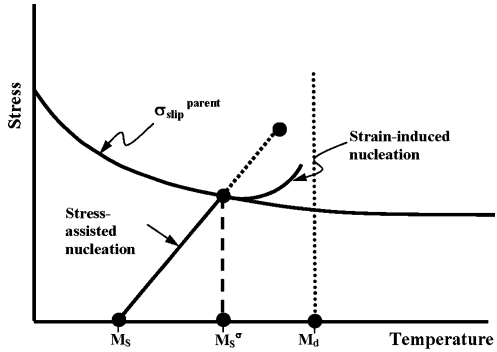

FIG. 1—*Schematic representation of stress-temperature relationship for NiTi.*

We herein present a brief review of existing literature delineating these behaviors and current efforts in the context of known beneficial effects of transformation plasticity and transformation toughening in enhancing fatigue and fracture properties of a variety of metallic and nonmetallic materials. Initially, a brief review of classic martensite mechanistic theory is presented to (re-) familiarize the reader with these important concepts, especially as they are becoming more relevant in understanding the fatigue behavior of Nitinol.

General Concepts in Martensitic Transformations

Nitinol is typically used in the pseudoelastic condition for medical device implants. In this state the material consists of austenite in a B2 crystal structure with various Ni-rich precipitates dispersed throughout the lattice as a result of device processing. The B2 structure is thermodynamically metastable such that lowering the temperature of a sample will result in a martensitic phase transformation to the $B19'$ monoclinic structure at the temperature labeled M_s in Fig. 1. Application of stress results in an increase in the transformation temperature for $M_s < T < M_s^\sigma$ as shown by the solid line marked "stress-assisted nucleation." The observed linear positive temperature dependence of the stress to nucleate martensite in uniaxial tension has been termed the "stress rate" [5] and obeys a modified Clausius-Clapeyron relation:

$$d\sigma/dT = -\Delta H/T\varepsilon \tag{1}$$

with ΔH=enthalpy change and ε=resolved uniaxial strain ($\approx$8 %) associated with the transformation. Stress-temperature measurements of NiTi binary alloys indicate a stress rate $\approx$6 MPa/°C in uniaxial tension [6].

Uniaxial tensile curves of Nitinol tested in the pseudoelastic condition, i.e., $A_f < T < M_s^\sigma$, loaded to 8 % strain, unloaded to zero stress, then reloaded to failure are shown in Fig. 2. A_f is the temperature at which the last volume of martensite reverts to austenite on heating a stress-free sample. On reaching σ_s martensite plates nucleate and grow rapidly until impinging an obstacle such as a grain boundary. Although there are typically 24 possible crystallographic martensitic variants, the applied stress favors those which permit maximum elongation in the tensile-axis direction. Thus, martensite is fully formed and stress-oriented at the end of the upper plateau in Fig. 2 corresponding to about 6 % uniaxial strain for Nitinol.

In thermoelastic alloys, such as Nitinol, the interfacial stress fields of an advancing plate are accommodated primarily by increasing stored elastic strain energy in the parent lattice. As such, the interface remains glissile taking on crystallographically-reversible features so that on unloading the imposed shape change is recovered as indicated by the lower plateau in Fig. 2. A small amount of concurrent slip deformation in the parent lattice results in a small permanent strain typically no more than about 0.5 % after unloading to zero stress. Hysteresis arises from the difference between the stresses σ_s and σ_r required for martensitic nucleation and reversion. Additional friction stress may be required to drive interfacial

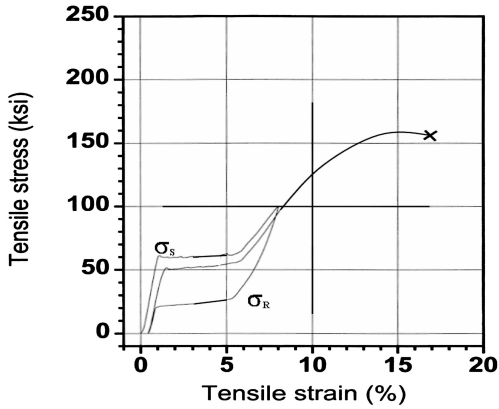

FIG. 2—*Typical load-unload-reload stress-strain curves of pseudoelastic Nitinol.*

motion increasing the hysteresis. For example, sufficient accommodation by slip results in interfacial pinning requiring re-nucleation of the austenite as occurs in nonthermoelastic alloys.

The reloading curve in Fig. 2 shows a decrease in the stress required for renucleation of the martensite due to formation of preferred variants during initial loading. Stress-assisted transformation continues with increasing strain until saturation occurs in the parent lattice after which deformation in the martensitic structure occurs mainly by traditional slip mechanisms giving rise to the power-law hardening behavior shown in Fig. 2. Tensile fracture strains in pseudoelastic Nitinol typically range from 10–20 %. The effects of a mechanically-induced martensitic transformation distort the stress-strain curve to an upward curving shape, as seen in the loading plateau in Fig. 2, approximating ideal exponential hardening behavior which imparts maximum stability of the macroscopic flow behavior. As a result, Nitinol samples pulled in tension typically show little "necking."

It is commonly assumed that no martensitic transformation occurs in NiTi alloys above the temperature labeled M_s^σ [6] in Fig. 1 and therefore M_s^σ is taken to be equivalent to the M_d temperature [7] in these alloys. However, there is some evidence [8,9] of further transformation in NiTi alloys above M_s^σ, and as such we include the possibility of "strain-induced" transformations in Fig. 1 as is traditionally described for other materials undergoing mechanically-induced martensitic transformations [7]. M_d is defined as the temperature above which the chemical driving force for transformation becomes so small that martensitic nucleation cannot occur even with prior plastic deformation. The reader is referred to Refs. [7,10,11] for more detailed descriptions of fundamentals aspects of martensitic transformations in both thermoelastic and nonthermoelastic materials.

Cyclic Plasticity Studies

In 1979, Melton and Mercier [12] published studies outlining crack growth rates and fatigue life of fully annealed NiTi alloys with differing thermodynamic stabilities. Room-temperature mechanical property testing was performed on alloys with M_s values ranging from −30°C to +70°C and corresponding microstructures ranging from partially or fully martensitic ($M_s > +20$°C) to fully austenitic.

Stress-controlled, R ($=\sigma_{min}/\sigma_{max}$)$=-1$, cyclic flow curves for the −30°C sample are shown in Fig. 3. The left curve shows the first cycle and the right shows the flow curve after nine cycles. The stress to nucleate martensite during initial loading is about 350 MPa consistent with that predicted by the stress-rate for Nitinol for the measured M_s of this alloy. During the first cycle deformation occurs by stress-assisted martensitic transformation with interfacial stress fields plastically, not elastically, accommodated due to the relatively low strength of the fully annealed austenite. From the first cycle the increased defect density pins interfaces kinetically stabilizing the martensitic structure so that virtually no strain recovery is seen on unloading. With continued cycling the stabilized martensite structure work hardens thus promoting deformation by more reversible processes such as mechanical twinning or variant reorientation which together

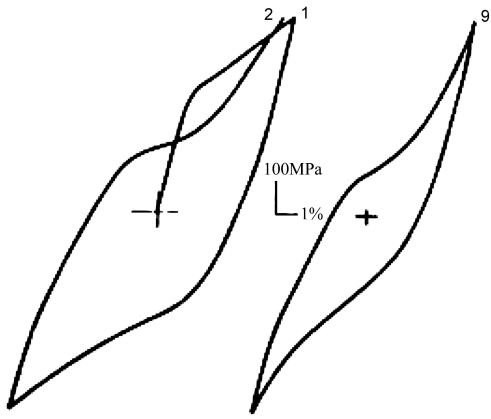

FIG. 3—*Stress-controlled flow curves for fully annealed Nitinol with $M_s = -30°C$. Melton and Mercier [12].*

with reduced stress for transformation results in the decreased hysteresis seen in the right curve of Fig. 3.

Fatigue crack-growth rate studies were also performed on two alloys with $M_s = +20°C$ and $+47°C$ with $R < 0.1$ at a testing frequency of 2.3 Hz under displacement-controlled conditions. Despite one alloy being fully martensitic at room temperature (+47°C) and the other primarily austenitic (+20°C), they found the fatigue crack growth rates for both alloys to be about 10^{-10} m/cycle with a fatigue threshold $\Delta K_{th} = 2$ MPa$\sqrt{\text{m}}$. It might be expected that the different thermodynamic stabilities of the two alloys tested would result in different crack propagation rates. However, at room temperature the chemical driving force for transformation in the austenitic alloy is nearly sufficient to nucleate the martensite so that the stress to induce transformation will be very low in this alloy. Once nucleated, the martensite is kinetically pinned as described above so that within a very few cycles both alloys will essentially have the same microstructure and operative deformation mechanisms. As such, it is not surprising that both alloys exhibit similar crack growth rates.

In 1989, Zadno et al. [13] performed low-cycle fatigue testing on wires in solution treated and aged, cold worked and aged, and as-cold worked conditions as outlined in Table 1. They pulled samples in tension to 4 % strain then unloaded and corrected for permanent strain so that each cycle was pulled to a total 4 % strain. Essentially this comprises a strain-controlled fatigue test at 2 % mean strain with an alternating strain amplitude of 2 % although it appears they unloaded to a zero stress, not zero strain, condition with each cycle.

Cyclic stress-strain curves are shown in Fig. 4 for these worked and aged conditions. Compared with the flow curves shown in Fig. 3 from Melton and Mercier's [12] work on fully annealed material, the results shown in Fig. 4 serve to illustrate the differences in flow behavior of Nitinol in which the parent austenite lattice has been strengthened sufficiently to allow elastic accommodation of interfacial stresses and reversibility of the majority of the imposed deformation on unloading.

In Condition 1 (Fig. 4(*a*)) the austenitic matrix is strengthened solely by a fine dispersion of precipitates resulting from the low temperature aging at 325°C for 30 min after solution treatment. Strengthening in Conditions 2 and 3 (Figs. 4(*b*) and 4(*c*)) is obtained by cold working followed by aging at 600°C for

TABLE 1—*Thermomechanical treatments and transformation characteristics of wires tested by Zadno et al. [13].*

Figure	Condition	M_s[a]	A_s[a]	R_s	σ_{slip}[b],MPa
4(*a*)	1. Sol'n Treat; Aged 325°C for 30 min	−17°C	30°C	32°C	737
4(*b*)	2. 40 % CW; Aged 600°C for 2 min	−32°C	11°C	0°C	850
4(*c*)	3. 40 % CW; Aged 375°C for 30 min	−75°C	−3°C	50°C	1360
4(*d*)	4. 40 % Cold Work	…	…	…	900

[a]M_s and A_s were obtained with 140 MPa applied stress.
[b]Austenitic yield strength.

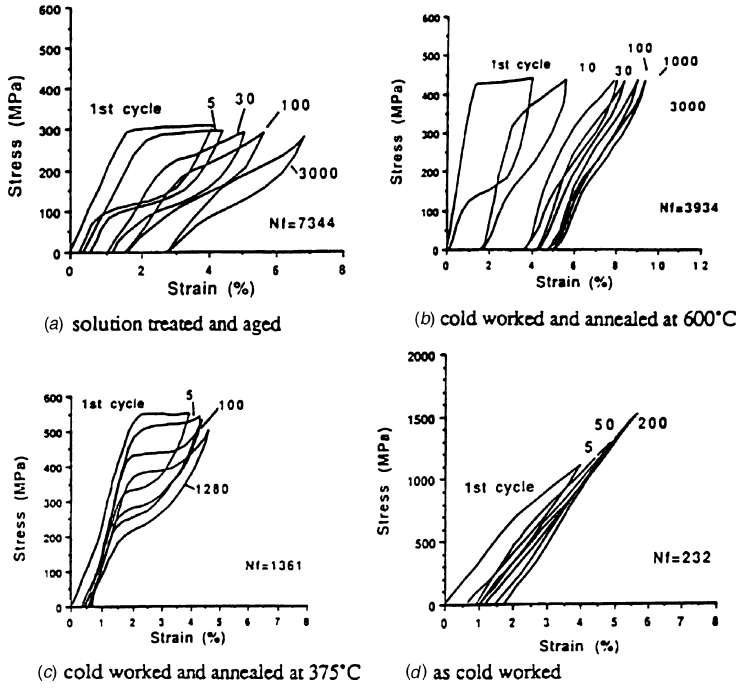

FIG. 4—*Cyclic flow curves from Zadno et al. [13].*

2 min and 375°C for 30 min, respectively. While these treatments result in different amounts of residual cold work and precipitation, in all three cases significant recovery on unloading occurs from the first cycle compared to the large permanent strains seen in Melton and Mercier's work [12].

The precipitates formed in Nitinol alloys used for medical devices are Ni-rich with stoichiometries such as $Ti_{11}Ni_{14}$, Ti_2Ni_3, and $TiNi_3$ [14]. These precipitates preferentially deplete the surrounding B2 lattice of Ni increasing the $B2/R \leftrightarrow B19'$ martensitic transformation temperatures. In general agreement with the stress rate for Nitinol, the data in Table 1 and Figure 4 show higher transformation temperatures correlate with decreased plateau stress levels and increased fatigue life, N_f, at a constant test temperature.

Other than strengthening the austenite lattice, increasing defect density during fatigue cycling affects the stress-assisted martensitic transformation and cyclic flow behavior in three important ways: the stress to nucleate martensite decreases due to stress-biasing of preferred variants, incrementally higher stresses are required to propagate an existing interface through the increasingly dislocated structure resulting in correspondingly higher "monotonic" work-hardening rates, and the higher slip strength of the work-hardened lattice promotes deformation by more reversible mechanisms. The combined effects are to decrease the hysteresis with continued cycling as seen in Figs. 4(*a*)–4(*c*). Figure 4(*d*) shows the cyclic stress strain curves after 40 % cold working with no further heat treating. In this condition the material consists of cold-worked martensite so that on loading deformation is primarily by twin boundary motion or variant reorientation both of which are reversible on unloading.

Despite the large recovery strains seen in all samples tested, the flow curves of samples processed in Conditions 1 and 2 (Figs. 4(*a*) and 4(*b*)) are clearly less stable than that of the sample processed in Condition 3 (Fig. 4(*c*)) exhibiting extensive strain ratcheting and significant hysteresis shape changes with continued cycling. The greater flow stability of the sample shown in Fig. 4(*c*) is likely the result of the nearly 70 % higher flow strength of the stabilized B2 structure resulting from prior cold working and the relatively low aging temperature compared with the lower B2 strengths of samples processed at higher temperatures in Conditions 1 and 2, as shown in Table 1. The higher strength of the B2 structure resists

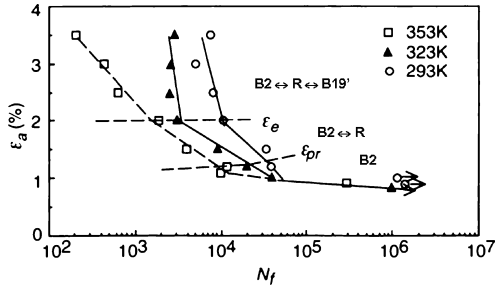

FIG. 5—*ε_a versus N_f curves from Kim and Miyazaki [15].*

accommodation slip imparting greater flow stability and likely longer fatigue life in the pseudoelastic condition used in medical devices.

Fatigue Failure Studies

In 1997 Kim and Miyazaki [15] published the results of a strain-controlled fatigue study on Ti-50.9a/oNi wires using a rotating beam apparatus which inherently imparts zero mean strain test conditions. After 30 % cold work, wires were annealed at 400°C for 60 min followed by water quenching. Measured transformation temperatures were M_s=−50°C (223 K), M_f<−103°C (170 K), A_s=−15°C (258 K), A_f =+10°C (283 K), R^*=37°C (310 K) and RA^*=40°C (313 K), where R^* and RA^* are the R-phase forward and reverse transformation peak temperatures. Specimens were mechanically polished followed by electropolishing. This is thought to be the first effort in which fatigue life of electropolished samples of Nitinol were studied. Wires were bent to induce outer-fiber (alternating) strains up to 3.5 % then fatigued at a test frequency of 6.67 Hz in controlled temperature baths at 20°C (293 K), 50°C (323 K), and 80°C (353 K).

It should be noted that the R-phase is a rhombohedral distortion of the B2 structure with B2→R transformation often occurring prior to transformation to the B19′ structure in worked and aged Nitinol alloys. As with the direct B2→B19′ martensitic transformation, the B2→R transformation can occur under the action of an applied stress albeit with less affect on the flow curve [15].

The results of Kim and Miyazaki's [15] strain-controlled fatigue tests are shown in Fig. 5. This figure shows three distinct regions of linear fatigue behavior separated by two strain levels labeled ε_{pr} and ε_e corresponding to the proportional limit, and the strain at which macroscopic yielding via stress-assisted martensitic transformation occurs in monotonic tensile loading, respectively. These three regions correspond to cyclic deformation by B2↔R↔B19′ at $\varepsilon_a > \varepsilon_e$, B2↔R at $\varepsilon_{pr} < \varepsilon_a < \varepsilon_e$, and linear elastic deformation in the B2 structure at $\varepsilon_a < \varepsilon_{pr}$. At $\varepsilon_a > \varepsilon_e$, the fatigue life at the two higher test temperatures is relatively insensitive to strain amplitude. As the test at 20°C (293 K) is below RA^*, cyclic deformation at $\varepsilon > \varepsilon_e$ occurs by R↔B19′ and the fatigue life exhibits a strong dependence on strain amplitude. As discussed elsewhere in this volume, the B2→R transformation can have a significant impact on the fatigue life of Nitinol when tested at zero mean strain and alternating strain levels below that at which the R →B19′ transformation occurs, i.e., ε_e.

Perhaps most important from Kim and Miyazaki's work is the notable increase in low-cycle ($N < 10^5$ cycles) fatigue life with decreased test temperatures seen in Fig. 5. This behavior is attributable to the positive-temperature dependence of the stress to nucleate martensite in the stress-assisted regime as depicted in Fig. 1. This unique behavior results in decreased operational stress during fatigue cycling at lower test temperatures.

Over the past six years or so the fairly dramatic increase in published literature addressing high-cycle fatigue life of Nitinol devices is a testament to the growing importance of this unique material in medical device applications. Most of these studies involve strain- or displacement-controlled testing as this is thought to best represent the in-vivo situation. In contrast to more traditional hourglass-shaped or wire samples used in fatigue studies in which stresses and strains are easily calculated, finite-element analytical (FEA) techniques are required to determine operational conditions in current test paradigms as sample

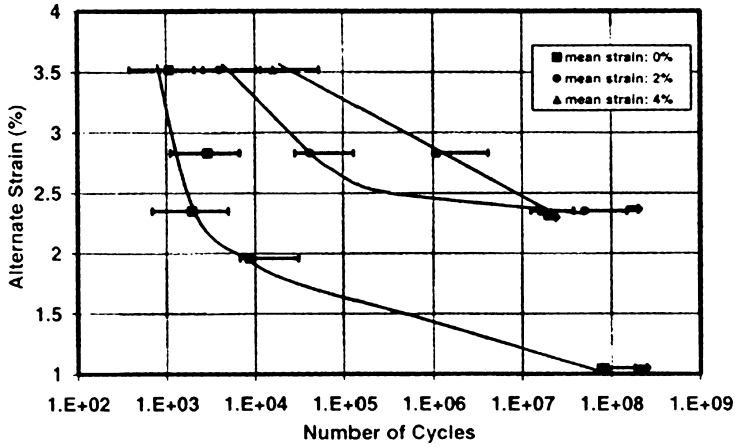

FIG. 6—*Results of strain-controlled fatigue testing, Harrison and Lin [2].*

geometries comprise V- or diamond-shaped components reflective of the basic repetitive stent unit subject to bending. Such techniques rely on accurate constitutive modeling for meaningful representations of in-vivo as well as in-vitro operating conditions. At present, constitutive input for FEA modeling of Nitinol consists of single-cycle loading and unloading curves as shown in Fig. 2–4 for fully annealed material and pseudoelastic Nitinol, respectively, clearly depict and mechanical hysteresis significantly changes within a relatively small number of reversals. The evolutionary nature of the hysteresis likely plays an important role in low and high-cycle fitigue of Nitinol and must be considered in fatigue studies. Numerous efforts are currently attempting to address these issues as well.

Building on early fatigue studies performed on relatively low-strength B2 structures resulting from either solution-treated and aged, or, cold worked followed by extensively long aging treatments, current processing of Nitinol wire or tubing for medical device applications involves cold working and short-time aging resulting in higher strength B2 structures capable of resisting cyclic slip deformation and exhibiting longer fatigue life. Although a number of very fine works on fatigue life of Nitinol have been published we confine our review to four recent studies deemed representative of current efforts.

In 2000, Harrison and Lin [2] published one of the first studies delineating the fatigue life of electropolished V-shaped samples and presenting data on a life diagram in terms of alternating, ε_a, and compressive mean strains, ε_m. Samples were fatigued to failure or 10^8 cycles at a frequency of 45 Hz. Results of their strain-controlled fatigue tests to 3.5 % alternating strain at ε_m=0, 2, and 4 % are shown in Fig. 6.

Consistent with most materials, the data in Fig. 6 exhibit decreased fatigue life with increasing strain amplitude. In contrast, however, to most engineering materials, the data in Fig. 6 show increased fatigue life as mean strain is increased from 0 to 2 %. The data at 4 % mean strain suggest fatigue life continues to increase although the few data presented exhibit significant scatter. Harrison and Lin attribute the increased fatigue life with mean strain to the reduced stress amplitude associated with cycling an existing (reversible) austenite-martensite interface between two fixed strain levels in tension, i.e., $\Delta\sigma=\sigma_s-\sigma_f$, compared to that required for re-nucleation during cycling between imposed tensile and compressive strain limits, i.e., $\Delta\sigma=2\sigma_s$, as schematically depicted in Fig. 7. They also note the decreased hysteresis with cycling will benefit fatigue by reduced internal friction and minimizing residual stresses.

Based on the data at 10^8 cycles Harrison and Lin construct the infinite life diagram shown in Fig. 8. The solid line in this figure represents the fatigue life of Nitinol as described by a strain modification of the traditional stress-based Goodman equation:

$$\varepsilon_a/\varepsilon_{en} + \varepsilon_m/\varepsilon_{ult} = 1 \tag{2}$$

with ε_{en}=endurance limit ($\approx$1 %) at ε_m=0, and, ε_{ult}=the strain at the ultimate tensile stress ($\approx$12 %). The dashed line connecting three of the data points from Fig. 8 shows the fatigue life of the

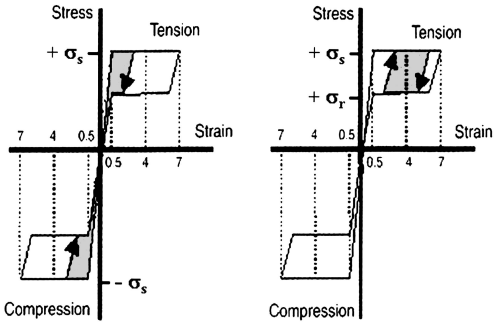

FIG. 7—*Schematic diagram depicting variation in stress amplitude at* $\varepsilon_m = 0$ *(left) and* $\varepsilon_m > 0$ *(right), Harrison and Lin [2].*

Nitinol samples tested is greater than predicted by Eq. 2, with a maximum endurance limit, ε_a, of 2.4 % at 10^8 cycles occurring at 2 % mean strain. As discussed later, the endurance limits at the mean strains tested by Harrison and Lin are significantly higher than those reported in similar studies of polished Nitinol components.

Pelton et al. [3] published results of displacement-controlled fatigue testing of electropolished diamond-shaped samples at 37°C cycled at 50 Hz in 2004. The measured A_f values of samples ranged from 26–32°C. Mean strains up to 4 % as determined by FEA were tested with alternating strains ranging from 0 to 3 %. The open squares in Fig. 9 show ε_a versus cycle count for samples fatigued to failure or run-out (10^7 cycles) at zero-mean strain up to 3 % alternating strain. Filled squares and triangles show non-zero mean strain data tested at alternating strains ranging from 0.2 to 1.5 %. No run-out data are shown for nonzero mean strain conditions. The trend line drawn through low-cycle fatigue data ($N < 10^5$ cycles) indicates a Coffin-Manson exponent of −0.41. Data labeled as "compression" (filled triangles) in Fig. 9 were obtained by "pushing" on the apices, but the stress state of the area analyzed was tensile in nature.

In the low-cycle regime, $N_f < 10^5$ cycles, the Pelton et al. data shown in Fig. 9 is in good agreement with the data from Harrison and Lin [2]. However, the data at zero mean strain to 10^7 cycles show an endurance limit of about 0.4 % strain which is significantly less than that determined by Harrison and Lin of 1.05 %. Both axes are plotted as strain amplitude, i.e., one-half the peak-to-peak, or range, of strains tested. The source of the discrepancy in fatigue limits is not clear although it may be related to processing, analytical, or design differences between the two stent configurations. For example, different apex radii may act as stress-risers: notched samples typically exhibit reduced endurance limits compared with un-

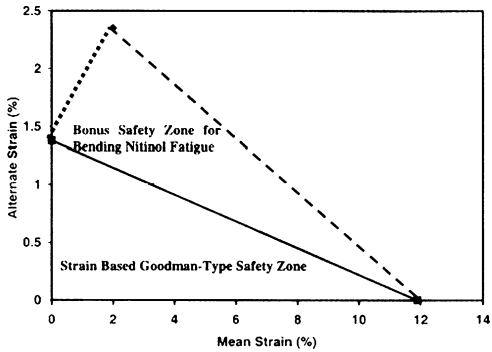

FIG. 8—*Estimated life diagram to* 10^8 *cycles from Harrison and Lin [2]. Note* ε_a *at* $\varepsilon_m = 0$ *should be 1.05 %.*

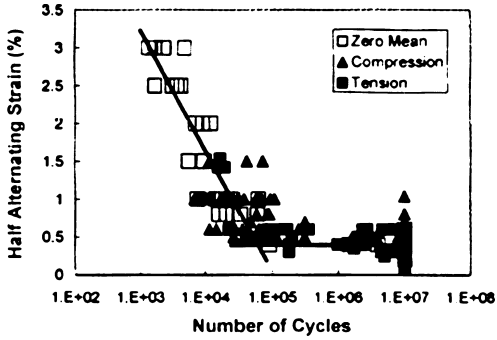

FIG. 9—*Results of strain-controlled fatigue testing on diamond-shaped samples [3].*

notched samples of the same material. Of course, surface conditions may play a role as high-cycle fatigue life is typically controlled by nucleation of cracks rather than propagation.

Figure 10 shows the constant life diagram constructed from the data in Fig. 9 as well as run-out samples tested in the nonzero mean strain conditions. As with data labeled "compressive" in Fig. 9, the axes labeled as "compression" in Figs. 10 and 11 should actually be denoted "push" as they refer not to the actual stress or strain state in the metal but rather that the apices of the test sample were being pushed to induce tensile stresses.

The trends in Fig. 10 are generally consistent with those of Harrison and Lin [2] for mean strains up to 2 % showing an increase of fatigue life with mean strain, although as stated earlier the Pelton et al. endurance limits for all mean strains are less than half those of the Harrison and Lin work. Beyond 2 % mean strain Pelton et al. show fatigue life continues increasing whereas Harrison and Lin indicate optimal fatigue life occurs at 2 % mean strain although there are relatively few data points beyond 2 % mean strain. Pelton et al. ascribe the increased fatigue life at mean strains greater than 1 % to stress-induced martensite as the active deformation mechanism citing the study by Kim and Miyazaki [15] that shows higher fatigue life in martensite than in austenite in identical testing conditions. They also refer to fracture mechanics analyses [16] that show lower crack growth rates in martensite than austenite.

Using a monotonic flow curve obtained at 37°C on the same material as fatigue tested, Pelton et al. convert the strain-life data in Fig. 10 to the stress-based fatigue life plot shown in Fig. 11. In contrast to the anomalous results shown in Fig. 10 as well as the data in Fig. 8 from Harrison and Lin [2], the data in Fig. 11 demonstrate more traditional fatigue behavior with increasing mean tensile stress reducing fatigue life. It would be of interest to replot these data using peak tensile stresses obtained directly from cyclic loading curves.

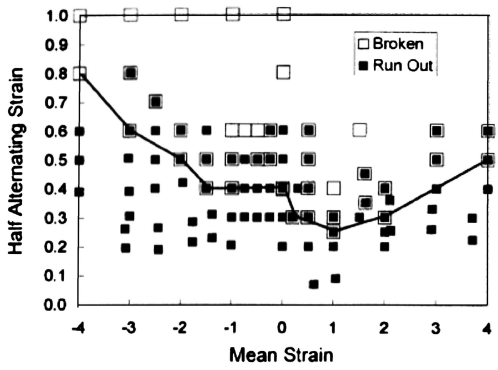

FIG. 10—*Constant life diagram from the data presented in Fig. 9 [3].*

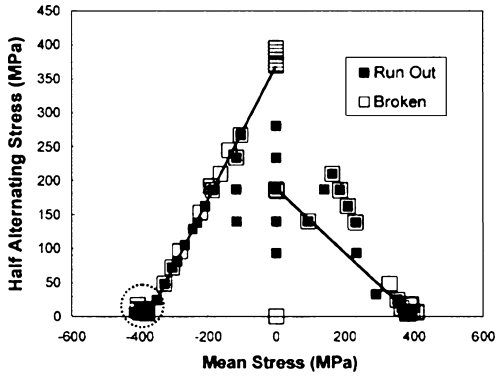

FIG. 11—*Stress-based life diagram converted from strain-based data in Fig. 10 [3].*

Morgan et al. [4] performed strain-controlled fatigue testing on "pickled" pseudoelastic Nitinol wires that had been cold worked and aged at 500°C for 10 min. Specimens were fatigued at 2, 4, and 6 % tensile mean strains at 38°C at a test frequency of 2 Hz. Samples were cycled at alternating strain amplitudes of 0.5, 0.75, 1.0, 1.5, 2.0, 2.5, and 3.0 %. Measured A_f using differential scanning calorimetry (DSC) was 12°C. Additionally, they examined fracture surfaces to investigate fatigue mechanisms and the role of microstructure.

Consistent with previous work, Morgan et al. [4] show decreased fatigue life with increasing alternating strains in the low-cycle region as shown in Fig. 12. As indicated by the near-vertical slope in this region, they found fatigue life to be relatively insensitive to strain amplitude similar to Kim and Miyazaki's [15] data in Fig. 5, but in contrast to Harrison and Lin's [2] and the Pelton et al. [3] data shown in Figs. 6 and 9, respectively. Morgan et al. also show an endurance limit of no more than 0.5 % similar to that found by Pelton et al. and, again, about half that of Harrison and Lin's data. Morgan et al. cite increased volumes of transforming material during cycling at higher alternating strains ($\varepsilon_a > 1.5$ %) result in significant defect generation and shorter fatigue life.

As shown in Fig. 12, and in agreement with the trends seen by Harrison and Lin [2], and Pelton et al. [3], Morgan et al. show increased fatigue life to 4 % mean strain in the high-cycle fatigue region. Furthermore, their data show continued improvement to 6 % mean strain at these low-strain amplitudes. As discussed earlier, Harrison and Lin [2] attribute the unusual observation of increased fatigue life with increasing mean strain to a decrease in corresponding stress amplitude during strain-controlled testing. Based on the schematic monotonic flow curves shown in Fig. 7, this argument accounts for increased fatigue life between zero and nonzero mean strains but does not explain the continued improvement in fatigue life at higher mean strains within the pseudoelastic region, i.e., for $\sim 1\ \% < \varepsilon_m < \sim 6\ \%$.

An example of a fracture surface from a specimen fatigued in the high-cycle region from Morgan et al.

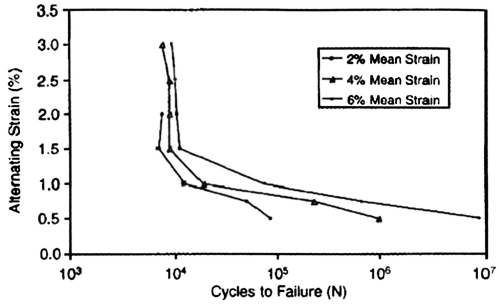

FIG. 12—*Alternating strain versus cycles to failure from Morgan et al..*

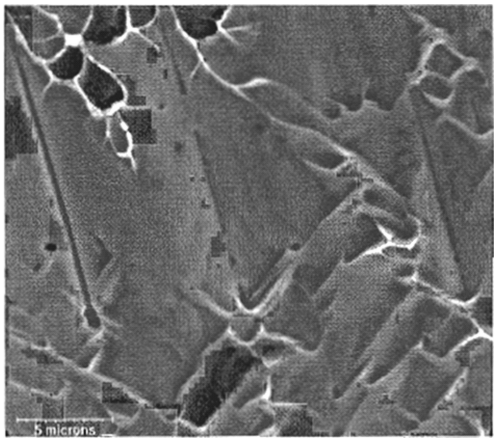

FIG. 13—*Fracture surface of wire tested at low alternating strain [4].*

[4] is shown in Fig. 13. They specifically note microcracking associated with voids resulting in the "comet" type appearance seen in this figure. The surrounding matrix exhibits a "herringbone" pattern typical of four martensite variants. They also observed an increased frequency of microcracking and "herringbone" martensite at higher mean strains. Based on these data, Morgan et al. postulate that despite a higher frequency of microcracking at higher mean strains, the observed increase in fatigue life is the result of more effective blunting of crack tips by the formation of stabilized martensite in the transformation zone at the tip of a propagating crack citing transformation toughening seen in certain materials.

While the specific heat treatments and microstructural details are not provided in their study, it is likely that the fractograph shown in Fig. 13 encompasses a number of austenite grains. If so, that the martensitic variants, as exhibited by the "herringbone" patterns, share common orientations indicative of a common crystallographic orientation of austenite grains within the field of view in Fig. 13, seems unlikely. Another possibility is that the "herringbone" patterns are a manifestation of macroscopic plasticity behavior rather than an indication of transformation behavior.

Crack Propagation Studies

Relatively few studies have addressed the crack propagation aspects of this unusual material. In 2001, McKelvey and Ritchie [16] published their work investigating fatigue crack growth in Nitinol at load ratios R=0.1, 0.5, and 0.7. A rod of Nitinol was annealed at 500°C for 35 min then quenched in ice water. As determined by DSC the resulting transformation temperatures were M_s=−26.9°C, M_f=−54.8°C, A_s =+13.6°C, A_f=+31.3°C, R_s=+23.1°C, and R_f=11.6°C, with R_s and R_f the start and final B2→R transformation temperatures on cooling. Fatigue crack growth behaviors of the stable B2 and metastable B2 structures were studied by cycling disk-shaped compact tension (CT) samples at 120°C ($T>M_d$) and 37°C ($A_f<T<M_s^{\sigma}$), respectively, while that for the stable B19′ martensitic structure was investigated by testing at −65°C and −196°C ($T<M_f$).

In general, McKelvey and Ritchie [16] found fatigue-crack growth resistance increased with decreasing test temperature such that fatigue thresholds were higher and crack growth rates slower in martensite compared to stable austenite or superelastic austenite. Figure 14 shows crack growth rate, da/dN, as a function of stress intensity range, ΔK, for the three microstructural conditions tested at R=0.1 at a frequency of 10 Hz.

As seen in this figure, there is nearly an order-of-magnitude decrease in near-threshold growth rates between 37°C and −65°C and an accompanying 50 % increase in the threshold from superelastic austenite (37°C) ΔK_{th}=2 MPa$\sqrt{\text{m}}$ to ΔK_{th}=3 MPa$\sqrt{\text{m}}$ for the stable martensite tested at −65°C. The fatigue threshold for the stable martensite structure continues to increase with decreasing test temperature. Interestingly, McKelvey and Ritchie [16] point out their current and previous work on fatigue crack growth in

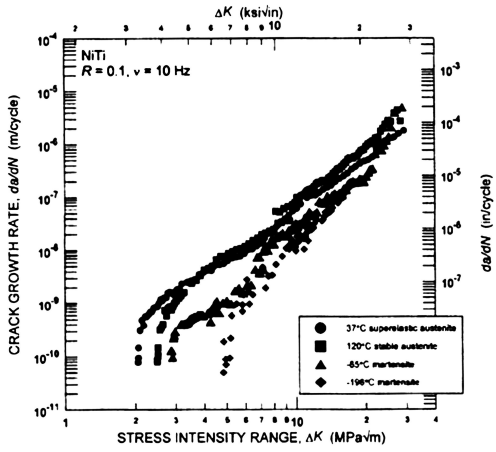

FIG. 14—*Fatigue crack growth curves from McKelvey and Ritchie [16].*

Nitinol demonstrates the superelastic condition and exhibits the worst fatigue-crack growth properties of the three conditions, although it is the most popular microstructure for commercial applications.

McKelvey and Ritchie [16] conclude that despite a marked difference in monotonic flow behavior there is remarkably little difference in the fatigue-crack growth behavior between the stable and metastable (superelastic) microstructures except at near-threshold levels below 10^{-9} m/cycle. Based on their findings McKelvey and Ritchie state that superelasticity does not appear to enhance the fatigue-crack growth resistance of Nitinol.

It is important to note that the heat treatment used by McKelvey and Ritchie [16] for the large diameter rod used for compact tension samples resulted in a fairly well annealed B2 structure as evidenced by the monotonic tensile flow curve presented in their study. In contrast to the cold-worked and relatively short aging times employed in the smooth bar and notched fatigue studies performed on diamond and V-shaped samples discussed above, the lowered B2 strength level resulting from the relatively long time heat treatment at 500°C will likely lead to reduced cyclic stability as previously discussed for Fig. 4.

The reduced strength of the B2 structure will allow more plastic accommodation and likely reduce fatigue life compared with material used in medical devices processed so as to maintain higher B2 strength levels which impart greater resistance to slip deformation and are more representative of actual microstructural conditions of Nitinol in clinical applications.

Discussion and Conclusions

Initial cyclic plasticity studies on Nitinol were performed on wire samples in both fully annealed and pseudoelastic conditions. These efforts outlined some important fundamental aspects of the flow behavior unique to a stress-assisted martensitic phase transformation such as correlating the effect of a positive-temperature dependence of the stress to nucleate martensite with decreased fatigue life at higher test temperatures within the pseudoelastic temperature range, viz., $A_f < T < M_s^{\sigma}$.

The early work by Melton and Mercier [12] revealed the evolutionary flow behavior resulting from cycling fully annealed Nitinol, and the important role of accommodation slip deformation in kinetically stabilizing the resultant martensitic B19′ structure. The subsequent cyclic plasticity study by Zadno et al. [13] showed B2 strength levels necessary for significant strain recovery during isothermal tensile testing of Nitinol could be attained via a number of cold working and aging treatments. Furthermore, their results clearly demonstrate a higher strength B2 structure imparts greater cyclic flow stability with reduced cyclic permanent set, i.e., "ratcheting," as well as a more stable cyclic hysteresis than lower strength austenitic structures. Higher strength parent structures will allow more elastic accommodation of advancing austenite-martensite interfacial stress fields and reduced concomitant slip deformation which should improve fatigue life.

Since the introduction and development of this alloy for medical implants a number of empirical studies have attempted to quantify fatigue life using single-diamond cell samples designed to simulate the in-vivo operating conditions of the repetitive stent unit. Resulting displacement-controlled fatigue data are then presented on constant-life diagrams in terms of alternating strain amplitude, ε_a, and imposed mean strains, ε_m, and compared with modified Goodman, Soderberg, or Gerber life-prediction formulas [17]. While studies generally agree that increasing mean strain within the pseudoelastic strain region either has no effect or actually improves the fatigue life of Nitinol; for a variety of reasons there is disagreement in interpretation of reported results as presented in terms of these infinite-life paradigms. This is not unexpected as traditional stress-based, constant-life models assume a power-law hardening material undergoing homogeneous deformation. Given the heterogeneous nature of a mechanically-induced martensitic phase transformation acting as a deformation mechanism along with the extreme effects that a large crystallographic shape change has on the macroscopic flow behavior, it is not unreasonable to anticipate that a novel approach to interpretation of strain-controlled fatigue data and resulting mapping of the infinite life realms might be required for Nitinol.

Consistent with most engineering materials, the results of smooth bar and notched fatigue studies performed on diamond and V-shaped samples that were cold-worked with relatively short aging treatments show the fatigue life of Nitinol decreases with increasing strain amplitude in the low-cycle fatigue region. In contrast, these same studies show increasing mean strain improves high-cycle fatigue life in strain-controlled testing, although there is a two-fold difference in the reported fatigue endurance limits between the various studies. The source of the discrepancy is not clear, although by either measure, Nitinol is exhibiting relatively good fatigue endurance limits compared to other metallic alloys when expressed in terms of strain amplitude. The work by Pelton et al. [3] show that when analyzed in terms of stress amplitude Nitinol may obey more traditional Goodman-type behavior with increasing tensile mean stress decreasing fatigue life. When expressed as a stress-amplitude, the fatigue limit for Nitinol is not very high with the Pelton et al. data showing a stress-endurance limit of about 200 MPa at zero mean stress.

Various hypotheses have been proffered to explain the anomalous high-cycle fatigue behavior observed in strain-controlled testing of Nitinol. Based on the "herringbone" structure seen on the surfaces of fractured specimens in the high-cycle region, Morgan et al. [4] suggest that the continued increase in high-cycle fatigue life with increasing mean strain is the result of more effective blunting of crack tips by the formation of stabilized martensite in the transformation zone at the tip of a propagating crack citing transformation toughening seen in certain materials. As discussed, however, it is not clear that the "herringbone" structure shown in Fig. 13 is indicative of transformation behavior or a manifestation of the macroscopic plasticity character of this material. Nonetheless, higher mean strains inherently involve a greater volume fraction of martensite at the start of testing. Morgan's et al. argument is thus plausible based on McKelvey and Ritchie's [16] work demonstrating a higher fatigue threshold and reduced crack propagation rate in stabilized martensite than in either a stable or metastable B2 structure, although the longer aging treatment used by McKelvey and Ritchie resulted in reduced B2 strength and is thus not necessarily reflective of material behavior as used in medical devices with higher austenitic strength. That the metastable austenitic structure exhibits the lowest threshold and highest crack propagation rate of the three structures remains unclear.

There is merit to Harrison and Lin's [2] suggestion that reduced stress amplitude results in improved fatigue life comparing zero to nonzero mean strains in strain-controlled testing, but remains insufficient in rationalizing the observed continued improvement in high-cycle fatigue life with increasing mean strain. Of course, their argument is based on the initial hysteresis loop rather than the cyclically-stabilized condition. Indeed, the results of cyclic plasticity studies outlined herein clearly show three primary effects of cycling on the flow behavior of Nitinol: continued accumulation of permanent set, i.e., ratcheting, especially during initial cycling, an increasing "monotonic" work hardening rate, and a reduced hysteretic area. These effects may result in either cyclic work hardening or softening of the material depending on specific test conditions.

Given the evolving nature of the hysteresis during cycling in Nitinol, it is not difficult to envision a number of means by which high-cycle fatigue life might increase with increasing mean strain in strain-controlled testing. For example, in addition to an overall reduction in area and the increased "monotonic" hardening rate, inspection of the cyclically-stable hysteresis shows "tapering" at the extreme of strain amplitude. The "tapering" is an indication of reduced interfacial friction as described by Salzbrenner and

Cohen [10] who cite decreased thermal hysteresis with increasing volume fraction of martensite in thermoelastic alloys. As the average martensite plate volume decreases with increasing transformed volume fraction, the average plate undergoing cyclic interfacial motion is smaller at higher mean strains than at lower mean strains. With a reduction in average plate volume interfacial stresses are reduced which, together with increased strength of the B2 structure resulting from cyclically-induced work hardening, result in reduced plastic accommodation and improved fatigue life.

Further understanding of the fatigue behavior of Nitinol will require well designed testing to explore the more subtle aspects of this material in relation to the B2 → B19′ martensitic transformation as was done by Berg [18] in formulating a "mechanistic" phase diagram incorporating test paradigms designed to explore properties of the stable and metastable structures. In addition to relative test temperature, i.e., $T_{\text{test}} - M_s$ (or A_f) to attain a constant thermodynamic driving force such testing should consider the inherent resistance to slip of the austenite (austenite yield strength), as reduced concurrent slip should improve cyclic stability and fatigue life. As well, the evolutionary nature of the flow curve during fatigue cycling in Nitinol is pronounced, especially at larger strain amplitudes. This aspect of fatigue has received little attention both in terms of understanding the fatigue behavior of Nitinol as well as in constitutive relations used in finite element (FEA) codes for device design and fatigue analysis. In this regard, transformation kinetics should be considered to discern interface-slip interactions, stress-assisted and strain-induced nucleation, as well as the effects of average martensite plate volume, both near M_s^{σ}, and at body temperature, on fatigue life. Explicit micromechanical modeling of concurrent slip would provide insights in this area. Stress-based analysis of strain-controlled fatigue testing of Nitinol will also allow interpretation from a more traditional fatigue perspective.

References

[1] Duerig, T. W. and Tolomeo, D. E., "An Overview of Superelastic Stent Design," *Proceedings of the International Conference on Shape Memory and Superelastic Technologies*, Asilomar, CA, SMST, 30 April–4 May 2000, pp. 585–604.

[2] Harrison, W. J and Lin, Z. C., "The Study of Nitinol Bending Fatigue," *Proceedings of the International Conference on Shape Memory and Superelastic Technologies*, Asilomar, CA, SMST, 30 April–4 May 2000, pp. 391–396.

[3] Pelton, A. R., Gong, X. Y., and Duerig, T., "Fatigue Testing of Diamond-Shaped Specimens," *Proceedings of the Materials and Processes for Medical Devices Conference*, Anaheim, CA, ASM International, 8–10 Sept. 2003, pp. 199–204.

[4] Morgan, N. B., Painter, J., and Moffat, A., "Mean Strain Effects and Microstructural Observations During in-vitro Fatigue Testing of NiTi," *Proceedings of the International Conference on Shape Memory and Superelastic Technologies*, Asilomar, CA, SMST, 5–8 May 2003, pp. 303–310.

[5] Wayman, C. M. and Duerig, T. W., "An Introduction to Martensite and Shape Memory," *Engineering Aspects of Shape Memory Alloys*, Butterworth-Heinemann Ltd., London, 1990, pp. 3–20.

[6] Melton, K. N., "Ni-Ti Based Shape Memory Alloys," *Engineering Aspects of Shape Memory Alloys*, Butterworth-Heinemann Ltd., London, 1990, pp. 21–35.

[7] Cohen, M. and Wayman, C. M., "Fundamentals of Martensitic Reactions," *Metallurgical Treatises*, TMS-AIME, 1983, pp. 445–468.

[8] Takimoto, A., "Relationship Between Volume Fraction of Strain-Induced Martensite Under Tension and Electrical Resistivity in a Ti-Ni SMA Wire," *J. de Physique*, Vol. 5, 1995, pp. 599–604.

[9] Karaman, I., Kulkarni, A. V., and Luo, Z. P., "Transformation Behavior and Unusual Twinning in a NiTi Shape Memory Alloy Ausformed Using Equal Channel Angular Extrusion," *Philos. Mag.*, Vol. 85, 2005, pp. 1729–1745.

[10] Salzbrenner, R. J. and Cohen, M., "On the Thermodynamics of Thermoelastic Martensitic Transformations," *Acta Metall.*, Vol. 27, 1979, pp. 739–748.

[11] Olson, G. B., "Transformation Plasticity and the Stability of Plastic Flow," *Deformation, Processing, and Structure*, ASM International, Materials Park, OH, 1984, pp. 391–424.

[12] Melton, K. N. and Mercier, O., "Fatigue of NiTi Thermoelastic Martensites," *Acta Metall.*, Vol. 27, 1979, pp. 137–144.

[13] Zadno, G. R., Yu, W., and Duerig, T. W., "Fatigue Properties of Superelastic Ni-Ti," Raychem

Corporation, internal publication, 1989.
[14] Nishida, M., Wayman, C. M., and Honma T., "Precipitation Processes in Near-Equiatomic TiNi Shape Memory Alloys," *Metall. Trans. A*, Vol. 17A, 1986, pp. 1505–1515.
[15] Kim, Y. S. and Miyazaki, S., "Fatigue Properties of Ti-50.9a/oNi Shape Memory Wires," *Proceedings of the International Conference on Shape Memory and Superelastic Technologies*, Asilomar, CA, SMST, 2–6 March 1997, pp. 473–478.
[16] McKelvey, A. L. and Ritchie, R. O., "Fatigue-Crack Growth Behavior in the Superelastic and Shape-Memory Alloy Nitinol," *Metall. Mater. Trans. B*, Vol. 32A, 2001, pp. 731–743.
[17] Mitchell, M. R., "Fundamentals of Modern Fatigue Analysis for Design," *ASM Handbook*, ASM International, Materials Park, OH, Vol. 19, 1996, pp. 227–249.
[18] Berg, B. T., private communication, 2006.

Journal of ASTM International, Vol. 4, No. 3
Paper ID JAI100657
Available online at www.astm.org

Ming H. Wu[1]

Effects of Phase Transformations on Fatigue Endurance of a Superelastic NiTi Alloy

ABSTRACT: It is well known that NiTi shape memory alloys exhibit superelasticity where a large elastic deformation proceeds under a constant stress due to the formation of stress-induced martensite. However, for most commercial NiTi alloys used in medical devices, the materials are processed in such a way that the R-phase transformation is apparently separated from the martensitic transformation. The B2 to R-phase change exhibits a much smaller shape change and a narrower hysteresis than does the B2 to B19′ martensite transformation. Hence, the transformation temperatures as well as the thermomechanical properties associated with the R-phase are much more stable during cyclic deformation when compared to those associated with the B19′martensite. The crystallographic features for both martensitic and R-phase transformations are reviewed, and their effects on the tensile properties and rotating-beam fatigue endurance are studied in the present paper.

KEYWORDS: NiTi, B19′, martensite, R-phase, superelasticity, rotating-beam fatigue

Introduction

Because of their unique superelasticity and excellent biocompatibility, NiTi shape memory alloys have rapidly become a material of choice for many revolutionary medical devices in recent years. The enormous flexibility resulting from stress-induced martensitic transformation allows medical devices and implants of NiTi alloys to be squeezed through small incisions and through a combination of elastic and thermal effects to regain their designed shapes. Because of the extremely dynamic nature of the living anatomy, these devices and implants are subjected to high cycles of complex loading in-vivo. Fatigue endurance is therefore an important consideration for these applications.

The most commonly used NiTi alloy for medical devices and implants has a composition of Ti-55.8 wt.%Ni (Ti-50.8 at.%Ni). When fully recrystallized, such as after annealing at temperatures greater than 600°C for a proper duration of time, this material exhibits a single stage martensitic transformation from the parent B2 to B19′ monoclinic martensite. However, when optimized for superelastic mechanical properties, as in most medical devices and implants, the alloy has generally been cold worked and subsequently heat treated at lower temperatures such that remaining dislocations and fine Ni-rich precipitates are present in the material. Transformation in this type of microstructure proceeds in two stages of B2→R-phase→B19′ martensite [1].

B2→R-Phase *Transformation*

The B2→R-phase transformation has long been a controversial subject. Often thought of as a precursor to the martensitic transformation in the early days, the B2→R-phase transformation had been clearly demonstrated to be a first-order displacive transformation in a transmission electron microscopy (TEM) study by Hwang et al. [2] as the R-phase possesses a well-defined crystal structure and a plate-shaped domain. Khachin et al. [3] supported this argument demonstrating that both R-phase and B19′ martensitic transformations exhibit distinctive shape memory effects, superelasticity, and high damping capacity. However, the presence of diffuse scattering at incommensurate positions in the electron diffraction patterns prior to the R-phase transformation, as reported in Hwang's work, continued as a subject of debate. A detailed

Manuscript received May 23, 2006; accepted for publication January 18, 2007; published online April 2007. Presented at ASTM Symposium on Fatigue and Fracture of Medical Metallic Materials and Devices on 7–11 November 2005 in Dallas, TX; M. R. Mitchell and K. L. Jerina, Guest Editors.
[1] Memry Corporation, 3 Berkshire Boulevard, Bethel, CT 06801.

diffraction and resistivity investigation by Salamon et al. [4] showed that the incommensurate diffuse reflections gradually moved toward the commensurate positions during cooling prior to the R-phase transformation. These diffuse reflections suggest the presence of lattice distortion and the authors interpreted the phenomenon as a charge density wave that gradually condensed to form the R-phase with decreasing temperature. Using an energy-filtered TEM technique and X-ray diffraction, Shindo et al. [5] was able to clarify that the incommensurate diffuse scattering prior to the R-phase transformation is in fact caused by the transverse atomic distortion of soft $\{110\}\langle 1\bar{1}0\rangle$ phonon.

The crystal structure of the R-phase was interpreted to be rhombohedral, and hence the designation of "R-phase." Lately, the R-phase crystal structure has been better elucidated using a refined X-ray diffraction technique [6] to have a trigonal symmetry of the P3 space group. Although the crystalline phase change is abruptly evident at the time of transformation, the lattice deformation of the R-phase with respect to that of the parent continues to increase, as indicated by the continuously changing α-angle with decreasing temperature [4], a characteristic clearly of a second-order phase transformation.

Because R-phase lacks lattice-invariant shear, the phenomenological theory for martensitic transformation has its limitation for calculating the crystallographic parameters. Instead it is more straight forward to calculate the lattice deformation of the transformation along the parent $\langle 111\rangle$ direction. Using the lattice constants measured by Ling and Kaplow [7], Otsuka and Ren calculated the strain to be about 0.5 % at 20°C below the R_s temperature and 0.9 % at 60°C below the R_s temperature [8]. These results are in good agreement with the tensile stress-strain data associated with the deformation of R-phase measured by Miyazaki et al. [9] using a single crystal of Ti-50.5 at.%Ni in composition.

B2→B19′ *Transformation*

While it is far more difficult to treat the crystallography associated with the R-phase→B19′ transformation, the crystallographic analysis for the B2→B19′ martensitic transformation is well within the scope of the phenomenological theory for martensitic transformation. For simplicity, only the B2→B19′ transformation is reviewed here.

The B19′ martensite is monoclinic and has the symmetry of $P2_1/m$ space group [10]. The lattice-invariant shear consists of $\langle 011\rangle$ Type II twining and possibly also $\{111\}$ and $\{011\}$ Type I twining [8]. The theoretical shape change direction has been calculated to be [0.43448, 0.75743, 0.48737] with a magnitude of 0.13078, in good agreement with the experimental measurements on a single martensite plate by the scratch displacement technique [11]. The calculated orientation dependence of shape memory strain also agrees well with the tensile stress-strain data measured from single crystal specimens with the maximum strain recovery occurring along the parent $\langle 111\rangle$ direction [12]. The recoverable strain observed in commercial polycrystalline NiTi alloys is generally about 0.06 (6 %) which is much smaller compared to the calculated shape change magnitude for the single martensite plate or that for the single crystal specimen.

Effects of R-Phase and Martensite on NiTi *Fatigue*

Superelastic NiTi alloys exhibit an unconventional fatigue behavior and the influence from the martensitic transformation was often noted. For example, fatigue-crack propagation rates have been reported to be higher at superelastic temperatures than in the fully martensitic state [13]. In contrast to the behavior of conventional materials, increasing mean strain prolongs the fatigue life of superelastic NiTi when more stress-induced-martensite is present in the alloy [14].

The influence of R-phase on the fatigue property of superelastic NiTi is less clear. This may in part be due to the fact that the stress plateau associated with R-phase transformation occurs only in a narrow temperature range around the vicinity of the R-phase transformation temperature because the temperature dependence of the critical stress to mechanically induce R-phase is quite steep when compared to that for the stress-induced martensitic transformation [15]. Due to the small lattice deformation associated with the R-phase transformation both the transformation strain and the transformation temperature are much more stable than those for the martensite during thermomechanical cycling of NiTi actuators [15–17]. Hence one would anticipate that the NiTi fatigue endurance would benefit by involving R-phase transformation during the cyclic deformation at least in a deformation mode where the alternating strain is comparable to the R-phase lattice deformation. Lopes et al. [18] carried out a fatigue study on Ti-50.8 at.%Ni tubing after aging at various temperatures between 350 and 500°C. The test was conducted at 1.5 % mean strain

TABLE 1—*Transformation temperatures*[a] *determined by a DSC method.*

Specimen	Heat Treat Temperature (°C)	R_s(°C)	R_f(°C)	A_s(°C)	A_f(°C)	M_s(°C)
A	480	27	7	8	29	<−70
B	525	7	−9	−6	10	<−70

[a]Per ASTM F 2005-00 Standard Terminology for Nickel-Titanium Shape Memory Alloys.

and 0.2–0.4 % alternating strain in tension. Specimens aged at 450°C and lower exhibited evident R-phase plateau in the stress-strain tensile curves. However, the results were inconclusive about the effect of various aging treatments on fatigue life; thus the influence of R-phase plateau on NiTi fatigue behavior remains unclear.

To further understand the influence of R-phase transformation on NiTi fatigue, wires of Ti-55.9 wt. %Ni (Ti-55.9 at. %Ni) in composition were processed in two different ways such that in one condition the wire exhibits only martensite plateau while in the other condition, both R-phase and martensite plateau are present in the tensile stress-strain curve.

Experiment Procedures

Wires of Ti-55.9 wt. %Ni having a nominal ingot A_s temperature of −15°C were cold drawn to 0.53 mm in diameter with a retained cold work of about 45 % reduction in the cross-sectional area. The test specimens were subsequently heat treated at 450–550°C. Two sets of heat treat where the resulting specimens exhibit similar plateaus stresses but different R-phase transformation temperatures were selected for further study. After heat treating the surface oxide was removed by chemical etching. The transformation temperatures were measured by differential scanning calorimetry (DSC) and the tensile properties were measured by using an Instron Model 5565 Tensile Tester equipped with a temperature control chamber. The strain was monitored using an Epsilon extensometer. The fatigue lives were characterized by rotating-beam fatigue tests at 1000 r/min in a 37°C water bath. Three specimens of each heat treat were fatigued at each strain level from 0.5 to 2.4 % to a maximum of 20,000,000 cycles.

Experimental Results

Transformation Temperatures

Transformation temperatures measured by DSC scan from 50°C to −70°C are listed in Table 1. Note that only the R-phase transformation peaks were detected as the martensite transformation temperatures are below the scan limit of −70°C.

Tensile Properties

The tensile stress-strain curves of specimens A and B tested at 37°C and pulled to 6 % are plotted in Figs. 1 and 2, respectively. Both specimens exhibit very similar upper plateau strengths of about 80 Ksi and lower plateau strengths around 45 Ksi. In spite of the similar plateau stresses, the linearly elastic portions between the two tensile curves exhibit a noticeable difference when examined in detail. The tensile curve of the 525°C heat treated specimen (Fig. 2) shows the segment before the plateau is relatively linear with a yield drop at 0.9 % tensile strain. The Young's modulus calculated from the slope is 10.6 Msi. In contrast, the tensile curve of the 480°C heat treated specimen (Fig. 1) prior to the plateau exhibits curvature starting at about 40 Ksi and the on-set of pseudoelastic plateau is delayed to about 1.2 % strain. The apparent modulus calculated based on the stress at 1 % tensile strain is also reduced to 7.2 Msi.

The difference between the two heat treats is more revealing when comparing the stress-strain curves tested to 1 % tensile strain shown in Figs. 3 and 4. The deflecting feature in the elastic curve of the 480°C heat treated specimen is evident as seen in Fig. 3 and the loading and unloading segments of the curve perfectly overlap with nil hysteresis, while in Fig. 4, the curve of 525°C heat treated specimen exhibits a well defined hysteresis typical of the martensitic transformation. Noting the much higher R-phase trans-

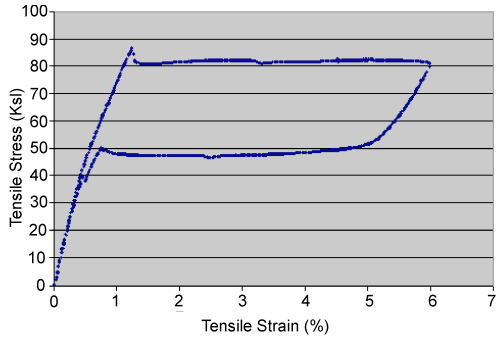

FIG. 1—*Tensile stress-strain curve of 480°C heat treated specimen A tested to 6 % strain at 37°C.*

formation temperatures (R_s, R_f, A_s and A_f) for specimen A than for specimen B, it is obvious that during testing to 1 % strain transformation to the R-phase occurs, while specimen B exhibits a primary transformation to martensite.

Rotating-Beam Fatigue Endurance

The fatigue endurances of both groups of specimens A and B were evaluated using a rotating-beam fatigue test method and the resulting S-N curves are plotted in Fig. 5. There is no obvious difference in fatigue life

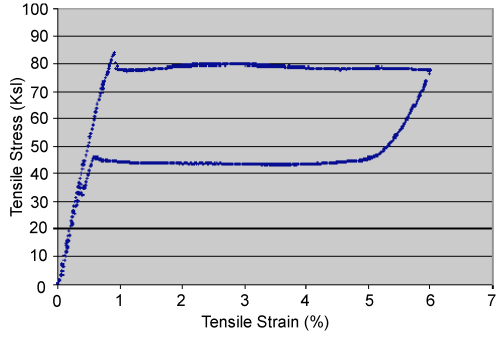

FIG. 2—*Tensile stress-strain curve of 525°C heat treated specimen B tested to 6 % strain at 37°C.*

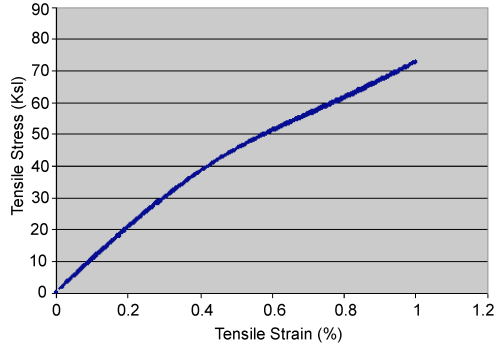

FIG. 3—*Tensile stress-strain curve of 480°C heat treated specimen A tested to 1 % strain at 37°C.*

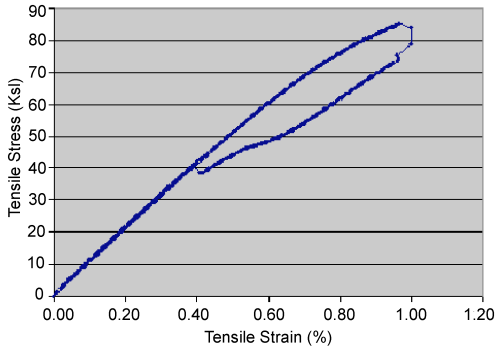

FIG. 4—*Tensile stress-strain curve of 525°C heat treated specimen B tested to 1 % strain at 37°C.*

between the two groups of specimens when tested at alternating strain levels greater than 1 %. At alternating strains equal to or less than 1 %, group A specimens consistently exhibited higher fatigue endurance than those in group B. There is also an obvious difference in the run-out strain between the two groups of specimens. While two out of three specimens in group A survived the run-out cycles, all three specimens of group B failed before 20 million run-out cycles at 0.65 % strain. The fatigue limit for group B appears to be 0.5 % strain while that for group A is slightly higher.

According to the present finding, the presence of R-phase at small tensile strains is beneficial to the rotating beam fatigue endurance because the stress-induced R-phase transformation lowers the operating stress level of the NiTi wire at the 0.4–1.0 % strain levels. In addition, the B2 to R-phase transformation allows the cyclic deformation to be accommodated by the B2 to R-phase lattice distortion during the transformation which substantially reduces defect generation.

Conclusions

1. By varying the heat-treat parameters, NiTi materials of similar martensitic plateau stresses but having quite different R-phase transformation characteristics can be obtained. In the present case, heat treating at 480°C yielded much higher R-phase transformation temperatures than at 525°C.
2. When the R-phase transformation temperatures are close to the tensile test temperature, an additional plateau associated with stress-induced R-phase transformation is present at strain levels between 0.4 and 1.0 %. The presence of R-phase plateau delays the on-set of pseudoelastic plateau associated with the martensitic transformation from 0.9 to 1.2 % tensile strain and reduces the apparent modulus from 10.6 Msi to 7.2 Msi.

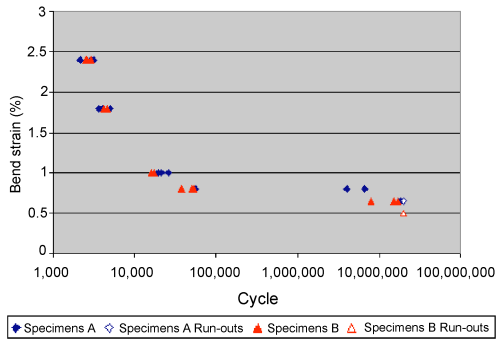

FIG. 5—*Rotating beam fatigue SN curves of specimens heat treated at 480°C (A) and 525°C (B).*

3. Specimens heat treated to exhibit higher R-phase transformation temperatures, and hence R-phase plateau in tensile test, perform better in rotating beam fatigue tests at strain up to 1.0 %. In these specimens, the R-phase, instead of martensite, is apparently induced during the cyclic fatigue deformation at these low strain levels. Stress-induced R-phase transformation results in lower operating stress and allows the cyclic strain to be accommodated by the lattice distortion associated with the B2 to R-phase transformation, which substantially reduces the risk of defect generation.

References

[1] Treppmann, D., Hornbogen, E., and Wurzel, D., "The Effect of Combined Recrystallization and Precipitation Processes on the Functional and Structural Properties in NiTi Alloys," *J. Phys. IV, Colloque C8*, August 1995, pp. 569–574.

[2] Hwang, C. M., Meichle, M., Salamon, M. B., and Wayman, C. M., *Philos. Mag. A*, Vol. 47, 1983, p. 31.

[3] Khachin, V. N., Gjunter, V. E., Sivokha, V. P., and Savvinov, A. S., "Lattice Instability, Martensitic Transformations, Plasticity and Anelasticity of NiTi," *Proceedings of the International Conference on Martensitic Transformations*, 24–29 June 1979, Cambridge, MA, pp. 474–479.

[4] Salamon, M. B., Meichle, M. E., and Wayman, C. M., *Physics Reviews B*, Vol. 31, 1985, p. 7306.

[5] Shindo, D., Murakami, Y., and Ohba, T., "Understanding Precursor Phenomena for the R-Phase Transformation in Ti-Ni-Based Alloys," *MRS Bull.*, Vol. 27, 2002, pp. 121–127.

[6] Hara, T., Ohba, T., and Otsuka, K., "Structural Study of the R-Phase in Ti-Ni Alloy by the Rietveld Method," *J. Phys. IV, Colloque C8*, August 1995, pp. 641–645.

[7] Ling, H. C. and Kaplow, R., *Metall. Trans. A*, Vol. 11, 1980, p. 77.

[8] Otsuka, K. and Ren, X., *Prog. Mater. Sci.*, Vol. 50, 2005, p. 511.

[9] Miyazaki, S., Kimura, S., and Otsuka, K., *Philos. Mag. A*, Vol. 57, 1988, p. 467.

[10] Kudoh, Y., Tokonami, M., Miyazaki, S., and Otsuka, S., *Acta Metall.*, Vol. 33, 1985, p. 2049.

[11] Matsumoto, O., Miyazaki, S., Otsuka, K., and Tamura, H., *Acta Metall.*, Vol. 35, 1987, p. 2137.

[12] Miyazaki, S., Kimura, S., Otsuka, K., and Suzuki, Y., *Scr. Mater.*, Vol. 18, 1984, p. 883.

[13] McKelvey, A. L. and Ritchie, R. O., *Metall. Mater. Trans. A*, Vol. 32A, 2001, p. 731.

[14] Morgan, N. B., Painter, J., and Moffat, A., *Proceedings, International Conference on Shape Memory and Superelastic Technologies*, 5–8 May 2003, Pacific Grove, CA, p. 303.

[15] Stachowiak, G. B. and McCormick, P. G., *Acta Metall.*, Vol. 36, 1988, p. 291.

[16] Miyazaki, S., Igo, Y., and Otsuka, K., *Acta Metall.*, Vol. 34, 1986, p. 2045.

[17] Todoroki, T. and Tamura, J., *J. Jpn. Inst. Met.*, Vol. 50, 1986, p. 546.

[18] Lopes, T. L., Gong, X-Y., and Trépanier, C., *Proceedings, International Conference on Shape Memory and Superelastic Technologies*, 5–8 May 2003, Pacific Grove, CA, p. 311.

Journal of ASTM International, Vol. 3, No. 9
Paper ID JAI100374
Available online at www.astm.org

K. E. Perry,[1] *P. E. Labossiere,*[1] *and E. Steffler*[2]

Thermoelastic Transformation Behavior of Nitinol

ABSTRACT: The transformation behavior of Nitinol under uniaxial tension and four-point bending was investigated. A novel sample geometry produced from drawn tubing was used to observe the differences caused by localized phase transformation effects between the two types of loading and between samples with different process and load histories. Phase shifted moiré interferometry was used to provide full-field measurement of strain during the experiments. Optical resolution and grating coherence were sufficient to simultaneously resolve the strain fields within both the parent and transformed phases of the material. Evidence of both localized and uniformly distributed phase transformation is observed for the samples tested in tension while the bending results clearly indicate an asymmetric neutral axis and a complex reverse bending response for samples containing a strong R-phase component and tested at temperatures below critical transformation temperatures.

KEYWORDS: Nitinol, thermoelasticity, phase transformations, photomechanics, moiré interferometry, full-field measurements, modeling, carrier fringes

Introduction

Nitinol has seen increased use in medical applications where devices are compressed to catheter dimensions, delivered through tortuous anatomy, and deployed in various diseased locations within the human body. The material is well suited to the design constraints imposed by such conditions and often provides incomparable advantages over other engineering materials. Alloy composition and processing history can [1–3] be used to achieve a broad range of material response that can be tailed to intended applications.

The stress-induced phase transformation and mechanical behavior of Nitinol have been generally described [4] and progress has been made on many fronts to further understanding of shape memory and superelastic material behavior [5–7]. Accurate and reliable measurements of material properties in Nitinol are difficult due to the material's strong dependence on temperature, processing, and load history as well as the phase transformation behavior that may exhibit localization. Global measurements, such as strain obtained using an extensometer during uniaxial tensile testing, can obscure the effect of localized transformation bands and potentially mislead interpretations of material behavior.

The interferometric measurement technique of moiré interferometry [8] is an excellent candidate for providing accurate material property information in Nitinol. The technique is well established and is routinely used to characterize complex material behavior playing a pivotal role in the development and validation of constitutive models for advanced engineering materials [9].

Recent studies by the authors have demonstrated the applicability of phase shifted moiré interferometry to strain measurements in Nitinol [10] with special attention to experimental details such as the effect of specimen grating thickness and density, fringe analysis, and the quantification of full-field strains [11].

Presently we utilize a novel sample design to measure full-field strain during uniaxial tension and four-point bending of Nitinol. Differences caused by localized phase transformation effects were studied in detail through the use of carrier fringes with samples having different process and load histories. Here we present only key results showing the capabilities of phase shifted moiré interferometry, the difficulties associated with Nitinol calibration due to the complex transformation behavior, and the sensitivity of the material to temperature. The results presented herein are not complete and are merely representative results of numerous experiments still underway in our laboratory.

Manuscript received December 5, 2005; accepted for publication April 14, 2006; published online October 2006. Presented at ASTM Symposium on Fatigue and Fracture of Medical Metallic Materials and Devices on 7–11 November 2005 in Dallas, TX; M. R. Mitchell and K. L. Jerina, Guest Editors.
[1] ECHOBIO LLC, 579 Azalea Avenue, Bainbridge Island, WA98110.
[2] Idaho National Engineering Laboratory, Idaho Falls, ID83415.

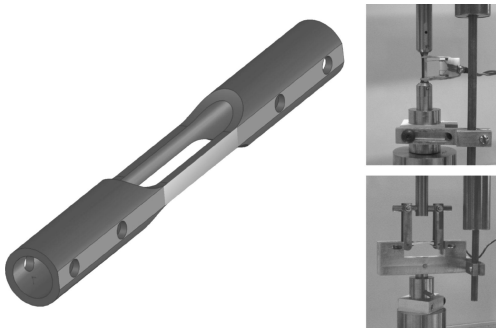

FIG. 1—*Schematic of the test sample and photographs of the tensile and four-point bend configurations.*

Test Samples

Material and Processing History

The material used in this study was SE-508, seamless drawn tubing from Nitinol Devices and Components, Inc., with an as-received A_f of −9°C. Two distinct heat treatments were chosen, denoted by A and B. Treatment A was performed at 325°C for 60 min and Treatment B was performed at 500°C for 30 min. All samples were water quenched subsequent to heat treating.

The active A_f temperatures were measured for all test samples following ASTM standard F 2082 for free bend and recovery over the temperature range from −30 to 30°C. Very consistent results were obtained and representative curves of deflection versus temperature are shown in Figs. 3 and 4 for the two heat treatments. Treatment A resulted in test samples with an active A_f of 25.4°C and exhibited a strong R-phase component with an R'_f of −3.5°C. Treatment B did not exhibit a noticeable R-phase component and had an active A_f of 22°C.

Geometry and Loading

A single sample geometry was chosen for both uniaxial tension and four-point bending tests. Figure 1 is a schematic of the sample geometry and photographs of the two loading scenarios.

Two pairs of holes were laser cut in the ends of the samples and then carefully honed to ensure precision pin loading of the test samples. The gage section of the samples were EDM'ed to produce perpendicular edges, maximizing the amount of material in the gage section and ensuring uniform behavior in bending. Slow feed, low power, and multiple passes were used to minimize adverse effects on the

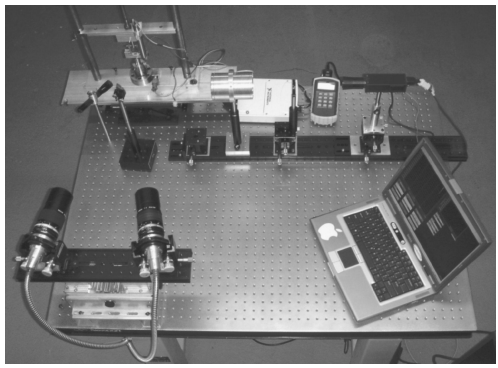

FIG. 2—*Photograph of the custom load frame in the moiré interferometer.*

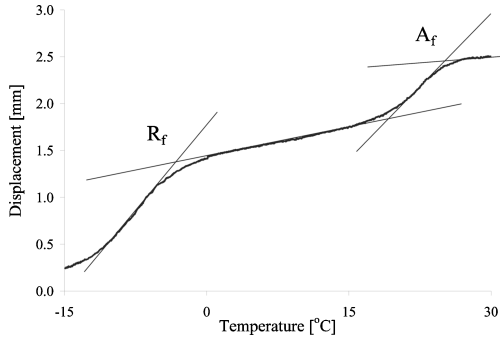

FIG. 3—*Displacement versus temperature from the free bend recovery test for material A showing location of A_f and R_f.*

bulk material properties. A flat surface was carefully ground on one face of the test samples to provide an optically flat surface for the grating replication process. Prior to production of the samples, FEA was used to optimize the design of the sample geometry and the corresponding fixtures to achieve uniform tension and pure bending over a large range of deformations. A slow loading rate (<1 mm/min) was used for all of the tests.

Testing

Global Measurements

Global (far-field) measurements of the sample load, extension, and displacement were made using a load cell, extensometer with a gage length of 10 mm and LVDT, respectively. Additionally, thermocouples were used to monitor the ambient temperature and the sample temperature throughout the experiments. Prior to beginning an experiment, the temperature was raised well above A_f and then slowly lowered to the desired test temperature to ensure an initial fully austenitic state. Ambient test temperatures were held constant within 1 °C throughout all of the experiments.

The samples were loaded in either tension or bending using a custom-built load frame and fixtures. Figure 2 shows a photograph of the load frame with a sample mounted in the moiré interferometer and imaging system. The experiments employed two personal computers, one each for the data acquisition and

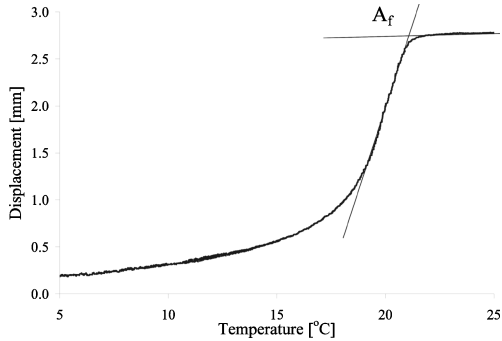

FIG. 4—*Displacement versus temperature from the free bend recovery test for material B showing location at A_f.*

imaging systems. Load, deflection, and extension measurements were digitized to 16 bits and recorded using a conventional data acquisition system at 50 Hz. Calibration for all sensors was performed to ensure accurate measurements.

Full-field Measurements

Moiré interferometry is a well established method in experimental mechanics and has been applied to single crystal shape memory materials [12]. The general technique is described in detail in [8]. For our work, we exploit phase shifting [13] that provides exceptional noise reduction while enhancing spatial resolution. Five phase shifted images were recorded for each full-field measurement at a resolution of 1280 by 960 pixels with 10 bit grayscale resolution. The typical field of view was on the order of 1–2 mm.

The interferometer used for these experiments was custom built with an integrated fiber optic splitter and phase shifter to provide exceptional stability and configurability [14]. Diffraction gratings were produced from holographic exposures of photographic plates. They were epoxy replicated using a method capable of producing a final grating thickness of 5–20 μm. A grating density of 300 L/mm was chosen to maximize measurement sensitivity for the anticipated range of deformations. This resulted in a fringe order sensitivity of 1.67 μm/fringe.

Carrier fringes [8] were used to extend the range over which displacement measurements could be made. Carrier fringes are produced by changing the angles of the incident beams and provide an offset to the effective diffraction grating density. They do not increase or decrease the inherent sensitivity of moiré interferometry data, but rather change the number of fringes produced for a given deformation. By dialing in or out carrier fringes, an extended measurement range was achieved so that strain measurements could be made in both the austenite and martensite phases.

Fringe analysis was performed manually by plotting the wrapped fringe contours and counting them edge to edge. The phase shifted data provided excellent contrast for identifying fringe centers as well as resolving the slope of the wave front. The gage length used for strain calculations was kept consistent for any given series of measurements, and was usually on the order of 0.5–0.8 mm (toward the higher end of the range for the tensile measurements and the lower end of this range for the bend measurements). The choice of gage length for the full-field measurements had little significance in the strain measurements over this range for both the tensile and bend tests. The estimated precision of the strain measurements was determined to be ±0.02 %.

Tension Test Results

Figure 5 shows a sequence of images of wrapped fringes of the tensile loading for a representative sample processed according to Treatment B. The sample was tested at a temperature of 19°C which is below the active A_f temperature of the material. Figures 5(*a*)–5(*h*) show a sequence of images during the tensile loading portion. Transformation occurs at both the top and bottom of the gage section as the loading increases and propagates towards the middle of the sample. Figure 5(*i*) shows an optically magnified view of the upper transformation region boundary. Figures 5(*j*) and 5(*k*) are for an intermediate unloading and full unloading, respectively. Lastly, Fig. 5(*l*) shows the image for full unloading but with the carrier removed.

Figure 6 shows the stress versus strain behavior using both the global measurements denoted by the solid line and the full-field measurements denoted by the open circles and connected by the dashed line. Note that the full-field results show that the local strain is either in the 0 to 1% range or in the 3.5–5% range in the austenite and martensite, respectively. Strains between these two appear only in the global measurements. Measurements of parent phase and transformation zone dimensions along with the measured strain values for each were used to compute an effective global strain estimate. The results of these calculations agreed exceptionally well with the measured global strain measurement.

Figure 7 shows a sequence of images of wrapped fringes of the tensile unloading for a representative sample processed according to Treatment A. Here the material was tested at a temperature below the active A_f temperature (22°C) but well above the R_f temperature. Figure 8 shows the stress versus strain behavior using both the global measurements denoted by the solid line and the full-field measurements denoted by the open circles and connected by the dashed line.

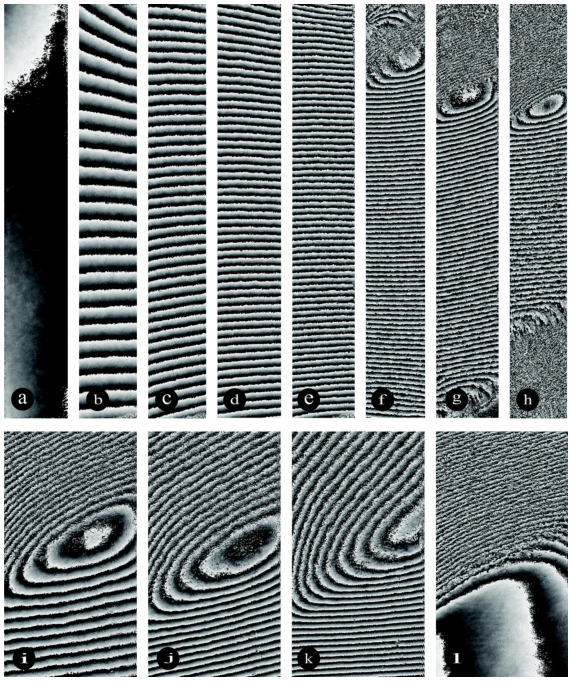

FIG. 5—*Sequence of images of unwrapped fringes during the tensile loading and close-up of unloading of material B.*

Bend Test Results

Figure 9 shows a sequence of images of wrapped fringes of the four-point bending for a representative sample processed according to Treatment A. Figures 9(*a*)–9(*c*) are for increasing load. Figure 9(*d*) is for nearing full unloading. Figures 9(*e*)–9(*h*) are for load reversal and up to nearing full unloading. The images clearly show that there is asymmetry in the tensile and compressive behavior material which is reflected in the off-center location of the neutral axis. Analysis of the fringe patterns clearly showed that the strain varied linearly through the cross section of the beam for both material treatments and all test temperatures investigated.

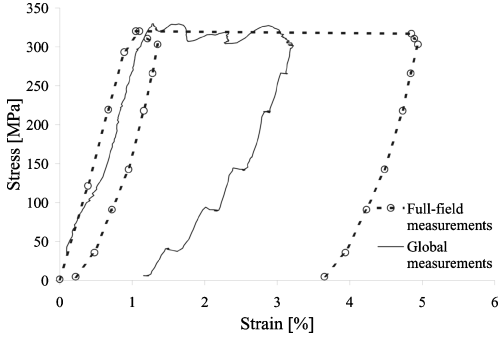

FIG. 6—*Stress versus strain behavior for material B using both the global and full-field measurements.*

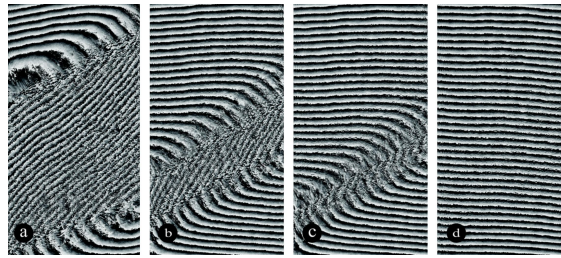

FIG. 7—*Sequence of images of unwrapped fringes during the tensile unloading of material B showing the disappearance of the transformation zone.*

Figures 10 and 11 shows the global load versus full-field strain measurements at the top and bottom edges of the sample during loading and reverse loading under four-point bend for representative samples processed according to Treatments A and B, respectively. In both cases the strains on the tensile side were higher than the strains on the compressive side of the specimen.

Reverse loading for a representative sample processed according to Treatment A showed a clear difference in measured response presumably indicating the influence of the strong R-phase component present in this material. The sample processed according to Treatment B and tested under four-point bending showed no residual strain since unlike the tensile test results presented for this treatment, this test was performed at 24°C that is above the A_f temperature of this treatment.

In both the forward and reverse loading of the sample treated according to Treatment B and the forward loading of the sample treated according to Treatment A, the ratio of the measured strains on the top edge and the bottom edge of the sample remained constant. This ratio was larger for the case of the sample treated according to Treatment B.

Discussion

The Utility of the Full-field Measurements

The technique of phase shifted moiré is shown here to provide accurate and reliable measurements of strain in both the parent and transformed phases of Nitinol under tensile and four-point bending with large deformations. The utility of such measurement results depends on the available measurement range and sensitivity of the measurement system which in turn depends directly on the quality of the fringe patterns.

Grating Quality—The quality of a fringe pattern is strongly affected by the performance of the diffraction grating. Diffraction gratings used for moiré interferometry must be efficient diffractors, espe-

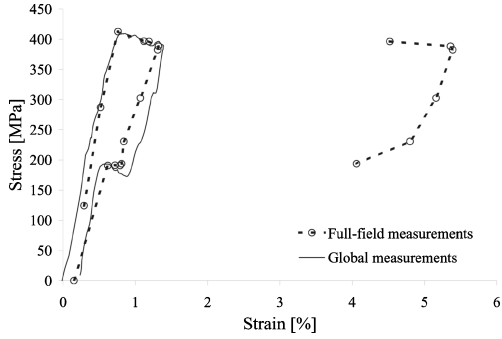

FIG. 8—*Stress versus strain behavior for material A using both the global and full-field measurements.*

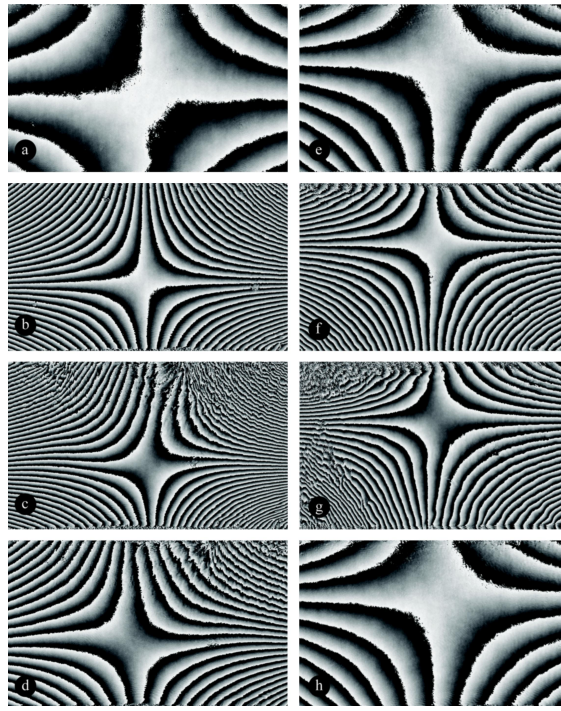

FIG. 9—*Sequence of images of unwrapped fringes during loading, unloading and reverse loading under four-point bending of material A.*

cially in the ±1 diffraction orders and they must be excellent reflectors. The gratings also must be adequately thin to minimize shear lag [8] and to not obscure fine spatial detail. Very thin (zero-thickness) photoresist gratings exposed in situ have been shown to clearly reveal edges and other microstructural details in Nitinol [11,15], but are difficult to pattern over large areas and tend to have higher background noise than replicated gratings.

Alternatively, thin epoxy replicated gratings were used in this work to provide an exceptional optical signal at the expense of slightly obscured spatial detail. This was an acceptable trade-off as the strain measurements of concern were made over significantly larger gage lengths than would be affected by the

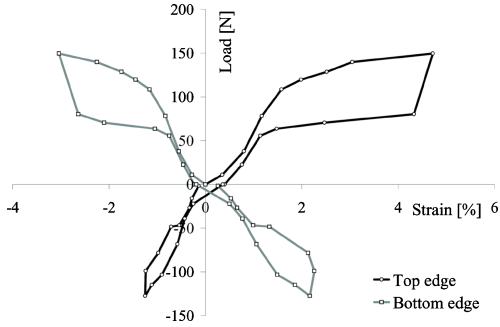

FIG. 10—*Global load versus full-field strain measurements at the top and bottom edges of the sample during loading and reverse loading under four-point bend for material A.*

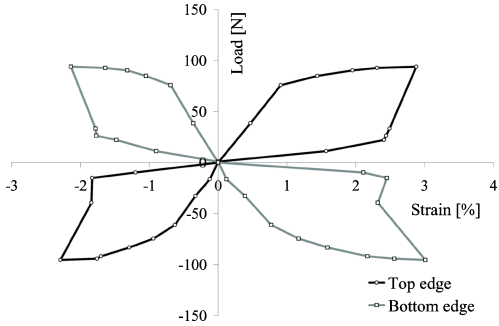

FIG. 11—*Global load versus full-field strain measurements at the top and bottom edges of the sample during loading and reverse loading under four-point bend for material B.*

thickness of the grating. Nonetheless, the thin epoxy gratings used for this work did exhibit shear lag effects most notably as viscoelastic relaxations of the grating (lasting on the order of seconds) after abrupt load changes.

Specimen reflectivity is directly affected by large deformations and the transformation process. The gratings used in this work proved extremely rugged and did not show any degradation in signal quality for the relatively small number of loading cycles considered, even while the physical appearance of the gratings was affected even after a single loading cycle producing localized phase transformation.

Carrier Fringes—Not unlike other full-field strain measurement techniques such as digital image correlation or speckle interferometry to name a few, there is an inherent trade-off between sensitivity and measurement range with the technique of moiré interferometry. Too much sensitivity results in more fringes than can be resolved with a digital acquisition system (a requirement for phase shifting) and too little resolution obviously reduces the precision of the displacement and strain measurements.

For these experiments the technique of carrier fringes was used to increase the range over which phase shifted measurements could be made while preserving the use of a high density grating. Carrier fringes do not add any additional optical information, they simply provide more or less fringe centers on which measurements are based [8].

Various methods for introducing the carrier fringes and for validating the measurements produced by this method were explored. The method chosen for these experiments was confirmed to produce a repeatability better than 0.02 % strain. Slight modifications of the interferometer were required to maintain optimal beam coverage over the large range of optical system adjustment required for the measurements presented herein. Phase shifting proved particularly helpful in analysis of the carrier frequency fringe patterns as it clearly distinguishes the sign of the optical wave front.

The Importance of Test Sample Design

Specimens Cut from Tubes—Fabrication of the test samples from seamless drawn tubing was chosen because of the importance of tubing to medical device applications and because processing is known to affect texture and, hence, the properties of Nitinol. As described in [16], equivalent thermomechanical processing can be used to reproduce the desired material response from samples scaled to different physical dimensions. By utilizing samples produced from tubing, we have demonstrated a technique that has great utility for medical devices and their applications.

Effect of Loading Configuration—The design of a single sample geometry capable of being tested in both simple uniaxial tension and pure four-point bending enabled us to explore differences between alternative loading configurations with a high degree of consistency.

Previous moiré interferometry results [11] have already demonstrated the effects of localization in the production of Lüders-type bands in uniaxial tension. Our current results have now confirmed that local-

ization also occurs in samples tested under four-point bending. The degree and uniformity of the localization is markedly different from that produced in tension, most likely a result of the more controlled strain state produced in bending.

Furthermore, for the representative sample processed according to Treatment A, noticeable nonrecovered strain was evident after the forward loading cycle and prior to reverse loading. Although not apparent in the global tensile test results, the effect of this was clearly evident in the plot of full-field strain for this sample in bending (Fig. 10).

Observation of Trends for the Different Processing Histories

The samples treated according to Treatment A required higher loads to induce transformation than the samples treated according to Treatment B. They also appeared stiffer in loading and exhibited more dramatic localization effects. Although not directly apparent in the global test results, the presence of the R-phase contributed significantly to the difference observed in the transformation strain behavior of the two treatments.

Conclusions

Measurements of strain were made simultaneously in both the parent and transformed phases of Nitinol for two distinct loading configurations. Comparisons were made to global measurements of strain to highlight the need for the correct interpretation and use of such measurements for calibrating material models describing Nitinol.

The strain data presented for the two material heat treatments were congruent with the bend free recovery data when the test temperatures are taken into consideration. For Treatment A, both tensile and bend tests were performed at the same temperature (22°C) that was slightly below the material's A_f of 25.4°C. Only a small residual strain was measured, however, due to the relatively large proportion of R-phase clearly indicated in Fig. 3. For Treatment B, a comparatively larger residual strain was measured for the tensile test, that was conducted at 19°C (below the A_f for this material), while no appreciable residual strain was measured for the bend test conducted at 24°C (above the A_f for this material).

The success of any predictive engineering methodology depends upon accurate measurement of material behavior. Global measurements, such as far-field load and extension, obtained during uniaxial tensile testing ignore local transformation effects and provide only a limited representation of the material's true behavior. Furthermore, remarkably different behavior can often be observed under different loading scenarios indicating the need for understanding the influence of multidimensional stress states.

Lastly, our results further demonstrate the need to fully consider the differences between the elastic responses of the two material phases [17] in both tension and compression when describing the phase transformation process.

Acknowledgments

The authors would like to gratefully acknowledge the contributions of Randy Lloyd and Nate Stevens from the Idaho National Laboratory and Mark Will at EDM Tek.

References

[1] Miyazaki, S. and Otsuka, K., "Development of shape memory alloys," *ISU International*, Vol. 29(5), 1989, pp. 353–377.

[2] Pelton, A. R., DiCello, J., and Miyazaki, S., "Optimization of Processing and Properties of Medical-Grade Nitinol Wire," in *SMST-2000: Proceedings of the International Conference on Shape Memory and Superelastic Technologies*, S. M. Russell and A. R. Pelton, eds. International Organization on SMST, Pacific Grove, California, 2001, pp. 361–374.

[3] Sczerzenie, F. and Gupta, S., "The Effect of Alloy Formulation on the Phase Transformation Temperature Range of NiTi Shape Memory Alloys," in *Proceedings of the International Conference on Superelastic and Shape Memory Technologies*, 2003, pp. 15–22.

[4] Duerig, T. W. and Zadno, R., Engineering Aspects of Shape Memory Alloys. 1990, pp. 369–383.
[5] Lim, T. J. and McDowell, D. L., "Cyclic Thermodynamic Behavior of a Polycrystalline Pseudoelastic Shape Memory Alloy," *J. Mech. Phys. Solids*, Vol. 50, 2002, pp. 651–676.
[6] Frick, C. P., Ortega, A. M., Tyber, J., Gall, K., and Maier, H. J., "Multiscale Structure and Properties of Cast and Deformation Processed Polycrystalline NiTi Shape-Memory Alloys," *Metall. Mater. Trans. A*, Vol. 35A, 2004, pp. 2013–2025.
[7] Imbeni, V., Mehta, A., Robertson, S. W., Duerig, T. W., Pelton, A. R., and Ritchie, R. O., "On the Mechanical Behavior of Nitinol Under Multiaxial Loading Conditions and in situ Synchrotron x-ray," in *Proceedings of the International Conference on Superelastic and Shape Memory Technologies*, 2003, pp. 267–276.
[8] Post, D., Han, B., and Ifju, P., *High Sensitivity Moiré*. Springer-Verlag, 1994.
[9] Epstein, J. S., Graham, S. M., Perry, Jr., K. E., and Reuter, W. G., "Displacement and Strain Fields for a Bimetallic Strip Under Remote Tension," *ASME J. Appl. Mech.*, Vol. 62, 1995, pp. 997–1004.
[10] Labossiere, P. E. and Perry, K. E., "The Effects of Notches and Grain Size on Transformations in Nitinol," in *Proceedings of the International Conference on Superelastic and Shape Memory Technologies*, 2003.
[11] Perry, K. E. and Labossiere, P. E., "Phase Transformations in Nitinol and Challenges for Numerical Modelling," in *Medical Device Materials II*, ASM International, 2004, pp. 131–134.
[12] Sun, Q-P., Xu, T. T., and Zhang, X., "On Deformation of A-M Interface in Single Crystal Shape Memory Alloys and Some Related Issues," *Trans. ASME, J. Appl. Mech.*, Vol. 121, 1999, pp. 38–43.
[13] Perry, Jr., K. E. and McKelvie, J., "A Comparison of Phase-Shifting and Fourier Methods in the Analysis of Discontinuous Fringe Patterns," *Optics and Lasers in Engineering*, 19(4–5), 1992. (Special issue on fringe analysis).
[14] Deason, V. A. and Ward, M. B., "A Compact Portable Diffraction Moiré Interferometer," in *Laser Interferometry: Quantitative Analysis of Interferograms*, Vol. 1162, SPIE, Bellingham, Washington, 1989, pp. 26–35.
[15] Perry, K. E., Labossiere, P. E., and Steffler, E. D., "Phase Shifted Moiré Interferometry for Accurate Characterization of Superelastic NiTi," in *Proceedings of the Society for Experimental Mechanics 2004 Spring Meeting*. The Society for Experimental Mechanics, 2004.
[16] Kugler, C., Matson, D., and Perry, K. E., "Non-zero Mean Fatigue Test Protocol for NiTi," in *SMST-2000: Proceedings of the International Conference on Shape Memory and Superelastic Technologies*, S. M. Russell and A. R. Pelton eds. International Organization on SMST, Pacific Grove, California, 2001, pp. 409–417.
[17] Liu, Y. and Yang, H., "The Concern of Elasticity in Stress-Induced Martensite Transformation in NiTi," *Mater. Sci. Eng., A*, Vol. A260, pp. 240–245, 1999.

Journal of ASTM International, Vol. 3, No. 6
Paper ID JAI100383
Available online at www.astm.org

V. Demers,[1] *V. Brailovski,*[1] *S. Prokoshkin,*[2] *K. Inaekyan,*[2] *E. Bastarash,*[1] *I. Khmelevskaya,*[2] *and S. Dobatkin*[3]

Functional Properties of Nanostructured Ti-50.0 at % Ni Alloys

ABSTRACT: Ti-50 at % Ni alloy wire is subjected to cold-rolling (true strain e=0.3–1.9) and post-deformation annealing (200–700°C range). For all levels of cold work, the maxima of recovery strain and stress are obtained after annealing in the 350–400°C range. For the moderately-to-high cold-worked material (e=0.3–0.88), this annealing leads to polygonization, while for the severely cold-worked one (e=1.9), to the material nanocrystallization (grains of 50–80 nm in size). Nanocrystallized alloy generates 30 % higher recovery stresses (up to 1450 MPa) and 10 % higher completely recoverable strains (more than 8 %) as compared to the polygonized alloy, while having comparable mechanical properties in tension.

KEYWORDS: nickel-titanium shape memory alloys, nanocrystalline structure, severe plastic deformation, post-deformation annealing

Introduction

Classic thermomechanical treatment (TMT) is shown to be a powerful method for improving such SMA properties as recovery stress and recovery strain, through the creation of a polygonized substructure containing 0.1 to 1 μm subgrains within a 20 to 40 μm fine grain structure [1]. It should be stated, however, that nearly all resources offered by the classical TMT technology (normally limited to low and moderate levels of strain varying from 20 to 40 %) seem so far to have been completely exploited, and the technology no longer offers much room for further improvement.

On the other hand, nanostructural materials have attracted considerable interest in the past few years owing to their unique mechanical properties, which combine high strength with high material ductility [2]. It is quite logical that modern interest in nanostructural materials is transposed to SMA; we must recall that already as far back as the early '90s, it was found that the cold-rolling of Ti-Ni and Cu-Al-Mn alloys to up to 50–70 % of their thickness reduction leads to partial bulk material amorphization and crystal refinement [3,4]. It was recently proven that the Ti-Ni alloy thus amorphized demonstrates, after annealing, a stable homogeneous nanocrystalline structure [5,6], which could be suitable from a material properties point of view. A detailed investigation of the TMT, consisting in amorphizing cold-rolling and nanocrystallizing annealing, and its effects on the functional properties in a connection with the microstructure and substructure of Ti-Ni alloys has been slow to emerge so far and, therefore, represents the main goal of this work.

Approach Proposed

In previous works, the level of cold work strain varied within 20–40 % limits, while the post-deformation annealing temperature was selected in the 400–700°C range. Following the objectives stated for the actual work, the deformation range is extended up to a true strain of around two to explore the possibility of

Manuscript received February 2, 2006; accepted for publication March 20, 2006; published online April 2006. Presented at ASTM Symposium on Fatigue and Fracture of Medical Metallic Materials and Devices on 7–11 November 2005 in Dallas, TX; M. R. Mitchell and K. L. Jerina, Guest Editors.

[1] Ph.D. Student, Professor, and Ms. Eng. Student, respectively, Ecole de Technologie Superieure, 1100, Notre-Dame Street West, Montreal (Quebec), Canada, H3C 1K3. Corresponding author: e-mail: vbrailovski@mec.etsmtl.ca

[2] Professor, Ph.D. Student, and Researcher, respectively, Moscow State Institute of Steel and Alloys, Leninsky prosp. 4, Moscow 119 049, Russia.

[3] Professor, Baikov Institute of Metallurgy and Material Science of RAS, Leninsky prosp. 49, Moscow, Russia.

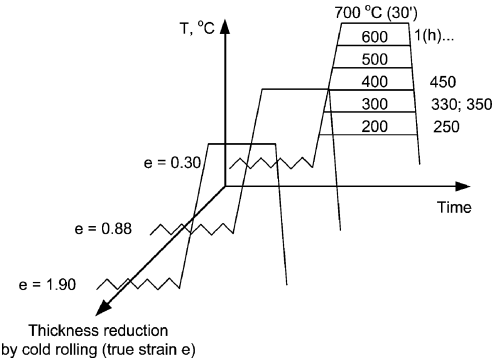

FIG. 1—*The entire cold work/annealing diapason of the study.*

amorphizing the material, while the annealing temperatures are lowered down to 200°C to keep the higher level of the material hardening, and thus to improve the resistance of the material to plastic deformation (Fig. 1).

The higher limit for the PDA temperature corresponds to the recrystallizing or "reference" thermal treatment (700°C), and the lower limit, to a starting temperature for either thermal recovery (200°C for the moderately cold-worked material), or nanocrystallization (300°C for the highly and severely cold-worked partially amorphized material). The higher limit for the cold work strain (e=1.9) refers to the maximum strain, which could be generated by conventional cold-rolling, while the lower limit (e=0.3) corresponds to the strain that initiates significant changes in the dislocation substructure. The study involves measurements of thermomechanical properties of Ti-50.0 at %Ni alloy by means of Differential Scanning Calorimetry (DSC) and tensile testing. Functional properties are measured by free recovery and constraint recovery stress generation techniques. In order to support interpretation of obtained results, a microstructure analysis is carried out by Transmission Electron Microscopy (TEM).

Materials and Experimental Techniques

This study involves the investigation of the solution treated Ti-50.0 at % Ni alloy (reference temperatures of phase transformation: $M_f=14°C$, $M_s=60°C$, $A_s=80°C$, $A_f=118°C$) supplied by the Central Research Institute for Materials (St. Petersburg). A ∅0.9 mm wire is cold-rolled using 4-046 Fenn rolling mill to obtain 0.3, 0.88, and 1.9 (from three to six passes, respectively) logarithmic thickness reductions. Flat rolling without lubrication and longitudinal tension is performed at a speed of 2 m/min. The deformed strip-type specimens are then annealed in the 200–700°C temperature range (0.5 h for annealing at 700°C and 1 h for other temperatures), and finally water-quenched to room temperature. Small surface cracks observed after severe cold-rolling (e=1.9) are removed by mechanical polishing prior to testing.

The Differential Scanning Calorimetry is performed using a Perkin-Elmer Pyris DSC with a scanning rate of 10°C/min. The lower limit for the temperature scanning is −50 (or −170°C), while the upper limit (150°C) is kept below the temperature of the post-deformation annealing (PDA) to not alter the structural state of the material during testing.

The oxidized surface layer was removed from the sample by chemical polishing in the hydrofluoric and nitric acids and hydrogen peroxide ($1HF+3HNO_3+6H_2O_2$) solution. The DSC samples, with a mass varying between 50 and 90 mg were cut with a low speed diamond saw from the thermomechanically processed wires.

To perform tensile testing, two different stress-strain curves using identically processed but separate specimens are plotted at a given testing temperature: (1) loading-unloading curve up to about 4 % of total strain, and (2) loading curve up until the specimen's fracture. The testing temperature is varied between −18°C and +200°C by 20–30 deg to represent all possible kinds of SMA mechanical behavior: martensite reorientation/detwinning or stress-inducing, elastic and plastic deformation of the reoriented or stress-induced martensite; elastic and plastic deformation of the austenite. First, thermomechanically-processed

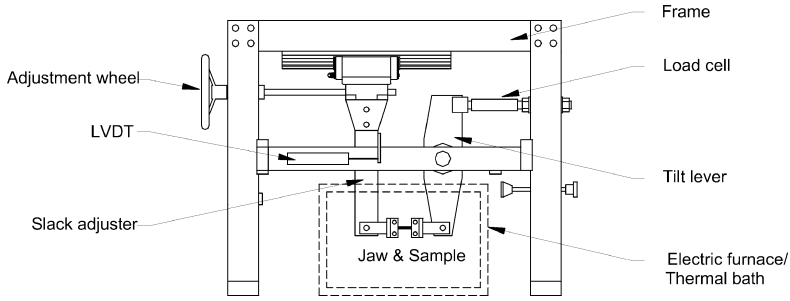

FIG. 2—*Experimental bench for tensile testing and recovery stress measurement.*

specimens with an effective length of 70 mm are set in the jaws of a specialized experimental bench (Fig. 2), and the temperature in the working zone of the bench is equilibrated at a given test temperature. The test temperature is reached on cooling from the A_f temperature in order to guarantee the same phase state of the specimens prior to testing. Then, the tensile test is performed. The force, elongation, and temperature of the specimen are measured by a load cell (S-beam), a displacement transducer (LVDT), and a thermocouple (K-type). Low and high temperatures are ensured, respectively, by a thermal bath and an electric furnace. A LabView acquisition system allows the simultaneous measurement and recording of force, displacement, and temperature data.

For constraint recovery stress measurements, the same testing bench is used (Fig. 2). A specimen is first deformed up to a given total strain at an initial temperature (T_i close to M_s) then released to allow an elastic springback, and finally set at a given initial strain, $\varepsilon_i = 2-12$ %. The constraint specimen is then heated to up to 250°C, cooled back to T_i and the "stress-temperature" curve thus generated, is plotted.

The free strain recovery measurement in bending [7] involves the following steps: (1) heating a strip-type specimen of 10 to 20 mm in length up to A_f temperature, followed by cooling to M_s temperature; (2) wrapping the specimen around a cylindrical mandrel and releasing it to allow an elastic springback, and (3) heating the specimen once again to its completely austenitic state. An initial outer fiber strain is calculated in the martensitic state: $\varepsilon_i = \varepsilon_t - \varepsilon_e$, where ε_t is the total strain and ε_e, the elastic strain prior to shape recovery. The recoverable strain is calculated in the austenitic state: $\varepsilon_r = \varepsilon_i - \varepsilon_f$, where ε_f is the residual strain after shape recovery. In both cases, the maximum strain in the outer fiber is determined as $\varepsilon = t/2r$, where t is the specimen thickness and r, the curvature radius. To determine the maximum completely recoverable strain $\varepsilon_{r,1}^{max}(\varepsilon_r = \varepsilon_i)$, the outer fiber strain in the martensitic state is incrementally increased, and the recoverable strain is plotted as a function of the initial strain.

The transmission electron microscopy (TEM) study is carried out using a JEM-100 C microscope. Thin foils are prepared using the "window" technique and electrolytic polishing in an $HClO_4 + CH_3COOH$ solution.

Results Obtained and Discussion

DSC Testing

Two important observations can be made from the analysis of the DSC thermograms (Fig. 3):

1. For all levels of cold work followed by high-temperature annealing (PDA higher than 650°C), direct martensitic transformation follows the one-stage transformation pass (characterized by a single DSC peak), while manifesting the appearance of a multi-stage transformation after lower-temperature annealing (characterized by a double DSC peak). The presence of a double peak on cooling is definitely to be attributed to the appearance of an intermediate R-phase. The presence of a double peak on heating can also be noticed (after cold-rolling at a true strain of e = 0.3–0.88 and 300–500°C annealing), but its interpretation is much more intricate because it can be attributed either to the reverse $B19' \rightarrow R \rightarrow B2$ transformation or to the material heterogeneity. Since the reverse transformation from B19′ to B2 does not have an energy advantage

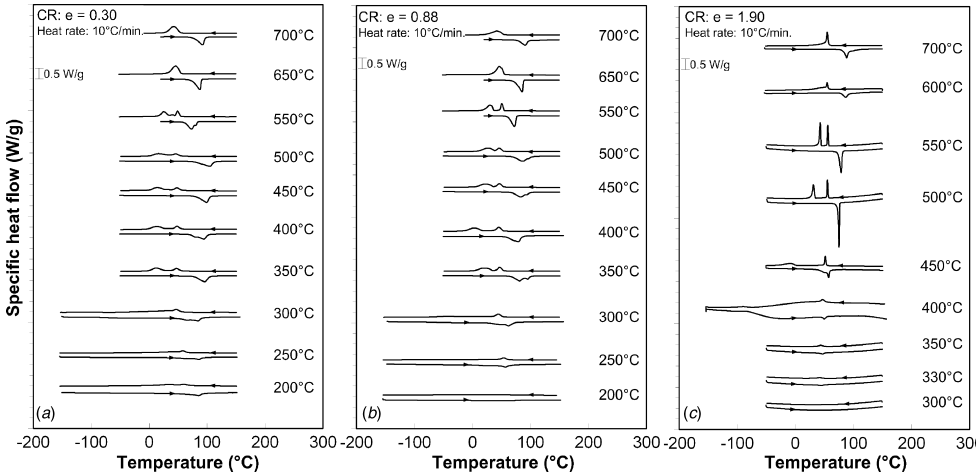

FIG. 3—*DSC thermograms of Ti-50.0 at % Ni alloy after thermomechanical treatments.*

from passing through an intermediate R-phase, it seems reasonable to attribute this phenomenon to the heterogeneity of the cold-rolled structure [8–10]. This interpretation is supported by the fact that while two DSC peaks can be observed on heating after a cold work of e=0.3–0.88, only a one-stage transformation is visible after a cold work of e=1.9 (Fig. 3). This difference can be explained by supposing that after a true strain of e=1.9, a large volume of the material crystallizes from an amorphous matrix, thus contributing to the material's structural homogeneity. To verify this interpretation, further investigation using a combined DSC and in situ diffractometry techniques is needed.

2. The DSC transformation peaks measured after the PDA of the 1.9 cold-worked material are sharper, and the hysteresis between direct and reverse transformations, is narrower than those of the 0.3–0.88 cold-worked material. This phenomenon is due to the fact that there are a smaller number of obstacles for interface movement after the former processing than after the latter. It is believed to be due to a significant difference in structure and microstructure resulting from the moderate-to-high (e=0.3–0.88) and severe (e=1.9) cold-work processing. The moderately cold-worked material is characterized mainly by its dislocation substructure, while the severely cold-worked one, is by its ultra-fine grain structure. For a material with the same grain size, the higher the dislocation density, the more extended the temperature range of martensitic transformation. It is the same for a material with an identical dislocation density, but with a finer grain structure. The fact that the DSC peaks for the 0.3–0.88 cold-worked material are broader and the thermal hysteresis of transformation, larger than those for the 1.9 cold-worked material can be explained by supposing that an increase in dislocation density has a greater impediment effect on the interface movement than does a decrease in grain size.

From DSC thermograms, two types of data are extracted: latent heat (Fig. 4) as well as the start and finish temperatures for the direct and reverse transformations (Fig. 5).

On the one hand, Fig. 4 shows that the higher the level of cold work, the higher the onset PDA temperature that allows the complete martensitic transformation to occur. For cold work varying from e =0.3 to 1.9, this onset PDA temperature increases from 250 to 500°C (indicated by the dashed arrows in Fig. 4). The lower the PDA temperature, the lower the latent heat of transformation, thus reflecting a gradual increase in dislocation density, which impedes the interface movement, and in the quantity of the retained austenite, which decreases the completeness of the transformation. The higher the cold-work strain, the more pronounced this trend.

On the other hand, Fig. 5 indicates that on cooling, the temperature range of the R-phase transformation remains relatively stable irrespective of the thermomechanical processing conditions, while the R

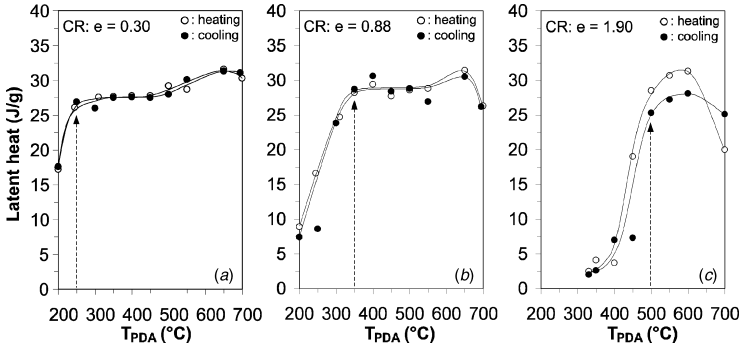

FIG. 4—*Latent heat of transformation as a function of the annealing temperature: (a) cold-rolling: e =0.3; (b) e =0.88, and (c) e =1.9.*

→B19′ temperature range is depressed to lower temperatures when the annealing temperature decreases. The higher the cold work, the more pronounced the gap between these two transformations and the broader the transformation peaks.

On heating, the temperature range of the reverse martensitic transformation (B19′→B2) remains relatively stable after polygonizing annealing (300–450°C). When the annealing temperature decreases to under 350°C, the temperature range of the transformations broadens and shifts to lower temperatures, and the higher the cold work, the more pronounced this trend (represented by the shaded area in Fig. 5).

Tensile Testing

Isothermal tensile testing plots for Ti-50.0 at % Ni specimens subjected to cold work (true strain of e =0.3, 0.88, and 1.9) and annealing (200–700°C temperature range) are obtained. The evolutions of the onset stress for martensite reorientation or stress-induced formation (σ_{cr}) and of the true yield stress (σ_y) as functions of the testing temperature are extracted from tensile curves and presented in Fig. 6. These data are regrouped in respect to the structural phenomena observed in the alloy following different TMT, such

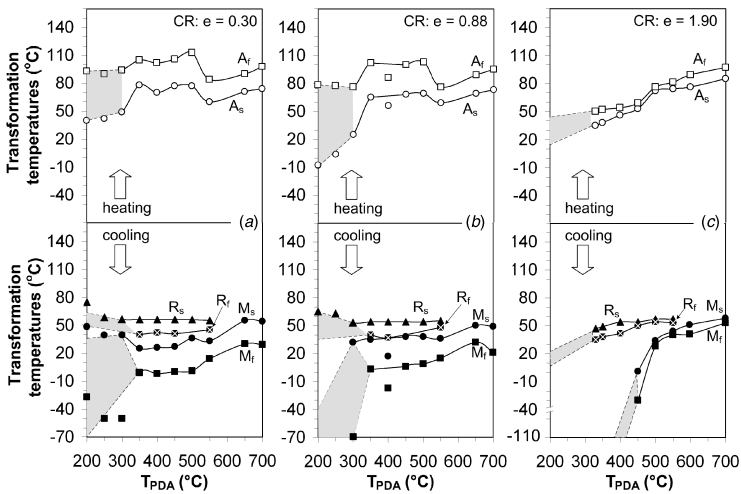

FIG. 5—*Transformation temperatures as a function of the PDA temperature for three levels of cold work (a) e =0.3; (b) e =0.88, and (c) e =1.9.*

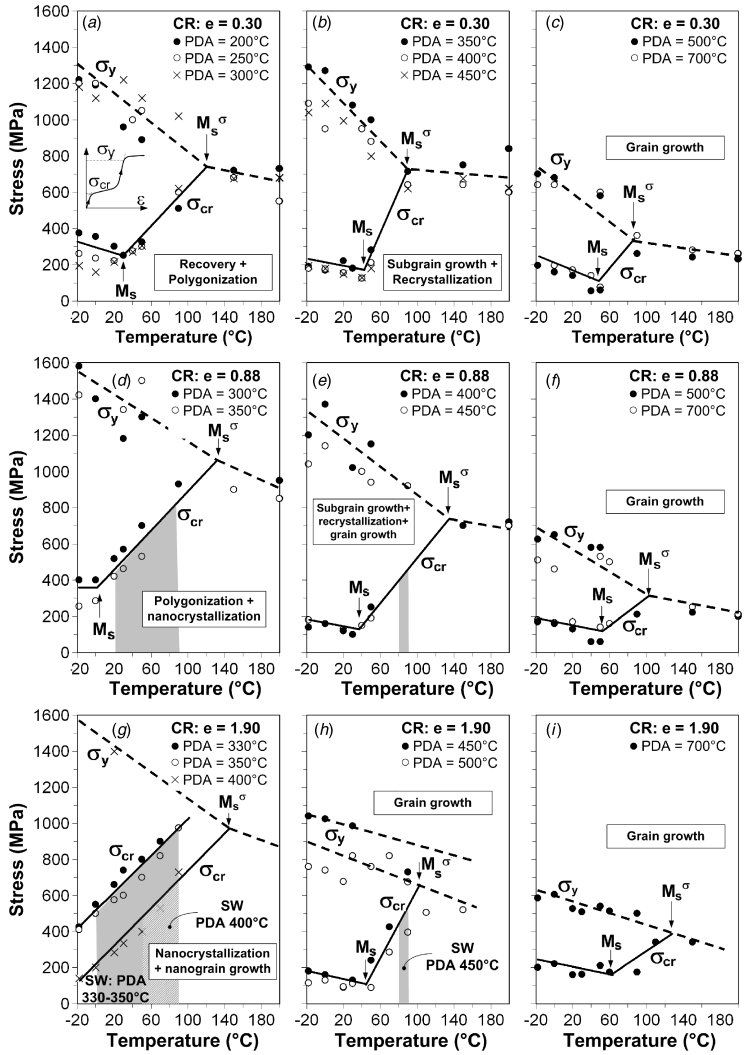

FIG. 6—*Evolution of the onset stress (σ_{cr}) and the true yield stress (σ_y) as a function of the testing temperature for the Ti-50.0at %Ni alloy processed by cold-rolling (CR) and annealing (PDA). The shaded and dashed areas represent the Superelastic Windows (SW).*

as recovery, polygonization, and recrystallization (for dislocation hardened material: e=0.3–0.88); nanocrystallization and grain growth (for amorphized material: e=1.9). This arrangement is consistent with TEM results.

- For a moderate cold work (e=0.3), annealing at 200–300°C corresponds to the static recovery and polygonization stage (Fig. 6(*a*)); at 300–450°C, to the subgrain growth and partial recrystallization (Fig. 6(*b*)); at 450°C and higher, to the recrystallization and grain growth (Fig. 6(*c*)).
- For a severe cold work (e=1.9), annealing at 300–400°C corresponds to the nanocrystallization of the amorphous regions and to growth of nanograins in the initially nanocrystalline regions (Fig. 6(*g*)); and at 450–500°C and higher (Fig. 6(*h*), Fig. 6(*i*)), to the nanograins growth stage.
- For a high cold work (e=0.88), which combines the structural features of moderate and severe

cold works, annealing at 300–350°C corresponds to the polygonization and subgrain growth, and to the nanocrystallization of the amorphous regions (Fig. 6(*d*)); annealing at 400 and 450°C, to the subgrain growth, recrystallization and grain growth (Fig. 6(*e*)). Annealing at higher temperatures corresponds to the grain growth stage (Fig. 6(*f*)).

For all cold work levels, the lowering of the annealing temperature causes a depression of the M_s temperature accordingly to the depression of the temperature range for the direct martensitic transformation. Since the M_s temperature is the testing temperature that allows the lowest onset stresses σ_{cr}^{min} to be obtained, the lower the annealing temperature, the lower then will be the testing temperature corresponding to σ_{cr}^{min}. In parallel, the lower the annealing temperature, the higher the M_s^{σ} temperature corresponding to the maximum temperature for the martensite induction under stress. These two simultaneous trends result in a widening of the temperature range between M_s and M_s^{σ}.

For all cold work levels, the lower the annealing temperature, the higher the minimum onset stress σ_{cr}^{min} and the yield stress $\sigma_y^{M_s}$ (determined at the same temperature as σ_{cr}^{min}), while the difference between these two parameters ($\sigma_y^{M_s} - \sigma_{cr}^{min}$) passes through a maximum in the 200–400°C PDA range. The higher the level of cold work, the more significant the increase in $\sigma_y^{M_s}$, σ_{cr}^{min} and ($\sigma_y^{M_s} - \sigma_{cr}^{min}$). This trend is more pronounced for an e=0.88 cold work than for an e=0.3 cold work and, more specifically, for the low-to-moderate temperatures of annealing (350–400°C). Note, however, that for the low-temperature annealing, the more intensive the cold work, the higher the onset stresses and the closer the material fracture to the brittle one. Consequently, for highly hardened materials, it becomes difficult to retrieve true yield stresses, which come close to the ultimate strength values. A scattering of these data becomes even more pronounced after e=1.9 cold work because of the internal and external microcracks generated during severe deformation.

The widening of the ($M_s^{\sigma} - M_s$) and ($\sigma_y^{M_s} - \sigma_{cr}^{min}$) windows makes it possible for the Ti-50.0 at % Ni alloy to manifest a superelastic behavior after thermomechanical processing, consisting in high-to-severe levels of cold work (e=0.88, 1.9) and low-to-moderate temperatures of annealing (300–450°C). These superelastic windows are represented by shaded zones in Fig. 6.

- For e=1.9 cold work, the highest annealing temperature leading to superelasticity is 450°C, with a very narrow temperature window for this effect around 90°C. The lower the annealing temperature, the lower the inferior temperature limit for superelasticity. After 400°C PDA, the inferior temperature for the superelasticity window extends to 50°C; after 350°C, to 20°C, and after 330°C to 0°C. Annealing below 330°C leads to hazardous destructive mechanical testing due to the mostly brittle fracture character for such specimens.
- For e=0.88 cold work, a similar trend is observed, except that after a low-temperature PDA (200–300°C), a plateau-like superelasticity is replaced by a linear superelasticity. This fact signifies that the well developed dislocation substructure resulting from e=0.88 cold work (and preserved after low-temperature annealing) offers a higher resistance to the interface movement than does the crystallized nanostructure obtained after e=1.9 cold work.
- For an e=0.3 cold work, only a partial superelasticity is observed.

Recovery Strain and Stress Measurements

The most important functional properties of the equiatomic Ti-Ni alloy are the recovery strain and stress that can be generated. Figure 7 shows an example of the results of the bend and free recovery testing. The maximum completely recoverable strain ($\varepsilon_{r,1}^{max}$: indicated by arrows in Fig. 7) is obtained when the recovery strain becomes lower than the initial strain ($\varepsilon_r < \varepsilon_i$). On the other hand, Fig. 8(*a*) shows a typical recovery stress—temperature curves measured after a given TMT (e=0.88 and 500°C annealing) for different levels of initial strain. From these curves, for a given TMT, the maximum values of generated stresses can be plotted as a function of initial strain (Fig. 8(*b*)), thus making it possible to determine the optimum initial strain corresponding to the maximum recovery stress $\varepsilon_i(\sigma_r^{max})$. The results obtained for the maximum completely recoverable strain (pure bending) and maximum recovery stress (tension) for different thermomechanical processing are presented in Fig. 9. The TEM images corresponding to the optimum annealing temperatures for each level of cold work are also presented.

For all levels of cold work, both the completely recoverable strain ($\varepsilon_{r,1}^{max}$) and recovery stress (σ_r^{max}) reach their maxima at a given "optimum" annealing temperature (T_{opt}), which varies between 350 and

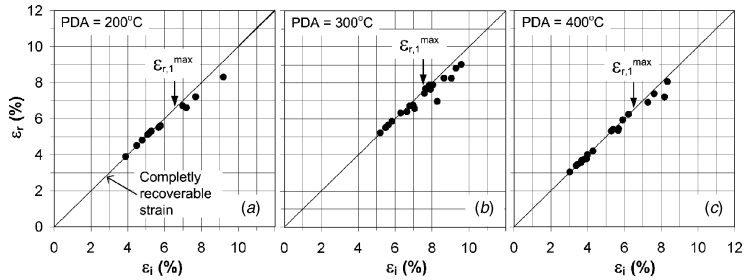

FIG. 7—*Typical results of recovery strain (ε_r) testing performed with specimens subjected to a given cold work (e = 0.3) and variable annealing temperatures 200, 300, and 400°C (arrows indicate the maximum completely recoverable strain: $\varepsilon_{r,1}^{max}$).*

400°C. The more intensive the cold work, the higher the maximum recovery stress σ_r^{max} attainable after annealing: 900 MPa (e=0.3), 1100 MPa (e=0.88), and 1450 MPa (e=1.9). The last value represents—to the best of authors' knowledge—the highest recovery stress that has so far been reported for the Ti-50.0 at % Ni alloy.

The influence of cold work on the maximum completely recoverable strain $\varepsilon_{r,1}^{max}$ is more intricate. In the cold-work diapason corresponding to the dislocation-hardening mechanism (e=0.3–0.88), the higher the cold work strain, the lower the completely recoverable strain (7.6 % for e=0.3 cold work and 6.8 % for e=0.88 cold work). This trend reflects the harmful consequences of an increase in strain-hardening on the reversibility of the martensitic transformation. (Despite this negative effect, the creation of the well developed dislocation substructure allows the material to improve its potential to generate high recovery stresses.) On the contrary, a material deformed at e=1.9 demonstrates a significant increase in $\varepsilon_{r,1}^{max}$ up to above 8 %, thus reflecting an unbiased positive influence of amorphizing and nanocrystallizing cold-work processing on the performance characteristics of Ti-Ni alloys.

TEM Study

The TEM study [11] confirms that cold-work processing is responsible for three types of material microstructure: (a) dislocation substructure, (b) nanocrystalline, and (c) amorphous structures. Post-deformation annealing leads to the distinct transformation of these peculiar structures: the dislocation substructure passes through the recovery, polygonization, and recrystallization stages; the amorphous structure crystallizes and the nanocrystalline structure, which either results directly from cold work or is crystallized from the amorphous structure, coarsens.

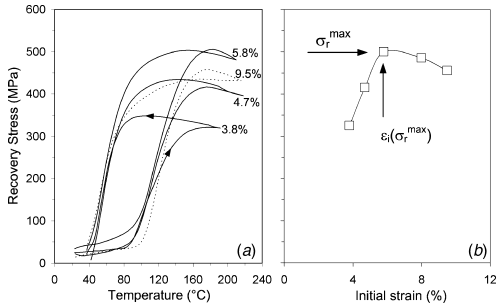

FIG. 8—*Typical recovery stress—temperature curves measured after a given thermomechanical processing (e = 0.88 + PDA500°C): (a) for different levels of strain (3.8, 4.7, 5.8, and 9.5 %); (b) recovery stress as a function of initial strain.*

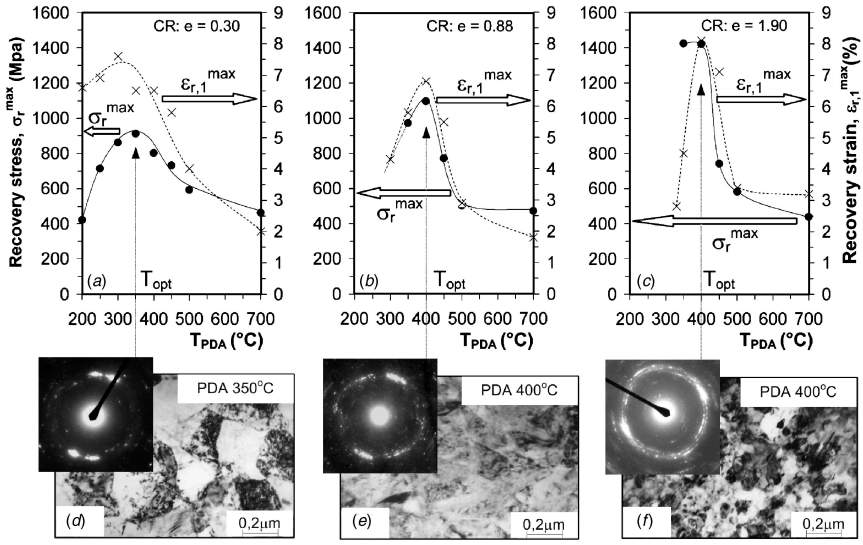

FIG. 9—*Maxima of recovery stress and completely recoverable strain (offset of 0.2 %) as functions of the annealing temperature; TEM images for the optimal annealing temperatures: (a–d) cold rolling: e = 0.3; (b–e) e = 0.88, and (c–f) e = 1.9.*

Cold-rolling at moderate-to-high levels (e=0.3–0.88) results in the formation of a well developed dislocation substructure in martensite. It should be noted that a logarithmic thickness reduction of e =0.88 gives rise to the partial formation (along with the dislocation substructure) of the nanocrystalline and even amorphous structures. Since the last two structures are not predominant, they do not represent a major factor in the resulting material properties after the PDA [5,6].

The higher the amount of cold work and therefore the higher the dislocation density, the lower the temperature required for the polygonized structure formation: 300°C for e=0.3 and 250°C for e=0.88.

Severe cold-rolling (e=1.9) is responsible for the formation of a mixed (approximately 50 %/50 %) nanocrystalline and amorphous structure in the material: nanograin (2–8 nm in size) zones are dispersed in the amorphous matrix.

Annealing at 300°C is related to the creation of a specific structure with a bimodal grain size distribution: a coarser-grain population (nanograins of about 20 nm in size) growing from nanocrystals formed during cold work and a finer-grain population (nanograins of about 5 nm in size) crystallized from the amorphous structure.

After annealing at 400°C—the optimum annealing, from a material properties point of view (see Fig. 9(*c*)–9(*f*))—the structure contains normally distributed nanograins with dimensions varying from 20 to 120 nm (50 to 80 nm for the most populous size). After annealing at 500°C, austenite grains grow to a size of 200 to 600 nm. After a reference annealing at 700°C, no marked difference can be observed in the structure resulting from various material processing instances: austenite grains have a similar size (measuring dozens of micrometres).

Conclusion

Generally speaking, the thermomechanical processing aims mainly to heighten the yield strength of a material, while facilitating the occurrence of martensitic transformation under stress. On the one hand, the hardening of the equiatomic Ti-Ni alloy can be obtained either through crystal refinement or through an increase in dislocation density (nucleation of coherent precipitates can also be the way for nickel-rich alloys), and on the other hand, the enhancement of the martensitic transformation reversibility can be obtained by a decrease in the dislocation density.

The main structural characteristic of the Ti-50.0 at % Ni alloy processed by severe cold-rolling ($e = 1.9$) and annealing (400°C) is the presence of the nanocrystalline structure combined with a relative absence of a well developed dislocation substructure, as a result of which material hardening is obtained by crystal refinement, and not by an increase in dislocation density. The nanocrystalline structure allows an increase in the true yield stress of the material, while the absence of the dislocation substructure combined with the relatively low level of onset stresses (σ_{cr}^{min}), decreases the risk of triggering deformations by slip mechanisms, and thus promotes the completeness of shape recovery and recovery stress generation. This reasoning can explain why the Ti-50.0at % Ni alloy demonstrates 30 % higher stress and 10 % higher strain recovery capabilities after $e = 1.9$ processing as compared to $e = 0.88$, while having comparable mechanical properties in tension.

After annealing at lower temperatures (350°C), the material hardening, through a continuing decrease in grain size, is accompanied by a partial suppression of martensitic transformation and, in grains smaller than 60 nm, martensitic transformation is completely suppressed [12]. That is the reason why after a PDA of 350°C, the constraint recovery stress is the same as after one of 400°C, while the completely recoverable strain is significantly lower (Fig. 9).

The main practical conclusion of this work can be resumed as follows: for equiatomic Ti-Ni alloys, nanocrystalline structure with a given grain size (60–80 nm) created by severe plastic deformation and post-deformation annealing is much more effective—from a functional properties point of view—than any dislocation (including polygonized) substructure resulted from classical thermomechanical processing consisting in plastic deformation at moderate strains combined with post-deformation annealing heat treatment.

Acknowledgments

This work had been carried out with support of the Natural Science and Engineering Research Council of Canada and the Ministry for Education and Research of the Russian Federation. The authors thank Dr. A. Korotitskiy for his support in designing the experimental test bench and Dr. E. V. Tatyanin for his support during microstructural analysis.

References

[1] Brailovski, V., Prokoshkin, S., Terriault, P., and Trochu, F., Eds., *Shape Memory Alloys: Fundamentals, Modeling and Applications*, ÉTS, Canada, 2003, pp. 403–548.

[2] Valiev, R., "Materials Science, Nanomaterial Advantage," *Nature*, Vol. 419, No. 6910, 2002, pp. 887–889.

[3] Koike, D., Parkin, M., and Nastasi, M., "Crystal-to-Amorphous Transformation of NiTi Induced by Cold Rolling," *J. Mater. Res.*, Vol. 5, No. 7, 1990, pp. 1414–1418.

[4] Dutkiewicz, J., "Plastic Deformation of CuAlMn Shape-Memory Alloys," *J. Mater. Sci.*, Vol. 29, No. 23, 1994, pp. 6249–6254.

[5] Nakayama, H., Tsuchiya, K., Umemoto, M., "Crystal Refinement and Amorphization by Cold Rolling in TiNi Shape Memory Alloys," *Scr. Mater.*, Vol. 44, No. 8–9, 2001, pp. 1781–1785.

[6] Li, Z. C., Zhao, X. K., Zhang, H., et al., "Microstructure and Superelasticity of Severely Deformed TiNi Alloy," *Mater. Lett.*, Vol. 57, No. 5–6, 2003, pp. 1086–1090.

[7] Lin, H. C. and Wu, S. K., "Strengthening Effect on Shape Recovery Characteristic of the Equiatomic TiNi Alloy," *Scr. Metall. Mater.*, Vol. 26, No. 1, 1992, pp. 59–62.

[8] Chang, S. H., Wu, S. K., and Chang, G. H., "Grain Size Effect on Multiple-Stage Transformations of a Cold-Rolled and Annealed Equiatomic TiNi Alloy," *Scr. Mater.*, Vol. 52, No. 12, 2005, pp. 1341–1346.

[9] Khalil-Allafi, J., Dlouhy, A., and Eggeler, G., "Ni_4Ti_3-Precipitation During Aging of NiTi Shape Memory Alloys and Its Influence on Martensitic Phase Transformations," *Acta Mater.*, Vol. 50, No. 17, 2002, pp. 4255–4274.

[10] Otsuka, K. and Ren, X., "Physical Metallurgy of Ti-Ni-Based Shape Memory Alloys," *Prog. Mater. Sci.*, Vol. 50, 2005, pp. 511–678.

[11] Brailovski, V., Prokoshkin, S. D., Khmelevskaya, Y., Inaekyan, K. E., Demers, V., Dobatkin, S., and

Tatyanin, E. V., "Structure and Properties of the Ti-50.0 at % Ni Alloy After Strain Hardening and Nanocrystallizing Thermomechanical Processing," *Materials Transactions*, Vol. 47, No. 3, 2006, pp. 1–10.

[12] Waitz, T., Kazykhanov, V., and Karnthaler, H. P., "Martensitic Phase Transformations in Nanocrystalline NiTi Studied by TEM," *Acta Mater.*, Vol. 52, No. 1, 2004, pp. 137–147.

Journal of ASTM International, Vol. 3, No. 5
Paper ID JAI13580
Available online at www.astm.org

Douglas J. Hornbach,[1] *Paul S Prevey,*[2] *and Edmund F Loftus*[3]

Application of Low Plasticity Burnishing (LPB) to Improve the Fatigue Performance of Ti-6Al-4V Femoral Hip Stems

ABSTRACT: Low plasticity burnishing (LPB) is a surface enhancement method that produces a deep layer of compressive residual stress with minimal cold working and an improved surface finish. Extensive fatigue testing, performed on numerous metal alloys in simulated environmental conditions, demonstrates that LPB significantly improves fatigue strength of highly stressed components. LPB is a flexible process, capable of being implemented on a wide variety of CNC machine tools. A product-specific LPB process was developed and applied to the modular neck taper junction of a Ti-6Al-4V total hip prosthesis (THP). LPB produced a compressive residual stress field with an improved surface finish, which enhanced component fatigue strength and resistance to fretting damage. X-ray diffraction (XRD) residual stress measurements, made before and after LPB application, are shown. High cycle fatigue (HCF) results obtained on LPB-processed hip stems are shown along with baseline data for unprocessed hip stems. HCF tests demonstrate complete elimination of fretting fatigue failures in the LPB processed area of the taper junction and a substantial increase in overall THP fatigue strength.

KEYWORDS: low plasticity burnishing (LPB), total hip prosthesis, residual stress, high cycle fatigue (HCF), surface enhancement, fretting fatigue

Introduction

Total hip replacement (THP) surgery is often required to alleviate pain and improve the function of hips damaged from disease or fracture. It is estimated that over 300 000 hip replacement surgeries are performed each year in the United States alone. Implanted THP systems experience a spectrum of cyclic loading from normal day-to-day patient activities. Chances of high cycle fatigue (HCF) failure of the THP increase with patient size and level of activity.

Modular THP construction has become more widely used because it gives the surgeon the opportunity to interoperatively choose the proper size prosthesis and offers flexibility in treating a wide spectrum of hip defects and patient anatomies. Modular THP systems are typically held together using a tapered interlock. Fretting can occur along the contact of the taper junction due to small displacement between the two connected subcomponents. Surface micro-cracks from fretting damage can cause a significant reduction to the high cycle fatigue strength of the THP.

The benefits of compressive residual stresses to boost fatigue strength in metallic components have long been recognized [1–4]. Many engineering components have been cold worked using various surface enhancement processes such as shot peening to improve fatigue strength. A surface enhancement process termed low plasticity burnishing (LPB) [5–9] has been shown to dramatically improve fatigue performance in components prone to damage such as foreign object damage (FOD) [10–12], fretting [13,14], and pitting/corrosion [15–18]. LPB surface treatment is applied using conventional multi-axis CNC machine tools for unprecedented control of the residual stress distribution developed through modification of the pressure, feed, and tool characteristics. Achieving deep compression with low cold work reduces relaxation of the protective compressive layer either thermally during exposures at service temperatures [19], or mechanically due to overload or impact. In addition to the deep compressive residual stress produced, LPB

Manuscript received October 7, 2005; accepted for publication January 30, 2006; published online April 2006. Presented at ASTM Symposium on Fatigue and Fracture of Medical Metallic Materials and Devices on 7–11 November 2005 in Dallas, TX; M. R. Mitchell and K. L. Jerina, Guest Editors.

[1] Vice President and Director of Laboratory Operations, Lambda Technologies.
[2] President and Director of Research, Lambda Technologies.
[3] Senior Product Development Engineer, Exactech.

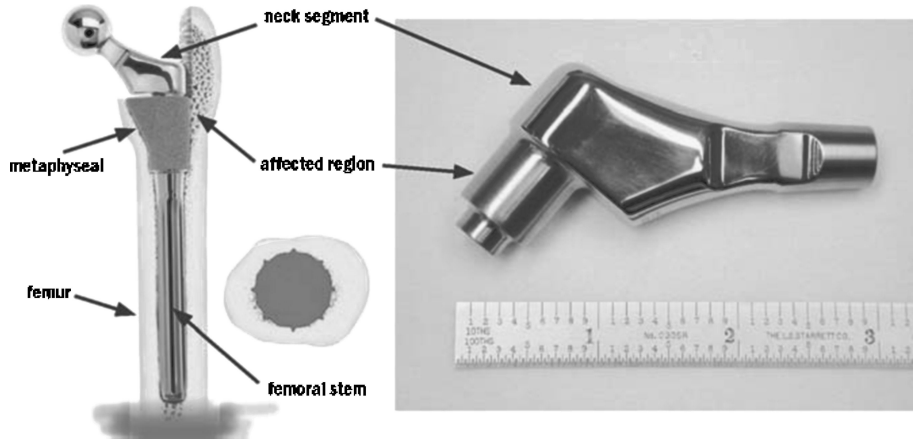

FIG. 1—*Exactech M-Series modular hip prosthesis: assembled construct (left) and neck segment (right).*

dramatically improves the finish of most machined surfaces and in some cases leaves the surface with a near mirror finish.

During a continuous improvement assessment for the Exactech M-Series modular hip prosthesis, it was hypothesized that the controlled application of compressive residual stresses to the taper surface could improve fatigue strength without altering the prosthesis geometry. The possibility of keeping the same prosthesis geometry offered important advantages, including maintaining the existing size scope and utilization of existing inventory.

An LPB process was designed to improve the fatigue strength and fretting damage tolerance of the M-Series modular hip prosthesis. A customized compressive residual stress field was developed for the tapered region of the neck stem segment using a detailed design protocol discussed in previous work [20]. Conventional roller burnishing was insufficient in terms of the compression produced and lacked the control required to produce consistent compressive residual stresses.

Experimental Method

Femoral Hip Stem Component

The Exactech M-Series Modular Hip Prosthesis is comprised of three major components that form a functional hip implant or prosthesis when assembled, as shown in Fig. 1. These components include the femoral stem, metaphyseal and neck segments, and are held together with taper interfaces and a locking screw. In service, the neck segment taper experiences high-stress loading conditions in a corrosive, fretting environment. Furthermore, every step taken by a patient represents a single loading and unloading cycle that accumulates over years of implantation. Given this aggressive use and environment, high cycle fatigue strength is critical to the successful clinical performance of hip prostheses.

Finite Element Modeling

Finite element (FE) modeling was used in the design of the compressive residual stress field of the hip stem. The model was used to estimate both the in-service applied stresses and the LPB residual stresses in the neck stem segment.

The 3-D model, shown in Fig. 2, was composed of both the femoral neck stem segment and head. The neck segment and head were treated as one continuous body. The FE model consisted of 17334 first-order brick elements and 6839 nodes. Typical solution treated and aged Ti-6Al-4V material properties were used [21].

Forces were placed on the femoral head to simulate the loads applied during fatigue testing. Applied

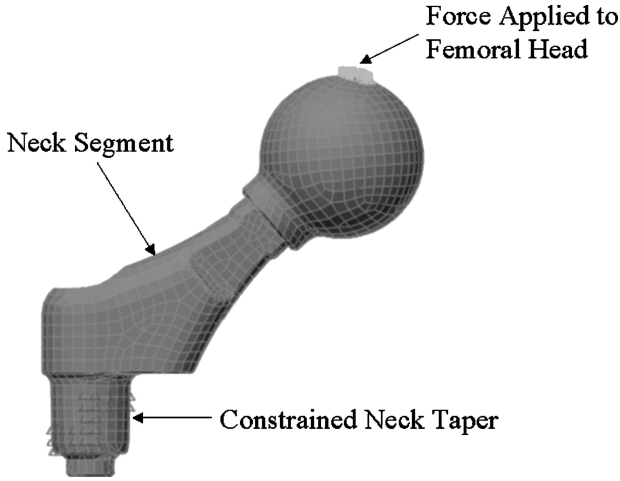

FIG. 2—*3-D finite element mesh for hip segment model.*

stresses in the tapered neck region were determined for a 1050 and 1800 lb (4671 and 8007 N) load. The 1050 lb (4671 N) load was the fatigue strength of the THP with no LPB processing and the 1800 lb (8007 N) load was the fatigue strength target for an LPB processed neck segment. Nodal constraints were placed on the neck to simulate the boundary conditions between the tapered connection of the neck and the metaphyseal.

Residual stress results measured by XRD on LPB processed neck segments were placed in the FE model to accurately simulate the compression imparted by the LPB process. No attempt was made to model the plasticity that occurs during LPB since the exact residual stresses produced by LPB were measured by XRD. Compensatory tensile residual stresses around the compressive LPB zone were also estimated with the model.

LPB Processing

CNC control code was developed to allow positioning of the LPB tool in a series of passes around the stem neck taper in a CNC lathe. Burnishing loads were controlled to develop the desired magnitude of compressive stress with relatively low cold working. Figure 3 shows a stem neck segment being LPB processed in a four-axis manipulator on the CNC milling machine.

Residual Stress Characterization

XRD residual stress measurements were made employing a $\sin^2\psi$ technique and the diffraction of copper Kα1 radiation from the (21.3) planes, of the Ti-6Al-4V. It was first verified that the lattice spacing was a linear function of $\sin^2\psi$ as required for the plane stress linear elastic residual stress model [22–25].

Material was removed electrolytically for subsurface measurement in order to minimize possible alteration of the subsurface residual stress distribution as a result of material removal. The residual stress measurements were corrected for both the penetration of the radiation into the subsurface stress gradient [26] and for stress relaxation caused by layer removal [27].

The value of the X-ray elastic constants required to calculate the macroscopic residual stress from the strain normal to the (21.3) planes of the Ti-6Al-4V were determined in accordance with ASTM E 1426-91 [28]. Systematic errors were monitored per ASTM specification E 915.

XRD residual stress measurements were made at the surface and at several depths below the surface on an as-received, roller burnished and LPB processed neck stem. Measurements were made on the processed outside diameter of the neck to characterize the depth and magnitude of the compression

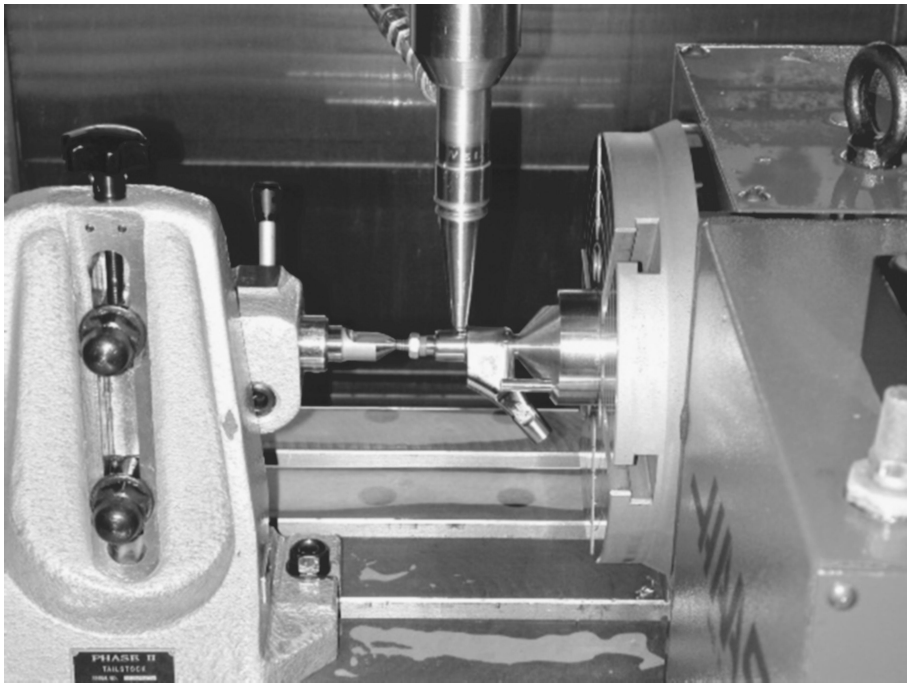

FIG. 3—*LPB processing of hip segment.*

produced. Measurements were also made on the inside diameter bore of the neck to establish any change resulting from equilibrating tension. All measurements were made at mid-length of the neck taper, at the 12 o'clock position, as shown in Fig. 4.

Residual stresses were measured at the 6 o'clock position, adjacent to the neck taper, on two neck segments following fatigue testing. Both neck segments ran out to 10^7 cycles at loads of 1400 lb (6228 N)

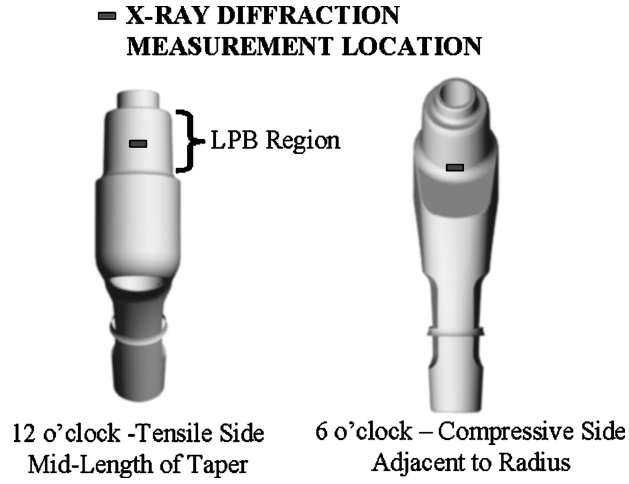

FIG. 4—*X-ray diffraction residual stress measurement locations.*

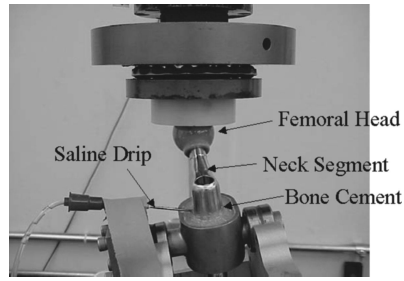

FIG. 5—*Fatigue test of THP system.*

or greater. Measurements were made to ensure the LPB compressive residual stresses were not significantly altered. The applied compression at the 6 o'clock position is added to the compressive residual stresses from LPB, providing the potential for compressive yielding. Previous studies [29] have shown that compressive residual stresses can flip to tension after bulk yielding in either tension or compression. Residual stress inversion is more likely to occur in highly cold worked surfaces. Most machining and shot peening processes produce relatively high cold working compared to LPB [19,29].

Component Fatigue Testing

High cycle fatigue (HCF) testing performed on baseline and LPB processed neck segments were conducted on a closed loop servo-hydraulic system in accordance with ISO standards 7206-4 and 7206-8 [30,31]. A photo of the fatigue test setup is shown in Fig. 5.

The metaphyseal and femoral stem were embedded in bone cement. A cyclic load was applied to the head producing bending and torsion about the processed neck region. A silicone bead was applied to seal the gap between the metaphyseal and the neck segment. A saline drip was introduced via needle injected into the silicone seal to maintain a wet saline environment at the modular taper junction.

Fatigue tests were run at an R ratio of 0.1 and a frequency of 15 Hertz. The systems were tested to failure, which was considered as a subcomponent breakage or loosening where the assembly is unable to support the applied loads. Specimen run-out was considered to be 10^7 cycles.

Baseline Fatigue Performance

To design the LPB zone it was necessary to determine the fatigue initiation site. Four fatigue tested hip stem segments, listed in Table 1, were examined optically at magnifications up to 60× and with a scanning electron microscope (SEM) to identify fatigue origins and locations thereof relative to the specimen. The fatigue loads and the corresponding life are shown in the table. Three of the four segments fractured in the tapered neck region. Specimen PR-2003-025-5 ran out to 10^7 cycles without failure to the neck.

Results and Discussion

Fractography

Figure 6 contains photographs of baseline Specimen PR-2003-025-2. Figure 6(*a*) shows the approximate location of the initiation site, which coincides with where finite element predicts the maximum tensile

TABLE 1—*Baseline hip stem segments used for fractography.*

Specimen	Load lb (N)	Cycles to Failure
PR-2003-025-5	1050 (4671)	10 000 000 (Run-out)
PR-2003-025-2	1200 (5338)	5 860 924
PR-2003-025-4	1500 (6672)	1 104 678
PR-2003-025-1	1800 (8007)	145 038

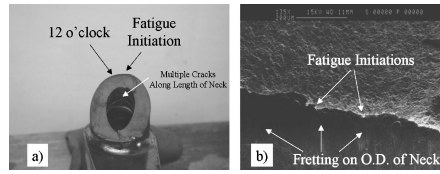

FIG. 6—*Optical (a), and SEM micrograph (b) of baseline Sample PR-2003-025-2 showing fretting fatigue initiations on outside diameter adjacent to 12 o'clock position.*

stress to occur. Fatigue cracks initiated on the outer diameter of the taper, near the 12 o'clock position. Multiple cracks in the hoop-radial plane are present at several positions along the length of the taper.

The micrograph in Fig. 6(*b*) shows a magnified view of the failure. At higher magnification, it is apparent that the fatigue cracks initiated from fretting damage on the outside diameter. Fretting damage resulted from relative motion between the tapered hip stem and the surrounding metaphyseal.

Specimens PR-2003-025-4 and PR-2003-025-1 failed at a similar location as PR-2003-025-2, near 12 o'clock on the outside diameter. Both specimens failed from fretting damage that occurred on the outside diameter of the neck. Both specimens contained multiple fatigue cracks at various positions along the neck length.

Figure 7 shows a photograph of the metaphyseal from baseline Specimen PR-2003-025-5. The specimen was tested with a 1050 lb (4671 N) load for 10^7 cycles. While the neck taper did not catastrophically fail under this testing regime, further analysis revealed cracking in the metaphyseal.

Finite Element Modeling

Applied stress predictions from the FE model are shown in Figs. 8(*a*) and 8(*b*). Stresses are shown in the longitudinal direction relative to the neck taper axis, on both the outside diameter, and through the cross section of the taper region. Stresses are shown for an applied load of +1050 lb (4671 N), which is the fatigue strength for the baseline condition. Peak tensile stresses on the order of +65 ksi (+448 MPa) are predicted on the outside diameter. The maximum applied stress is proximate to the 12 o'clock position due to the offset loading condition.

Figures 9(*a*) and 9(*b*) show the residual stresses from LPB placed in the FE model on the outside diameter and through the cross section of the taper, respectively. No residual tension is predicted at the surface of the taper region adjacent to the LPB processing. The LPB processed neck material pushes against the surrounding material resulting in compression in adjacent unprocessed areas. Subsurface compensatory tensile stresses on the order of +30 ksi (+207 MPa) or less were predicted below the compression from LPB. Tension on the inside diameter bore increased +10 to +15 ksi (+69 to +103 MPa) as a result of introducing compression on the outside diameter.

Figure 10 shows the longitudinal applied stresses at 12 o'clock for both a 1050 and 1800 lb (4671 and

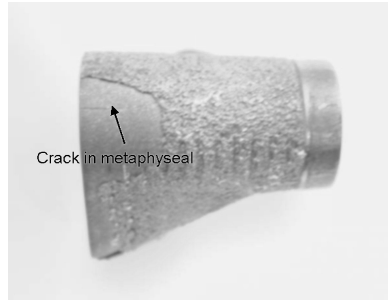

FIG. 7—*Optical photograph of metaphyseal used in conjunction with the testing of sample PR-2003-025-5. Note the cracking in the metaphyseal that occurred before complete failure of the construct.*

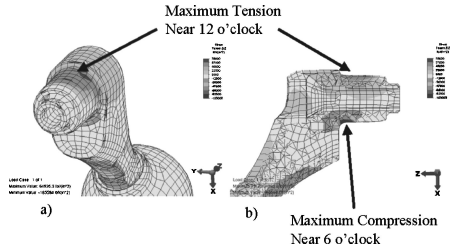

FIG. 8—*Finite element model showing the predicted applied stress resulting from a 1050 lb (4671 N) load on the outside diameter (a), and through the cross section (b) of the neck segment taper.*

8007 N) load. Surface residual compressive stress measured by XRD on an LPB processed neck segment was added to the applied stress distributions to provide an estimate of the combined stress state. A horizontal line representing the fatigue strength of solution treated and aged (STA) Ti-6Al-4V [32] at 10^7 cycles, R=0 and Kt=1, is shown for comparison. Results indicate a maximum combined stress of close to +35 ksi (+241 MPa) on the outside diameter at the start of the radius for the 1800 lb (8007 N) load. Combined stresses for the 1050 lb (4671 N) load was compressive throughout the taper region and less than half the fatigue strength of the 1800 lb (8007 N) load. Results suggest that the neck stem should not fail in HCF in the LPB processed regions for loads up to at least 1800 lb (8007 N).

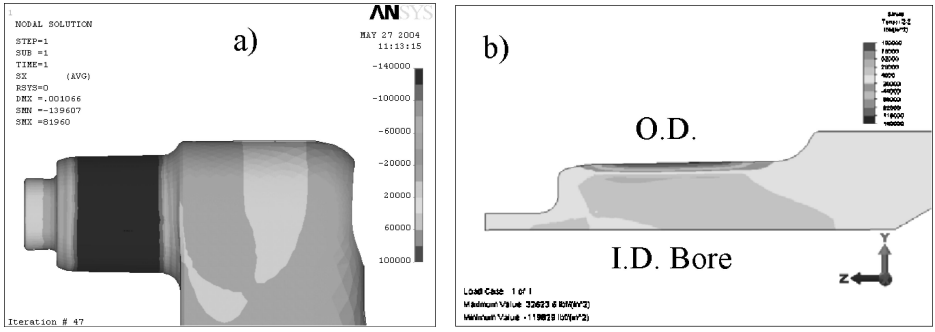

FIG. 9—*Compressive residual stresses imparted into femoral hip segment FE model. Residual stresses are shown on outside diameter (a), and through the cross section (b).*

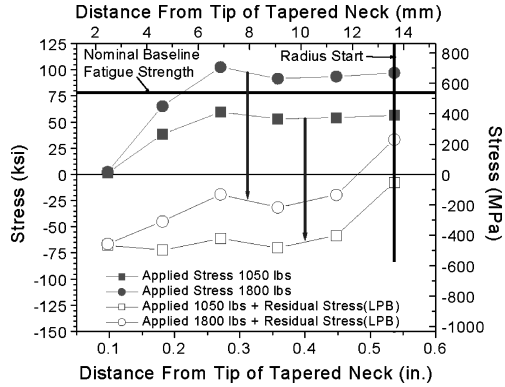

FIG. 10—*Applied and combined (applied + residual stress) on outside diameter of neck stem taper.*

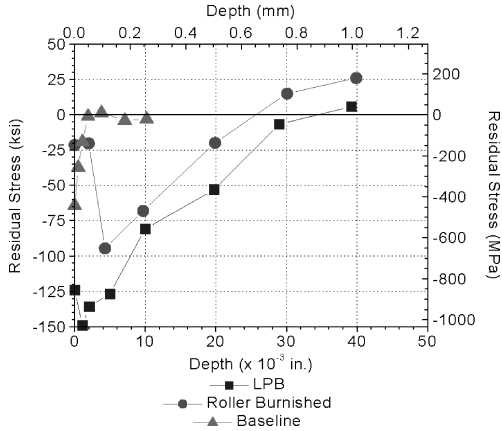

FIG. 11—*XRD residual stress versus depth profiles on the outside diameter of the tapered neck showing deeper and higher compression for LPB processed specimen.*

Residual Stress Measurements

The residual stress distributions measured by XRD on the outside diameter of a baseline, roller burnished and low plasticity burnished hip segment are shown in Fig. 11. A relatively shallow layer of compression exists on the hip stem in the baseline condition from the turning operation. Roller burnishing produced a depth of compression on the order of 0.02 in. (0.51 mm) with relatively low surface compression. LPB produced slightly greater than 0.03 in. (0.76 mm) depth of compression with near surface compression on the order of five times that produced by roller burnishing.

XRD residual stresses measured at mid-length of the inside diameter bore of the taper for the as-received, roller burnished, and low plasticity burnished specimens were all compressive. All three samples had similar compression. As predicted by the FE model, the compensatory tension on the inside diameter bore was negligible, and produced essentially no change to the residual stresses.

XRD residual stress results collected at the 6 o'clock position, adjacent to the radius, are shown in Fig. 12. The applied compressive stresses from fatigue testing are not altering the compressive residual stresses significantly or causing a residual stress inversion from compression to tension.

Fatigue Testing

Results for the HCF fatigue tests are presented graphically in Fig. 13. The data are shown in a semi-log plot of maximum force vs. cycles to failure. Arrows indicate run-outs for both baseline and low plasticity burnished samples. Multiple run-outs were achieved for both sets of samples.

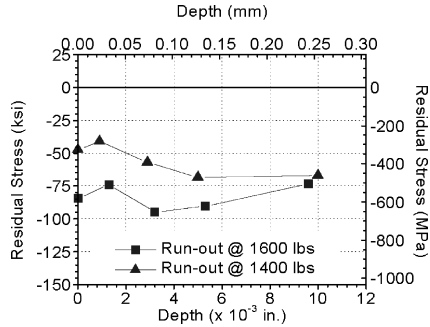

FIG. 12—*Residual stress versus depth showing compression remaining on the compressively loaded side of the neck taper.*

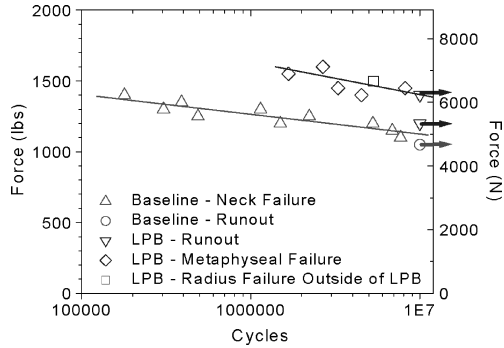

FIG. 13—*HCF results indicating LPB produces a nominal 40 % increase in fatigue strength at 10^7 cycles. Arrows indicate run-outs at 10^7 cycles.*

Baseline specimens were tested within a load range of 1050 to 1400 lb (4671 to 6228 N). All fatigue failures in the baseline specimens occurred in the tapered neck region of the hip segment. Baseline results, shown in red symbols, indicate a fatigue strength at 10^7 cycles of 1050 lb (4671 N).

Low plasticity burnished neck segments were tested at loads of 1400 to 1600 lb (6228 to 7117 N). LPB improved the fatigue strength of the hip stem greater than 40 % and increased the life by over 10 × as depicted by the blue symbols. The metaphyseal fractured on five of the LPB processed specimens ultimately ending the test. No failures initiated in the fretted LPB processed neck taper region. However, one failure occurred at 1500 lb (6672 N) from fretting damage in the non-low plasticity burnished radius. Further refinement of the LPB process is planned to include coverage of the radius, further strengthening the THP.

Additional HCF tests conducted on production neck segments confirm the fatigue strength of the neck segment to be at least 1400 lb (6228 N). Future HCF tests are planned using larger metaphyseals to gage the true fatigue strength of the low plasticity burnished neck segment.

Conclusions

- LPB produced compressive residual stress in the stem neck segment to a depth of 0.03 in. (0.762 mm) with maximum compression approaching −150 ksi (−1034 MPa) near the surface. LPB produced a deeper layer of compression compared to roller burnishing with nominally 5× the compressive magnitude near the surface.
- LPB completely eliminated fretting failures in the processed neck stem region.
- LPB increased the fatigue strength of the THP by 40 % above the baseline condition and increased the life by 10×. Fatigue cracks initiated in the metaphyseal in several of the LPB fatigue tests indicating the hip segment has a fatigue strength higher than 1400 lb (6228 N). Further tests are being planned, with larger metaphyseals, to better determine the fatigue strength of the neck taper.
- Fractographic observations indicate that the prevalent location of failure initiation for baseline samples is approximately 30° to the clockwise of the 12 o'clock position (see figures for orientation). This trend in failure initiation location indicates that this position experiences high applied stress during loading as indicated from the finite element model. The baseline specimens generally have multiple initiations along the length of the taper which appear to be directly related to fretting damage occurring on the surface of the taper in the same general area.

Acknowledgments

The authors gratefully acknowledge Brian Tent, Doug Young, Chris Wahl, and Tom Lachtrupp, from Lambda Technologies, for the fractography, finite element modeling, CNC code development, LPB design, and residual stress measurement, and Robert Neugebauer and the staff at Martest Inc. for the HCF testing.

References

[1] Frost, N. E., Marsh, K. J., and Pook, L. P., *Metal Fatigue*, Oxford University Press, 1974.

[2] Fuchs, H. O. and Stephens, R. I., *Metal Fatigue in Engineering*, John Wiley & Sons, 1980.

[3] Berns, H. and Weber, L., "Influence of Residual Stresses on Crack Growth," *Impact Surface Treatment*, S. A. Meguid, Ed., Elsevier, 1984, pp. 33–44.

[4] Ferreira, J. A. M., Boorrego, L. F. P., and Costa, J. D. M., "Effects of Surface Treatments on the Fatigue of Notched Bend Specimens," *Fatigue and Fracture Engineering Materials and Structures*, Vol. 19, No. 1, 1996, pp 111–117.

[5] Prevéy, P. S., Telesman, J., Gabb, T., and Kantzos, P., "FOD Resistance and Fatigue Crack Arrest in Low Plasticity Burnished IN718," *Proceedings of the 5th National HCF Conference*, Chandler, AZ, March 7–9, 2000.

[6] U.S. Patents 5,826,453 (Oct. 1998), 6,415,486 B1 (July 2002) other U.S. and foreign patents pending.

[7] "Low Plasticity Burnishing," NASA Tech Briefs, Aug. 2002, p. 50.

[8] B. Hogan, "Longer Life with Low Plasticity Burnishing," *ASME J. Manuf. Sci. Eng.*, Dec. 2001, pp. 34–38.

[9] Gabb, T., Telesman, J., Kantzos, P., and Prevéy, P., "Surface Enhancement of Metallic Materials," Advanced Materials & Processes, ASM,P. Hunt, Ed., Jan. 2002, pp. 69–72.

[10] Prevéy, P., Jayaraman, N., and Ravindranath, R., "Effect of Surface Treatments on HCF Performance and FOD Tolerance of a Ti-6Al-4V Vane," *Proceedings, 8th National Turbine Engine HCF Conference*, Monterey, CA, April 14–16, 2003.

[11] Prevéy, P. S., Hornbach, D., Jacobs, T., and Ravindranath, R., "Improved Damage Tolerance in Titanium Alloy Fan Blades with Low Plasticity Burnishing," *Proceedings of the ASM IFHTSE Conference*, Columbus, OH, Oct. 7–10, 2002.

[12] Prevéy, P. S. et al., "The Effect of Low Plasticity Burnishing (LPB) on the HCF Performance and FOD Resistance of Ti-6Al-4V," *Proceedings 6th National Turbine Engine HCF Conference*, Jacksonville, FL, March 5–8, 2001.

[13] Shepard, M., Prevéy, P., and Jayaraman, N., "Effect of Surface Treatments on Fretting Fatigue Performance of Ti-6Al-4V," *Proceedings, 8th National Turbine Engine HCF Conference*, Monterey, CA, April 14–16, 2003.

[14] Prevéy, P. S. and Cammett, J. T., "Restoring Fatigue Performance of Corrosion Damaged AA7075-T6 and Fretting in 4340 Steel with Low Plasticity Burnishing," *Proceedings, 6th Joint FAA/DoD/NASA Aging Aircraft Conference*, San Francisco, CA, Sept. 16–19, 2002.

[15] Jayaraman, N., Prevéy, P. S., and Mahoney, M., "Fatigue Life Improvement of an Aluminum Alloy FSW with Low Plasticity Burnishing," *Proceedings, 132nd TMS Annual Meeting*, San Francisco, CA, Mar. 2–6, 2003.

[16] Prevéy, P. S. and Cammett, J. T., "The Influence of Surface Enhancement by Low Plasticity Burnishing on the Corrosion Fatigue Performance of AA7075-T6," *Proceedings, 5th International Aircraft Corrosion Workshop*, Solomons, MD, Aug. 20–23, 2002.

[17] Cammett, J. T. and Prevéy, P. S., "Fatigue Strength Restoration in Corrosion Pitted 4340 Alloy Steel Via Low Plasticity Burnishing," Retrieved Sept. 2, 2003 from http://www.lambda-research.com/publica.htm.

[18] Prevéy, P. S., "Low Cost Corrosion Damage Mitigation and Improved Fatigue Performance of Low Plasticity Burnished 7075-T6," *Proceedings of the 4th Internatioanl Aircraft Corrosion Workshop*, Solomons, MD, Aug. 22–25, 2000.

[19] Prevéy, P., "The Effect of Cold Work on the Thermal Stability of Residual Compression in Surface Enhanced IN718," *Proceedings 20th ASM Materials Solutions Conference*, St. Louis, MO, Oct. 10–12, 2000.

[20] Prevey, P. S. and Jayaraman, N., "A Design Methodology to Take Credit for Residual Stresses in Fatigue Limited Designs," *Journal of ASTM International*, Vol. 2, No. 8, 2005.

[21] *Alloy Digest*, Filing Code Ti-66, July 1972, Engineering Alloys Digest, Inc.

[22] Hilley, M. E., Ed., *Residual Stress Measurement by X-Ray Diffraction*, Society of Auto. Eng., Warrendale, PA, 1971.

[23] Noyan, I. C. and Cohen, J. B., *Residual Stress Measurement by Diffraction and Interpretation*, Springer-Verlag, New York, NY1987.
[24] Cullity, B. D., *Elements of X-ray Diffraction*, 2nd ed., Addison-Wesley,Reading, MA, 1978, pp. 447–476.
[25] Prevéy, P. S., "X-Ray Diffraction Residual Stress Techniques," *Metals Handbook*, Vol. 10, , ASM, Metals Park, OH,1986, pp. 380–392.
[26] Koistinen, D. P. and Marburger, R. E., *Transactions of the ASME*, Vol. 67.
[27] Moore, M. G. and Evans, W. P., "Mathematical Correction for Stress in Removed Layers in X-Ray Diffraction Residual Stress Analysis," *SAE Trans.*, Vol. 66, pp. 340–345.
[28] Prevéy, P. S., "A Method of Determining Elastic Properties of Alloys in Selected Crystallographic Directions for X-Ray Diffraction Residual Stress Measurement," *Advances in X-Ray Analysis*, Vol. 20, Plenum Press, New York, NY, 1977, pp. 345–354.
[29] "The Effect of Prior Cold Working on the Development of Tensile Residual Stresses Following Bulk Deformation," Lambda Research - Diffraction Notes 28, Winter 2002.
[30] "Determination of Endurance Properties of Stemmed Femoral Components with the Application of Torsion," ISO 7206-4; Geneva, Switzerland; 2002.
[31] "Endurance Performance of Stemmed Femoral Components with Application of Torsion," ISO 7206-8; Geneva, Switzerland; 1995.
[32] *Aerospace Structural Metals Handbook*, Book #4, Pg. 5, 1997 edition.

Journal of ASTM International, Vol. 3, No. 5
Paper ID JAI100504
Available online at www.astm.org

Michael D. Roach,[1] *R. Scott Williamson,*[1] *and Lyle D. Zardiackas*[1]

Comparison of the Corrosion Fatigue Characteristics of 23Mn-21Cr-1Mo Low Nickel, 22Cr-13Ni-5Mn, and 18Cr-14Ni-2.5Mo Stainless Steels

ABSTRACT: The purpose of this study was to evaluate and compare the notched corrosion fatigue (CF) characteristics of a series of stainless steel alloys including 18Cr-14Ni-2.5Mo (ASTM F 138), 22Cr-13Ni-5Mn (ASTM F 1314), and 23Mn-21Cr-1Mo low nickel stainless steel (ASTM F 2229). Evaluation of alloy composition, microstructure, static single cycle mechanical properties, stress corrosion cracking, and smooth sample corrosion fatigue was performed on the same lots of each material in a previous study in our laboratories. Notched CF tensile samples of each alloy were machined using low stress grind techniques to a 2.5 mm notch root diameter (K_t=3.2) and tested at 1 Hz according to ASTM F 1801 in Ringer's solution at 37°C. A minimum of three samples was tested at five tension-tension sinusoidal load levels including a run-out level at 10^6 cycles. SEM analysis was performed on the fractured surfaces of representative samples of each alloy to characterize and compare the failure mechanisms. Previous evaluation of corrosion fatigue on smooth samples of these alloys found no significant differences in the fracture modes or cycles to failure between the samples run in distilled deionized water and those run in Ringer's solution indicating corrosion fatigue mechanisms were not in effect. However, a significant lowering of fatigue strength was observed for the notched samples of each alloy compared to the smooth samples previously tested. This suggests that even though the notch sensitivity of these alloys under static single cycle conditions has been shown to be acceptable, a notch under dynamic fatigue mechanisms may cause a substantial reduction in strength and implant life. Despite this reduction in fatigue strength, in high strength applications where the implant must be bent during surgery or may be scratched during implantation BioDur 108 proved to be the best alternative. For lower strength applications, 316LS revealed the least fatigue notch sensitivity of any of the alloys tested.

KEYWORDS: stainless steel, corrosion fatigue, notch

Introduction

Austenitic stainless steels remain a widely used metallic implant material primarily because of their high strength, good corrosion resistance, and cost effectiveness for fracture fixation devices. Significant amounts of nickel are often added to these steels to stabilize the austenitic microstructure. Although less than 5 % of the patient population have experienced metal sensitivity reactions due to implants, nickel does account for approximately 90 % of the clinically observed sensitivity reactions of metals [1]. In part as a response to concerns over such sensitivity reactions, several low nickel stainless steels have been developed. One such alloy, BioDur™ 108 from Carpenter Specialty Alloys, contains very low nickel (<0.05 %) and uses a high nitrogen content (>0.90 %) to stabilize its austenitic microstructure. This high nitrogen content has also been shown to strengthen the alloy as well as contribute to its corrosion resistance [2–4].

Under single cycle loading conditions, implant grade austenitic stainless steels have demonstrated good mechanical properties in both smooth and notched configurations. In vivo, however, implants are subjected to discontinuous cyclic loading often over a period of many years. The fatigue fracture of these implants is not a function of time but rather stress and number of cycles, so the behavior of these alloys under low and high cycle fatigue loading conditions is also of primary concern. Since the actions of muscles and body weight are the two main forces applied *in vivo*, the load amplitude ranges in these cyclic

Manuscript received February 22, 2006; accepted for publication February 22, 2006; published online March 2006. Presented at ASTM Symposium on Fatigue and Fracture of Medical Metallic Materials and Devices on 7–11 November 2005 in Dallas, TX; M. R Mitchell and K. L. Jerina, Guest Editors.

[1] Senior Materials Engineer, Senior Materials Engineer, Chair, Department of Biomedical Materials Science, and Professor of Orthopaedic Surgery, University of Mississippi Medical Center, Jackson, MS 39216.

laboratory tests should remain relatively small [5]. ASTM F 1801 governs the testing of metallic implant materials under axial fatigue conditions and suggests a stress amplitude ratio, R, of 0.053 and testing at 1 Hz to best simulate physiological conditions. Fatigue fracture has been shown to be highly dependent on the alloy microstructure and up to 90 % of an alloys fatigue life may be consumed in the crack initiation stage [6]. The presence of a surface defect or notch in a material may lead to an increased state of stress that may accelerate the initiation of a fatigue crack. For this reason, it is also of interest to test notched fatigue samples. A previous study using four-point bending fatigue showed that unlike titanium, the fatigue life of stainless steel spinal rods was not shortened by an applied French bender notch or top loading connector notch in the material [7]. Based on these results this study recommended that when spinal rods must be bent and fatigue life is a concern, stainless steel systems should be considered.

Of all the available fracture modes, fatigue is one of the most sensitive to its environment. The human body can be a harsh environment. Many factors, including the fluctuating ionic concentration in the saline environment, the body loading mechanisms discussed earlier, initial fluctuations in pH following implantation, and a number of potential tissue reactions can greatly influence the performance of an implant [8]. The addition of these potentially corrosive environmental effects to the previously mentioned fatigue loading mechanisms also warrants the testing of these alloys under corrosion fatigue conditions. Several previous corrosion fatigue studies on austenitic stainless steel smooth samples [9–12], including previous work in our laboratories [13], have shown reduced fatigue resistance and enhanced fatigue crack growth rates when these materials were exposed to NaCl environments, as compared to air or water.

Even though the notched fatigue and smooth corrosion fatigue characteristics of austenitic stainless steel implant materials in physiological solutions are well documented, very little information is available in the literature on the notched sample corrosion fatigue of these materials. Therefore, this study examined the notched corrosion fatigue characteristics on the same stainless steel alloys as our previous smooth corrosion fatigue study [13]. The same lots of the three austenitic stainless steels were used to manufacture notched samples in order to eliminate any material property variations due to changing lots. Any enhanced effects on the fatigue characteristics due to the increased state of stress on the notched samples as compared to the smooth samples were noted and discussed.

Materials and Methods

The low nickel stainless steel chosen for the study was alloy A (ASTM F 2229). Alloy B, 316LS (ASTM F 138), and alloy C, 22Cr-13Ni-5Mn (ASTM F 1314), were chosen for comparison since they were available from the same source and represented the other two commonly used austenitic stainless steel alloys. Alloys were supplied as 8-mm diameter centerless ground bar in the cold worked condition. In order to verify information supplied on primary certification documents and to establish baseline mechanical properties for fatigue testing, each alloy was characterized for composition, microstructure, and tensile properties. Quantitative compositional evaluation of the major alloying elements of each alloy was determined using an inductively coupled plasma spectrometer (ICP) with a spark attachment for analysis of solid samples (SPECTRO[2] ICP with LISA). The microstructure of these alloys was evaluated at 100× magnification according to ASTM E 112 with all samples prepared in duplicate.

To establish baseline data for fatigue testing, smooth and notched mechanical testing was performed on each alloy using an MTS[3] servo hydraulic test system. Five smooth and five notched tensile samples of each alloy were machined using low stress grinding to a maximum surface roughness of 16 microinches (Ra $\leqslant$ 16) in the gage. Smooth samples were prepared with a 36-mm gage length and a 6-mm gage diameter. Testing was performed at a 0.3 mm/min stroke rate to yield, and a 3.0 mm/min stoke rate from yield to failure. Strain was measured using a 25 mm extensometer. The ultimate tensile strength (UTS), 0.2 % yield strength (YS), elastic modulus (MOD), percentage elongation (%El.) to fracture, and reduction of area (%ROA) were calculated. Notched tensile samples were prepared with a K_t factor of 3.2 and a notch root diameter of 6 mm. For many years, the ratio of the notch tensile strength to the smooth tensile strength was considered the most valid method for evaluating the sensitivity to a notch and the toughness of a material. As specified in the ASTM Test Method for Sharp-Notch Tension Testing with Cylindrical Specimens (E 602), it is widely recognized that since the onset of plastic deformation occurs at the yield strength, the ratio of the notch tensile strength to the smooth 0.2 % yield strength may be a more useful

[2]SPECTRO Analytical Instruments, Fitchburg, MA.
[3]MTS, Eden Prarie, MN.

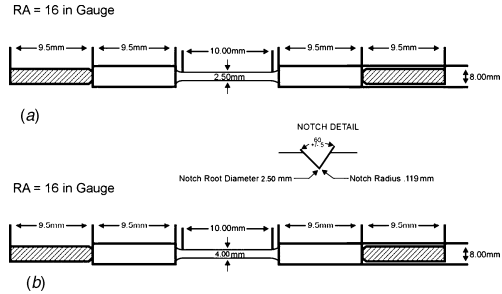

FIG. 1—*(a) Sample drawing for smooth fatigue samples. (b) Sample drawing for notched fatigue samples.*

predictor of toughness. Notch tensile testing was performed according to ASTM E 602 such that the load rate did not exceed the limit of 690 MPa/min. The notch tensile strength (NTS), the ratio of NTS to UTS, and the ratio of NTS to 0.2 % YS were determined.

Corrosion fatigue testing was performed in tension-tension on smooth samples of each alloy in both aerated distilled/deionized water (DI water) and aerated Ringer's solution at 37°C. Fatigue testing followed the guidelines of ASTM F 1801 using the given R (Φ_{min}/Φ_{max}) value of 0.053. Smooth fatigue samples were prepared using the same low stress grind techniques as the smooth tensile samples previously described with a 10-mm gage length and a 2.5-mm gage diameter (Fig. 1(*a*)). Corrosion fatigue was also performed on notch samples of each alloy in Ringer's solution at 37EC. Notch fatigue samples were prepared with a K_t factor of 3.2 and a 2.5-mm diameter at the root of the notch (Fig. 1(*b*)). Samples were mounted vertically to facilitate complete submersion of the sample through the gage section, and all fixturing in contact with the solution was either teflon or the same alloy as the samples to eliminate any corrosion couples. A tension-tension load was applied as a sinusoidal wave function in load control at 1 Hz. Triplicate samples were tested at each of five stress levels to failure or to a fatigue run-out limit of 10^6 cycles. Data were plotted as stress versus number of cycles to fracture to generate typical S/N curves for each alloy. Fatigue notch factors (K_f) and fatigue notch sensitivities (q) were computed from the S/N curves for each alloy.

$$K_f = \frac{\sigma_{smooth(unnotched)}}{\sigma_{notch}} \tag{1}$$

$$q = \frac{K_f - 1}{K_t - 1} \tag{2}$$

The fatigue notch factor (K_f) shown in Eq. 1 is the ratio of the fatigue strength of a smooth sample to the fatigue strength of a notched sample at the same number of stress cycles. Since this value will vary according to the position on the S-N curve, it was calculated for high stress (10 k cycle) and low stress run-out limit (1 M cycle) levels for each alloy. In addition, the fatigue notch sensitivity (q) shown in Eq. 2 was calculated for both high and low stress levels. After the completion of fatigue testing, analysis of the fracture surfaces from at least one fatigue sample of each alloy which fractured at less than 10^5 cycles in low cycle fatigue (LCF) and one sample that fractured at greater than 10^5 cycles were examined by scanning electron microscopy (SEM). Comparison was made between alloys to determine the area of crack initiation (Stage I fatigue), fracture morphology during crack propagation (Stage II fatigue), and the final fracture mode (Stage III fatigue). Additionally, comparison was made to identify any differences in fracture surface morphology between fatigue in distilled/deionized water and Ringer's solution for each alloy. Finally, comparisons were made between the fracture morphologies of the smooth and notched samples of each alloy.

Results and Discussion

Compositional and metallurgical analysis results for these stainless steel alloys were previously performed in our laboratories and results are reported elsewhere [14]. A summary of the smooth and notched mechanical testing results, previously performed in our laboratories, is provided in Table 1 and establishes a baseline for the fatigue analysis [15]. NTS/UTS ratios ranged from 1.4–1.7 indicating none of these alloys is considered notch sensitive under single cycle conditions.

Smooth fatigue S/N curves for these alloys were also previously generated in our laboratories and reported, but will be repeated here for comparative purposes [13]. Since no statistically significant differences were shown in any of the alloy systems between the S/N curves for Ringer's solution and DI water in the smooth samples, the notched samples were only tested in the more aggressive Ringer's solution. Table 2 provides a summary of the fatigue notch factors, K_f, and fatigue notch sensitivities, q, calculated for each alloy. The K_f value controls the crack initiation time for the material [16]. Figures 2(*a*)–2(*c*), provide a comparison of the smooth S/N curve to the notched S/N curve for each alloy tested.

The low-Ni nitrogen strengthened stainless steel notched samples revealed a substantially suppressed S/N curve with a run-out strength in Ringer's solution of 300 MPa compared to 550 MPa for the smooth samples (Fig. 2(*a*)). This large reduction in fatigue strength due to the presence of even a small notch, or defect, has been shown by others for higher strength steels [17]. Normally, materials become more notch sensitive resulting in fatigue notch sensitivity values (q) at higher cycle counts and lower stresses. However, the calculated q values for alloy A ranged from 0.41 on the high stress samples to 0.38 on the low stress samples (Table 2). These values indicate the material was slightly less notch sensitive at higher cycle counts. Alloy A is known to cold work very rapidly [2,3,13] and the K_f and q values are functions of the time (or cycles) required to initiate a fatigue crack. Therefore, the higher notch sensitivity at the high stress end of the curve was attributed to the extensive cold working caused by the higher applied stress. As suggested previously in the fatigue work on the smooth samples of this alloy [13], this rapid cold working could lead to the pinning of nitrogen interstitials in the FCC lattice. These pinned interstitials would create some areas of localized high intensity stress fields near the surface of the sample making it more notch sensitive to the higher applied loads.

For alloy A LCF samples, SEM analysis revealed primarily a cleavage mechanism in the crack initiation region (Fig. 3(*a*)). At higher magnifications, this region showed multiple cleavage terraces with fluting on the edges as well as some furrowing (Fig. 3(*b*)). Early in the crack propagation stage, the mechanism changed to a mixed-mode quasi-cleavage fracture containing cleavage facets with feather marks, extensive secondary cracking, and areas of more typical striated ductile fatigue crack propagation (Fig. 3(*c*)). As the fatigue crack continued to progress across the sample the mechanism changed almost exclusively to coarsely spaced fatigue striations (Fig. 3(*d*)) and continued until ductile overload failure via microvoid coalescence. This change during Stage II fatigue from a quasi-cleavage to a fatigue striation mechanism represents a change in the stress intensity of the material. Previous studies have shown the

TABLE 1—*Smooth and notched mechanical testing results.*

Alloy	UTS[a] (MPa)	0.2 % Offset Yield Strength (MPa)	NTS[b] K_t=3.2 (MPa)	NTS/0.2 % Yield Strength Ratio	NTS/UTS Ratio
A	1344	1179	2255	1.91	1.68
B	1014	793	1455	1.83	1.43
C	1351	1082	2206	2.04	1.63

[a]UTS=Ultimate Tensile Strength.
[b]NTS=Notch Tensile Strength.

TABLE 2—*Fatigue notch sensitivity results, K_t=3.2.*

Alloy	Fatigue Notch Factor, K_f High Stress (10 k cycles)	Fatigue Notch Factor, K_f Low Stress (1 M cycles)	Fatigue Notch Sensitivity, q High Stress (10 k cycles)	Fatigue Notch Sensitivity, q Low Stress (1 M cycles)
A	1.90	1.83	0.41	0.38
B	1.56	1.80	0.25	0.36
C	1.80	2.40	0.36	0.64

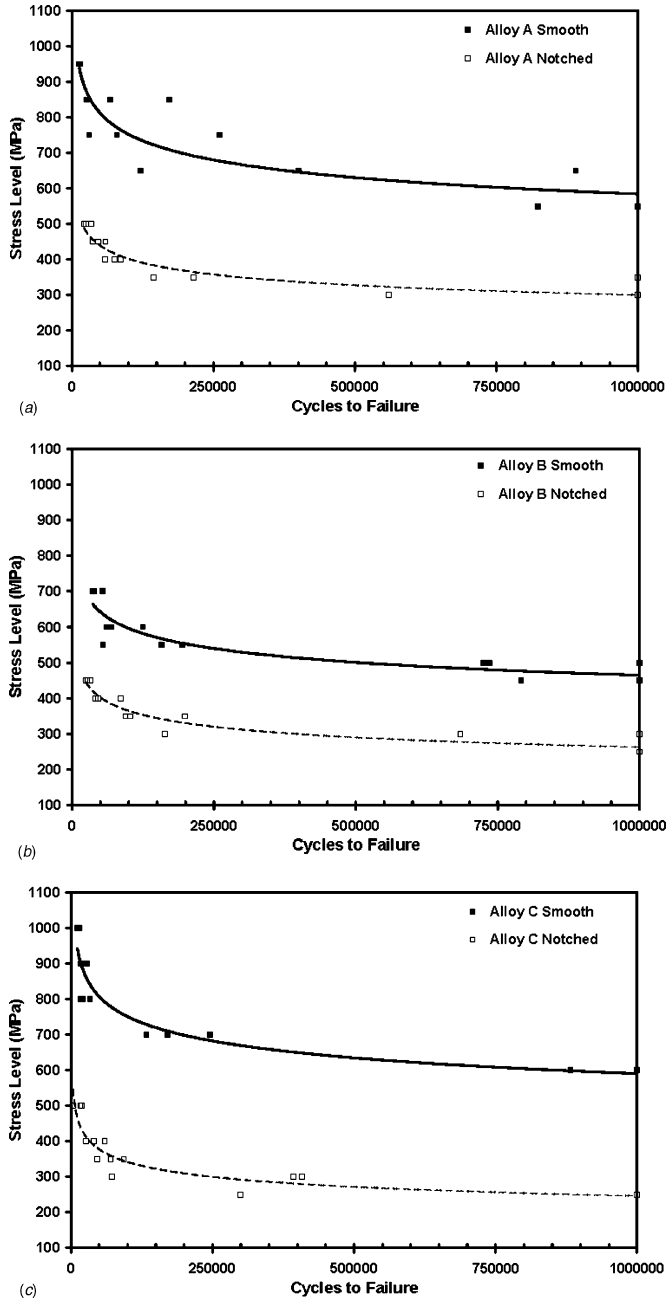

FIG. 2—*(a) Comparison of the smooth and notched sample S/N curves generated for alloy A in Ringers solution at 37°C. (b) Comparison of the smooth and notched sample S/N curves generated for alloy B in Ringers solution at 37°C. (c) Comparison of the smooth and notched sample S/N curves generated for alloy C in Ringers solution at 37°C.*

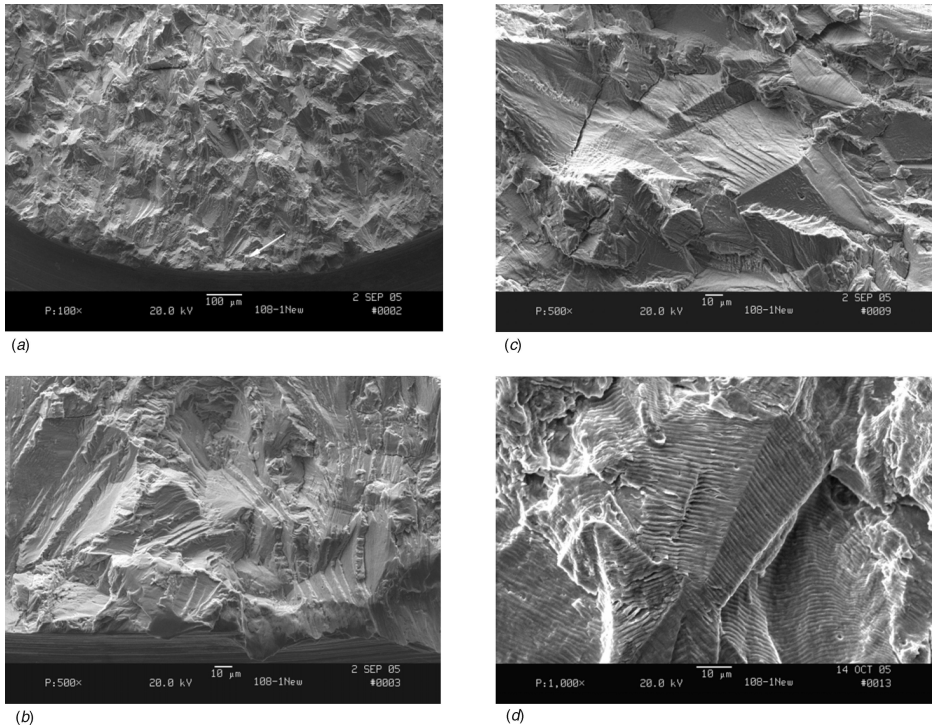

FIG. 3—*(a) Representative low cycle alloy A notched sample fatigue crack initiation region at low magnification. (b) Crack initiation region of Fig. 3(a) at a higher magnification showing multiple cleavage terraces. (c) Early crack propagation region of Fig. 3(a) showing quasi-cleavage with secondary cracking. (d) Transition to a fatigue striation mechanism later in the crack propagation region of alloy A at low cycles.*

stress intensity to govern the fracture mechanism and crack propagation time in Stage II fatigue [16,18]. The higher cycle samples overall contained a similar fractures surface to the LCF samples in the crack initiation region including areas of furrowing and cleavage terraces with fluting on the edges (Figs. 4(*a*) and 4(*b*)). The crack propagation stage consisted mostly of cleavage facets with feather markings and extensive furrowing combined with secondary cracking (Fig. 4(*c*)). Just before ductile overload the mechanism changed to a thin band of finely spaced fatigue striations (Fig. 4(*d*)).

Overall the fatigue fracture mechanisms of the notched samples of alloy A were similar to those shown previously in the smooth samples. The percentage of cleavage fracture was higher on the notch samples compared to the smooth samples as expected due the additional constraints of the tri-axial state of stress at the root of the notch. This quasi-cleavage fracture mechanism has been shown in the previous study on smooth fatigue samples [13] and in other studies on high nitrogen steels [19]. This more brittle fracture mechanism further supports the unusual notch sensitivity values described earlier. It is attributed to the rapid work hardening rate of the material pinning nitrogen interstitials in localized areas of the FCC lattice and thus impeding further plastic deformation locally and promoting the overall mixed-mode fracture mechanism. The mechanisms and morphological structures associated with this quasi-cleavage fracture have been well documented by others [18,20].

Alloy B notched samples revealed a slightly suppressed S/N curve with a notched run-out strength of 250 MPa compared to 450 MPa for the smooth fatigue samples (Fig. 2(*b*)). The calculated fatigue notch sensitivity factors for this alloy ranged from 0.25 on the high stress samples to 0.36 on the lower stress samples (Table 2). These values follow the normal trend of becoming more notch sensitive at lower

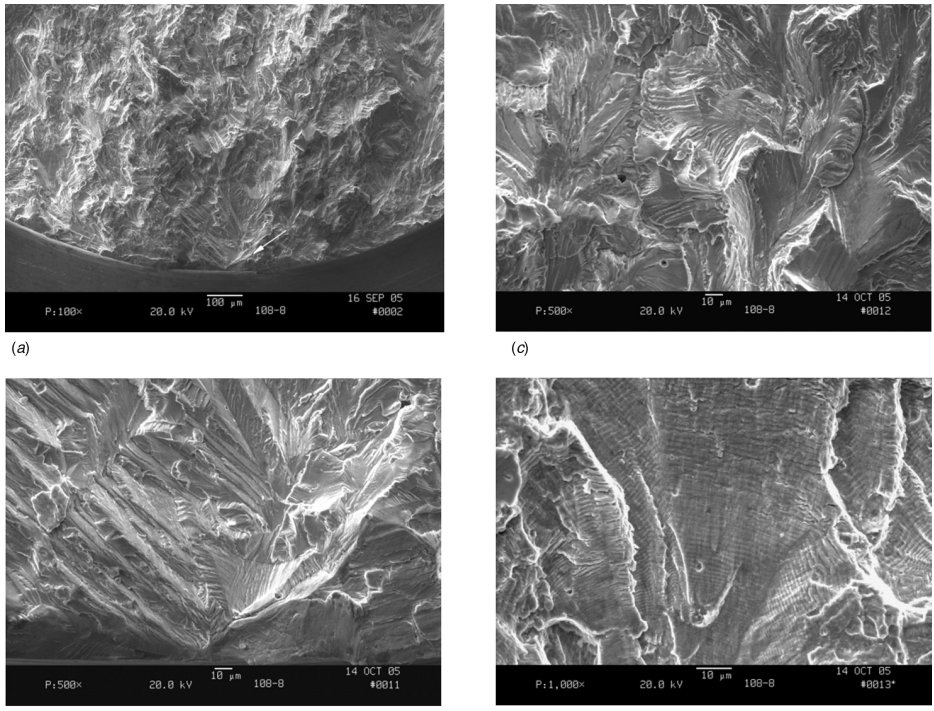

FIG. 4—*(a) Representative high cycle alloy A notched sample fatigue crack initiation region at low magnification. (b) Region of Fig. 4(a) at higher magnification showing furrowing, terracing, and fluting. (c) Early crack propagation region of Fig. 4(a) showing quasi-cleavage with secondary cracking. (d) Later crack propagation region of alloy A high cycle samples showing finely space fatigue striations.*

stresses and higher cycle counts. Since a fatigue notch sensitivity rating of 1.0 is considered fully notch sensitive, these values also indicate that alloy B was relatively insensitive to fatigue crack initiation as the result of a small notch or defect in the material. These results are in good agreement with a previous study concluding that when spinal rods must be bent or deformed by a surgeon prior to implantation and the fatigue life of the implant is a concern, consideration should be given to stainless steel over titanium alloys [7].

SEM analysis of LCF samples of alloy B revealed a rather typical fatigue crack initiation and early propagation region (Fig. 5(*a*)). Examination at higher magnification in Stage II fatigue, revealed a typical transgranular fatigue fracture with coarsely spaced fatigue striations and substantial secondary cracking (Fig. 5(*b*)). Stage III fatigue failure was due to ductile overload and consisted of ductile dimples. Higher cycle fatigue samples revealed a similar fracture mechanism with more finely spaced fatigue striations and secondary cracking in Stage II fatigue which was attributed to lower applied stresses (Figs. 6(*a*) and 6(*b*)). The fracture surfaces were similar to those in the previous work on the smooth samples of this alloy [3]. The similarity in the fracture mechanisms between the smooth and notched samples further support the low fatigue notch sensitivity factors indicating this material is relatively insensitive to a notch or defect even under cyclical loading conditions.

Alloy C stainless steel notched samples showed the largest suppression in the S/N curve with a run-out strength in Ringer's solution of 250 MPa compared to that of 600 MPa in the smooth samples (Fig. 2(*c*)). Fatigue notch factors calculated for this alloy ranged from 0.36 on low cycle samples to 0.64 on high cycle samples (Table 2). These values indicate alloy C becomes substantially more notch sensitive at higher cycle counts and lower stresses. This reduction in fatigue notch resistance is believed to be due to the work

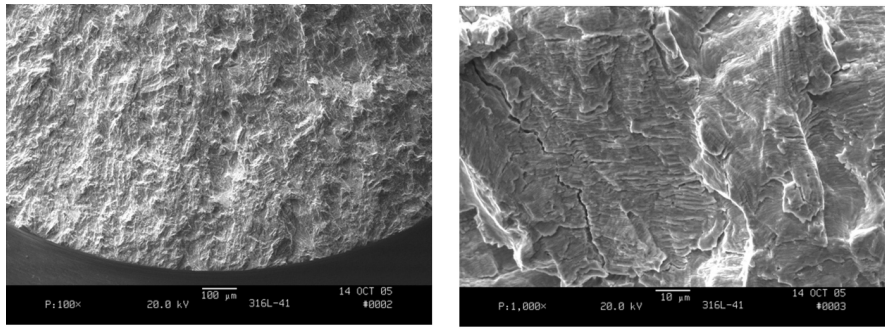

FIG. 5—*(a) Representative low cycle alloy B notched sample fatigue crack initiation region at low magnification. (b) Stage II fatigue of alloy B low cycle samples showing striations and secondary cracking.*

hardening of the material over the duration of the fatigue test. These data agree well with other studies that have shown the increase in fatigue resistance due to cold working of this alloy to drop off as cold working increases [12,21].

Low magnification SEM analysis of LCF samples of alloy C showed a fracture consisting of several radial markings indicating several crack initiation sites (Fig. 7(*a*)). These multiple crack initiation sites with only one leading to catastrophic failure is a characteristic of fatigue fractures that has been well documented [22]. These fatigue cracks continue to propagate across the fatigue surface to a relatively large area of ductile overload showing ductile dimples. At much higher magnification, Stage II fatigue shows a very finely striated fracture surface with secondary cracking increasing toward the overload region (Fig. 7(*b*)). Higher cycle fatigue samples revealed a macro fracture consisting of fewer radial markings including one that extended across the sample to the overload region (Fig. 8(*a*)). Crack propagation was similar to the LCF samples with very finely spaced striations with secondary cracking increasing toward overload (Fig. 8(*b*)). The notched fracture surfaces were similar to those shown previously on the smooth samples [13].

For comparisons between the three austenitic stainless steels, a composite chart of the notched and smooth sample S/N curves generated for each alloy tested is included in Fig. 9. The smooth samples of the two nitrogen strengthened stainless steels, alloys A and C, revealed substantially higher fatigue strengths compared to that of alloy B. The low-Ni alloy A notched fatigue curve also exhibited a higher notched fatigue strength than that of alloy B. However, the other nitrogen strengthened steel, alloy C, revealed a more negative S/N curve compared to that of alloy B. While additional samples would be needed to verify

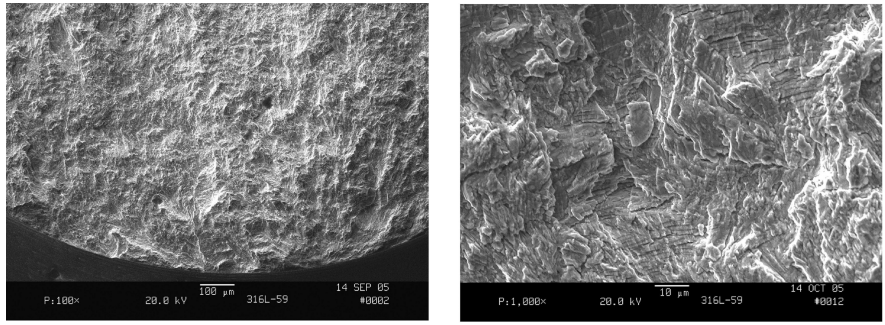

FIG. 6—*(a) Representative high cycle alloy B notched sample fatigue crack initiation region at low magnification. (b) Stage II fatigue of alloy B high cycle samples showing finely spaced striations and secondary cracking.*

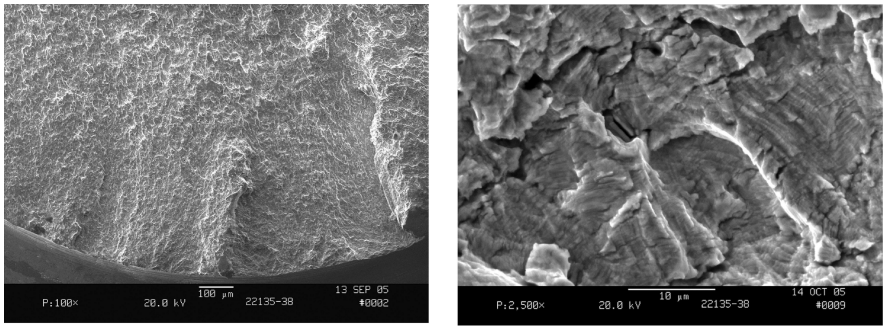

(a) (b)

FIG. 7—*(a) Representative low cycle alloy C notched sample fatigue crack initiation region at low magnification. (b) Stage II fatigue of alloy C low cycle samples showing very fine striations and secondary cracking.*

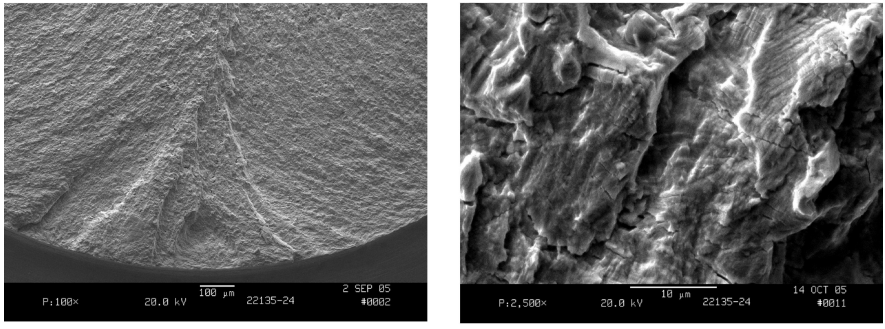

(a) (b)

FIG. 8—*(a) Representative high cycle alloy C notched sample fatigue crack initiation region art low magnification. (b) Stage II fatigue of alloy C high cycle samples showing very fine striations and secondary cracking.*

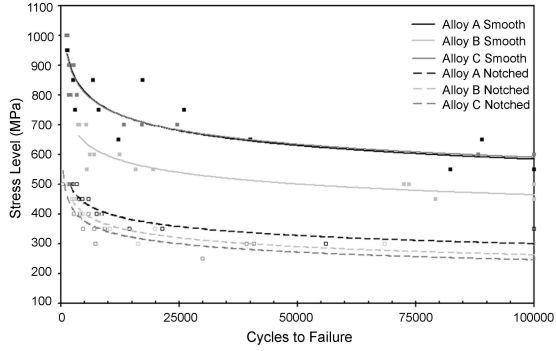

FIG. 9—*Comparison of smooth and notched S/N curves for stainless steel alloys A, B, and C.*

any statistical differences in the notched fatigue curves between alloys B and C, the trend suggests alloy C to be the most fatigue notch sensitive alloy in this study. The differences apparent between the two nitrogen strengthened alloys A and C in the notched condition are attributed to the significant ductility differences previously shown for these alloys despite the higher work hardening rate in alloy A [15].

Conclusions

Each of the three stainless steel alloys tested revealed a suppressed S/N curve for the notch samples compared to the one for the smooth samples. These results indicate that the presence of a notch or defect may substantially shorten the fatigue strength and life of an implant in the alloys tested. However, notch fatigue results suggest alloy A may be especially beneficial for high strength applications where the surgeon may have to bend the implant material or where it may be scratched during implantation. For lower strength applications, alloy B revealed the lowest fatigue notch sensitivity values indicating it was the least sensitive material tested to the presence of a notch or defect.

Acknowledgment

This research was supported by the University of Mississippi Medical Center.

References

[1] Hierholzer, S. and Hierholzer, G., *Internal Fixation and Metal Allergie*, Thieme Medical Publishers, 1992.

[2] Disegi, J. A. and Eschbach, L., "Stainless Steel in Bone Surgery," *Injury*, Vol. 31, No. 4, 2000, pp. D2–D6.

[3] Carpenter Technology Corporation Alloy Data, BioDur®108 Alloy, Carpenter Technology Corp., Reading, PA, 2000.

[4] Gebeau, R. C. and Brown, R. S., "Tech Spotlight—Biomedical Implant Alloy," *Advanced Materials and Processes*, Vol. 159, No. 9, 2001, pp. 46–48.

[5] Bratina, W. J., et al., "Fatigue Deformation and Fractographic Analysis of Surgical Implants and Implant Materials," *Conference Proceedings of the International Conference and Exhibits on Failure Analysis*, Montreal, Quebec, Canada, 1991, pp. 299–310.

[6] Buck, O., Morris, W. L., and James, M. R., "Fracture and Failure: Analyses, Mechanisms, and Applications," *Proceedings of the ASM Fracture and Failure Sessions at the 1980 Western Metal and Tool Exposition and Conference*, American Society for Metals, P. P. Tung, et al., Eds., Metals Park, OH, 1981.

[7] Dick, J. C. and Bourgeault, C. A., "Notch Sensitivity of Titanium Alloy, Commercially Pure Titanium, and Stainless Steel Spinal Implants," *Spine*, Vol. 26, No. 15, 2001, pp. 1668–1672.

[8] Dumbleton, J. H. and Edward, H. M., "Failures of Metallic Orthopaedic Implants," *Metals Handbook, 8th Ed.*, Vol. 10, American Society for Metals, H. E. Boyer, Ed., Metals Park, OH, 1975, pp. 571–580.

[9] Pohler, O., "Failures of Metallic Orthopedic Implants," *Metals Handbook, 9th Ed., Vol. 11, Failure Analysis and Prevention*, American Society of Metals, Metals Park, OH, 1985, pp. 683–688.

[10] Nakajima, M., Akatsuka, Y., and Tokaji, K., "Fatigue Crack Initiation and Growth of Stainless Steels in 3 % NACL Solution," in *Advances in Fracture Research*, Vol. 1–6, B. L. Karihaloo et al., eds. Pergamon Press, 1997, pp. 1621–1628.

[11] Nakajima, M., Shimizu, T., Kanamori, T., and Tokaji, K., "Fatigue Crack Growth Behavior of Metallic Biomaterials in a Physiological Environment," *Fatigue & Fracture of Engineering Materials & Structures*, Vol. 21, No. 1, 1998, pp. 35–45.

[12] Shetty, R. H. and Ottersburg, W. H., "Metals in Orthopedic Surgery," *Encyclopedic Handbook of Biomaterials and Bioengineering, Part B: Applications*, Marcel Dekker, Inc., D. L. Wise, et al., Eds., New York, NY, 1995, pp. 509–540.

[13] Zardiackas, L. D., Williamson, S., Roach, M., and Bogan, J. A., "Comparison of Corrosion Fatigue of BioDur 108 to 316L S. S. and 22Cr-13Ni-5Mn S. S.," *Stainless Steels for Medical and Surgical*

Applications, ASTM STP 1438, G. L. Winters and M. J. Nutt, Eds., ASTM International, West Conshohocken, PA, 2003, pp. 194–207.

[14] Zardiackas, L. D., Williamson, S., Roach, M., and Bogan, J. A., "Comparison of Anodic Polarization and Galvanic Corrosion of a Low-Nickel Stainless Steel to 316LS and 22Cr-13Ni-5Mn Stainless Steels," *Stainless Steels for Medical and Surgical Applications, ASTM STP 1438*, G. L. Winters and M. J. Nutt, Eds., ASTM International, West Conshohocken, PA, 2003, pp. 107–118.

[15] Zardiackas, L. D., Williamson, S., Roach, M., and Bogan, J. A., "Comparison of Notch Sensitivity and Stress Corrosion Cracking of a Low-Nickel Stainless Steel to 316LS and 22Cr-13Ni-5Mn Stainless Steels," *Stainless Steels for Medical and Surgical Applications, ASTM STP 1438*, G. L. Winters and M. J. Nutt, Eds., ASTM International, West Conshohocken, PA, 2003, pp. 154–167.

[16] Hedia, H. S., Barton, D. S., and Fisher, J., "Shape Optimization of a Charnley Prosthesis Based on the Fatigue Notch Factor," *Biomed. Mater. Eng.*, Vol. 6, 1996, pp. 199–217.

[17] Pilkey, W. D., "Definitions and Design Relations: Notch Sensitivity," *Peterson's Stress Concentration Factors, 2nd Ed.*, John Wiley and Sons, Inc., New York, NY, 1997.

[18] Kerlins, V. and Phillips, A., "Modes of Fracture," *ASM Handbook: Vol. 12, Fractography*, ASM International, 1999, pp. 12–71.

[19] Vogt, J. B., "Fatigue Properties of High Nitrogen Steels," *J. Mater. Process. Technol.*, Vol. 117, 2001, pp. 364–369.

[20] Brooks, C. R. and Choudhury, A., "Fracture Mechanisms and Microfractographic Features," *Metallurgical Failure Analysis*, McGraw-Hill, Inc., New York, NY, 1993, pp. 119–212.

[21] Black, J., *Orthopaedic Biomaterials in Research and Practice*, 1988.

[22] Ryder, D. A., Davies, T. J., and Brough, I., "General Practice in Failure Analysis," *Metals Handbook, 9th Ed., Vol. 11 Failure Analysis and Prevention*, American Society for Metals, Metals Park, OH, 1986, pp. 15–46.

Journal of ASTM International, Vol. 3, No. 9
Paper ID JAI100391
Available online at www.astm.org

Kelly Pike[1]

Verification of Strain Level Calculations in Nitinol Fatigue Resistance Predictions

ABSTRACT: A method to confirm FEA strain level predictions was developed for small nitinol-compressive specimens by taking micron magnitude measurements from SEM images. The technique was used to confirm predictions of an earlier report of fatigue resistance.

KEYWORDS: fatigue, nitinol, compressive, SEM, stent, FEA (Finite Element Analysis)

Introduction

The failure to obtain accurate material properties when designing medical devices will bring harsh censure when the design proves deficient. As noted by Herbert Hoover, "*The engineer simply cannot deny that he did it. If his works do not work, he is damned*." Conversely, when a design achieves success, those who recognize its performance will also study the reason for that success. The following discussion confirms a methodology to determine a material property that is partially responsible for a medical device's success.

Recent European clinical data reports a significant resistance to fatigue for a peripheral self-expanding nitinol stent [1], see Table 1. By comparison, it has been reported that other designs have a strut fracture rate 15 to 29 times greater [2].

The engineers responsible for the fatigue-resistant stent based their design on data taken from a "V"-shaped gage specimen they created to imitate a superelastic nitinol stent strut. Lin and Denison [3] asserted that the quality of the polished surface would improve fatigue fracture resistance.

Additionally, Harrison and Lin [4] claimed achieving robust fatigue resistance at a mean strain of up to 4 %. This conclusion was in contrast to reports by other investigators that had shown lower fatigue performance for nitinol materials. In light of the positive clinical performance noted above, it is reasonable to describe the device performance predicted by Lin and Harrison as possible if the disparity with other investigators can be reconciled. A review has been conducted to confirm the veracity of the 0–4.0 % strain range that was cited in the Lin-Harrison experiments.

Review of V-shape Specimen Experiment

The fatigue specimens used by Lin and Harrison were laser cut from commercially available nitinol tubing with the struts oriented along the axis of the tube. Specimen preparation included standard stent production processes: cleaning, expansion, heat treating, and polishing to produce a specimen representative of the stent strut's high stress "V" region. An example of the geometry is shown in Fig. 1. The final V section is 0.004-in. wide and the support legs are 0.008-in. wide. The exposed sections of the legs are 0.31-in. long.

TABLE 1—*Peripheral stent system results in European clinical study.*

Patients	Stents	Average Follow-up Period	Average Lesion Length	Fracture Rate Stents
125	113	15 months	125 mm	2/113 1.8 %

Manuscript received October 11, 2005; accepted for publication June 14, 2006; published online July 2006. Presented at ASTM Symposium on Fatigue and Fracture of Medical Metallic Materials and Devices on 7–11 November 2005 in Dallas, TX; M. R. Mitchell and K. L. Jerina, Guest Editors.

[1] Abbott Vascular, P.O. Box 58167, Santa Clara, CA 95054.

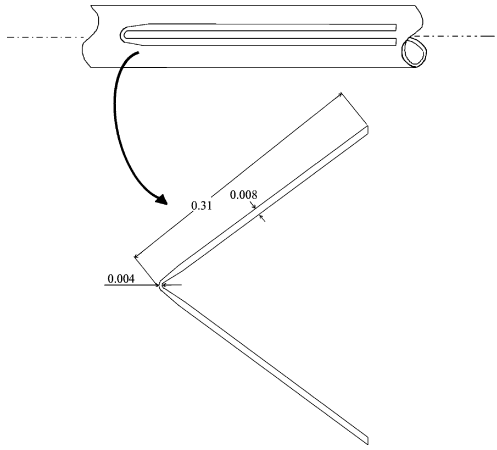

FIG. 1—*Nitinol V specimen cut from a tube and expanded (all dimensions are in inches).*

The V-shaped specimen is comparable to a stent strut as shown in Fig. 2. The major difference between the two items is the extension of the legs of the V-shaped specimen so that it can be captured in the fatigue fixture test grips.

Review of Fatigue Data

Multiple runs were performed with the V-shaped specimens at different mean and alternating strains in the studies described by Lin and Denison [3] and Harrison and Lin [4]. Strains were predicted from finite element analysis (FEA) based on average part geometry and calculated in ABAQUS. See Fig. 3 below for the results. Of particular interest were the specimens that survived 1.0E+08 cycles of alternating strain (2.35 %) at 2 % mean strain.

Flow Chart of Strain Assumptions

To confirm the accuracy of the 2 % mean strain data in Fig. 3, a review of the process employed to calculate the strain magnitude was conducted. The review shows there were four areas that could have created a significant error. They were: (1) nitinol material properties, (2) specimen measurement, (3) FEA program, and (4) fatigue fixture malfunction (see Fig. 4). Although there are many assumptions made during this entire process, two of the four main areas were identified as capable of contributing to significant error and thus were subjected to verification. They were: item (2) the dimensional measurement of the V-shaped gages, and (3) strain predicted by the FEA program. Nitinol material properties (1) were

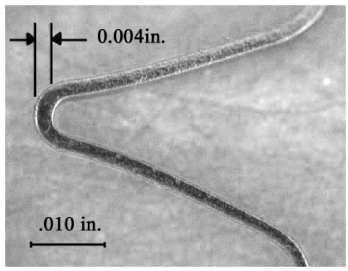

FIG. 2—*Typical nitinol stent strut with a 0.004-in. wide V.*

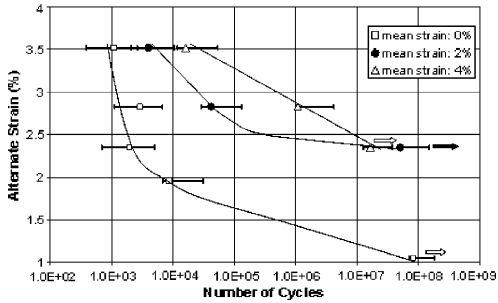

FIG. 3—*Alternating strain versus number of cycles failure for three mean strain conditions.*

not considered as a source of error because this is a published material table and confirmed when the material was received. The test equipment (4) was not considered as a source of error because it produces a direct displacement that is easily measured to a high precision.

V-shaped Specimens Geometry Verification

The specimens were designed to simulate small delicate stent strut cantilevers. As a result they are very small and present a technical challenge to measure accurately (see Fig. 5).

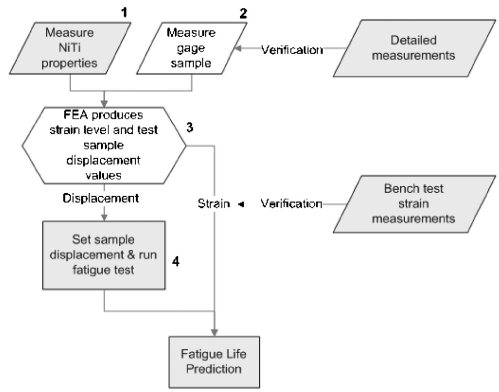

FIG. 4—*Flow chart of data collection for fatigue life prediction.*

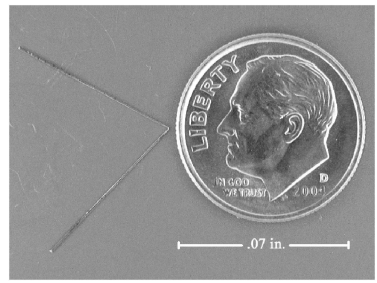

FIG. 5—*V-shaped specimen.*

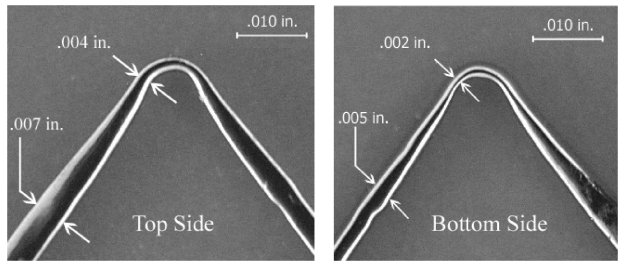

FIG. 6—*Width change due to tapering side walls.*

Width taper occurs during the laser cutting of the specimen from tube stock and is greatest along the axial cut direction and less along the transverse cutting directions. A severe example of taper is shown below in Fig. 6. Note in the right side image of Fig. 6 (bottom side) how that the short depth of field of the optical microscope prevents the viewer from seeing the larger width of the deeper top side edge.

To understand the effect measurement error would have on FEA prediction, a preliminary geometry sensitivity study was performed. The study calculated the change to maximum compression strain of the specimen when changing the width of the vertex from 0.004 to 0.006 in. The study concluded that changing the width of the curved vertex by the range above would result in a 237 % increase in compression strain.

The sensitivity described above suggests that an error may have been introduced in the FEA analysis if the width data of the V section was inaccurate. It was true that the original measurements did not consider variations due to side tapering that would have produced a different vertex width input value. Therefore, surviving test specimens that had undergone 2 % mean strain (ε_m 2 %) with 2.35 % alternating strain (ε_a 2.35 %) to 1.0+E08 cycles were selected for re-measuring.

Re-Measurement Data

To confirm the width assumption requires re-measurement of width from both sides of a part. The original data of the same three specimens at position "A" and "B" were compared with re-measured averages, Ar and Br (see Fig. 7).

Results of the re-measurement of the specimens showed that one of the three, (#4v72), had enough side taper to affect the results significantly had the data been considered (see Fig. 8). However, the difference between the specimens was not a factor in the original FEA because an average of all three samples was used and according to the re-measurement the actual average dimensions of #4v72 were much closer to the other specimens. Therefore the missed error was negated.

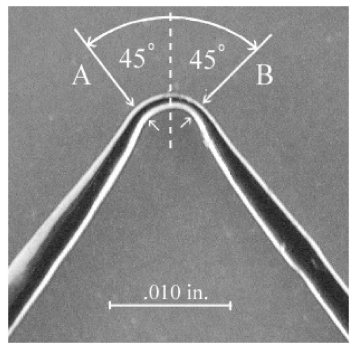

FIG. 7—*Location on V shape of dimensions for re-measurement.*

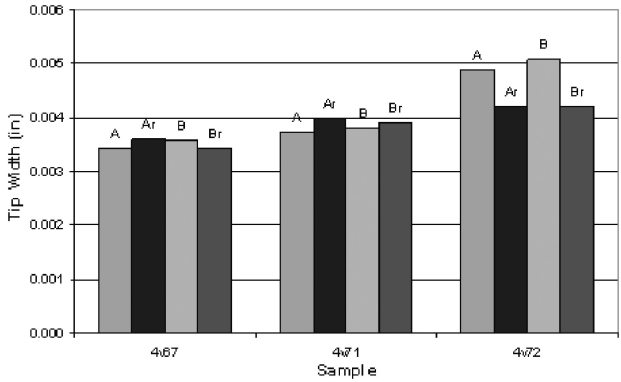

FIG. 8—*Re-Measurement of V width "A" and "B".*

Bench Test Strain Measurement

To verify that the FEA strain predictions were accurate, a novel method to determine surface compressive strain on small specimens has been developed. A V-shaped specimen was loaded in a fixture that can simulate the same compression and tension geometries used during fatigue testing by moving an adjustable slide that holds the leg of the V specimen (see Fig. 9). To simulate the fatigue cycle specimen geometry, the gap between the adjustable slide and the fixed slide was set equal to the gap between slides in the fatigue tester.

The fixture with specimen was mounted in an SEM where the distance between surface "markers" on the inside surface of the V specimen were measured before and after geometry changes. Different alloys of nitinol can produce different markers. An example of surface precipitates viewed in silhouette is shown in Fig. 10. The specimen images shown below were prepared by mechanical removal of laser cutting slag followed by electrochemical polishing.

Pairs of surface defects on the inside surface of the V were used as markers for the nitinol specimens from the Harrison and Lin experiment. See an example of surface defects in Fig. 11. When surface defects are used as markers for multiple measurements it is important to select those with high contrast and acute edges so that they can be easily located when respective measurements are performed. Additionally, the line between markers needs to be perpendicular to the beam to provide as clear an image as practical.

Measurements across the range of 5 % compression to 8 % tension have been made and describe a pattern consistent with theory. The differences in strain between the two samples shown in Fig. 12 are attributed to variations in individual part geometry.

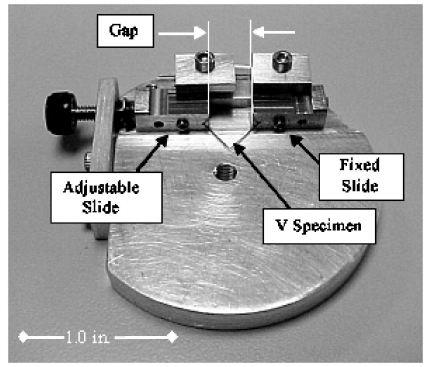

FIG. 9—*Fatigue simulation fixture with mounted V specimen.*

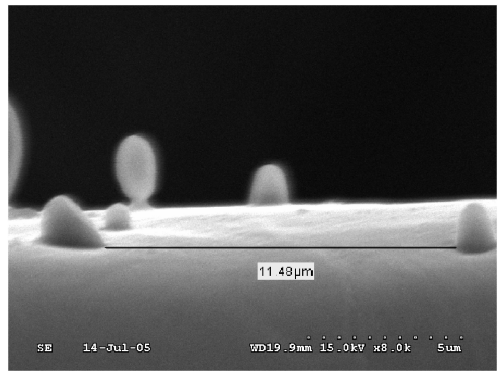

FIG. 10—*Measuring distance between silhouetted surface markers of a nitinol alloy.*

Nitinol Fatigue Sample Verification

The technique described above was applied to the surviving fatigue samples reported on in the Harrison paper. The units chosen were those which had undergone 2 % mean strain (ε_m 2 %) with 2.35 % alternating strain (ε_a2.35 %) and survived 1.0E+08 cycles.

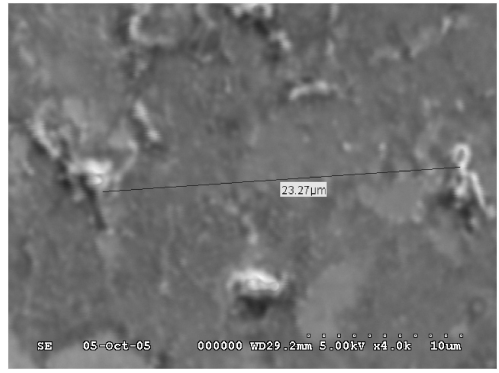

FIG. 11—*Measuring perpendicular to specimen face between nitinol surface defects.*

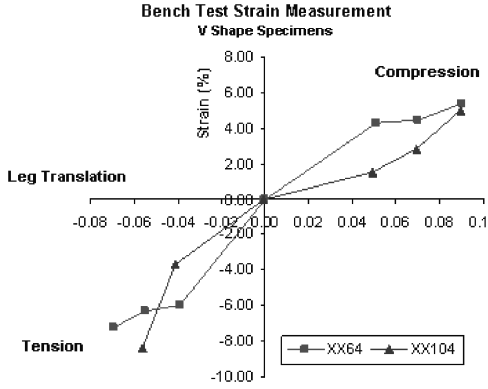

FIG. 12—*Specimen bench data.*

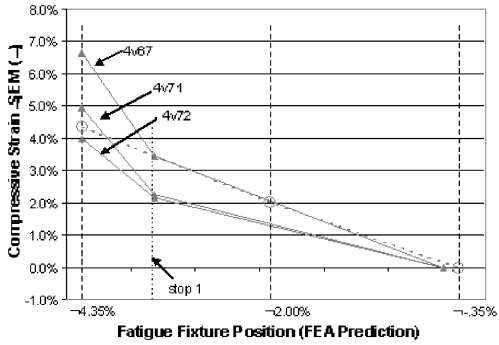

FIG. 13—*Fatigue survivor strain at* ε_m *2 % with a* ε_a*2.35 %.*

Methodology

Sample Preparation—Surface contaminations that could be mistaken for surface defects were removed from the specimen and fixture by ultrasonically cleaning both in alcohol for 5 min before loading in the SEM.

A specimen was mounted in the fatigue simulation fixture at the maximum compression setting used during the fatigue test that was predicted to be 4.35 %. The sample was oriented within the SEM so that the inside surface of the V was perpendicular to the beam. Two landmarks were identified in the center of the inside surface of the V that were approximately 20 μm apart and were parallel to the direction of compression on the surface. An image was captured at the highest definition scan and transferred to the imaging measuring software program for measurement. A calibrated ruler line was drawn between the two landmarks and the marked image was saved for later reference. The simulation fixture was removed from the SEM and reset to correspond to a lower compression value (stop 1), then returned to the SEM. The same landmarks are located and the process of measuring repeated. The final fixture setting held the V sample under no compression or tensile load (neutral) to establish a zero strain reference. The corresponding compressive strains from the three samples measured in the SEM are shown in Fig. 13 below as triangles. The predicted compressive strain curve is denoted by circles; ε_m 2 % with a ε_a 2.35 %.

Equipment

Hitachi SEM S-3000N

Using Secondary Electronic Image with the following settings:
Accelerate Voltages—5–15 KV
Working Distance—20–40 mm
Magnification—From 100× to 8000×
Quartz PCI V5.1 Scientific Image Management System, Quartz Imaging Corp.

Discussion

The essence of the disparity between the original Harrison-Lin experimental data and other publish data was the higher magnitude of the mean plus the alternating strain. A systematic review of possible contributing errors has ruled out the most probable sources of error. In fact, the SEM measurements confirmed empirically that the actual fatigue specimens were cycled in a strain range higher than the 4 % range predicted by FEA. The strain magnitude trend agrees with the difference in specimens by rank order of V thickness, in that as the V thickness decreased the strain increased.

The higher strain measured on specimen #4v67 raises legitimate questions about sample population homogeneity. Small dimensional variances in the samples create noise in the data. Since a fatigue test group assumes there is strain consistency in the cohorts, had the use of the SEM measurement been preemptively applied to fatigue specimens, specimen #4v67 would have been removed from the sample

pool and replaced with a more appropriate specimen. The use of SEM measuring to pre-qualify specimens for fatigue tests would provide multiple benefits; test groups would be more homogenous, sample populations would be accurately stratified by strain characteristics, and outliers would be identified for further variance root cause investigation.

The only weakness in the data is the few data points included. However, the real world application of these data was to make an intravascular self-expanding stent that would have minimal fatigue fractures. The clinical data that have been reported thus far describes performance for more than 113 stents each of which contains hundreds of struts at risk. The report of low rates of fractures in comparison to other designs [1,2] that provide the same features strongly suggests that the performance seen in fatigue testing has carried over to the engineer's design.

Conclusion

A technique has been developed to measure compressive surface strain by taking the measurements with an SEM. This technique was applied to specimens where there was a question as to the actual magnitude or range of strain, or both on small specimens. The SEM technique provided confirmation that the FEA predicted strain levels of ε_m 2 % with a ε_a 2.35 % were achieved.

Accurate FEA analysis and material characterization are joined at the hip. The use of the SEM to make direct surface measurements on small test specimens enables the FEA analyst to construct and validate an individual specimen model. In this case the true performance of three samples was not only shown to be close to the intended performance but the compliance is known for each specimen. This allows the engineer to place each specimen exactly where it belongs on the cycle to failure curve.

The engineers cannot foresee all the ramifications of their work. The importance of microscopic changes recorded in the SEM's vacuum chamber swells to life size when the product performs poorly. As described by Schlager and Scheinert, the state of endovascular stent strut failure has become of such great interest to clinicians that hospitals are re-examining implanted stents for mechanical integrity and reporting the results for each design.

And so we return to Hoover's comment on the visibility of the engineer's endeavor…"*If his works do not work, he is damned.*"

Acknowledgments

The author would like to thank Z. C. Lin, Ph.D., for his contributions of SEM silhouette measurement technique and photo.

References

[1] Schlager, O. et al., "Long-Segment SFA Stenting—The Dark Sides: In-Stent Restenosis, Clinical Deterioration, and Stent Fractures," *J Endovascular Ther*, Vol. 12, 2005, pp. 676–684.

[2] Scheinert, D. et al., "Prevalence and Clinical Impact of Stent Fractures after Femoropopliteal Stenting," *J. Am. Coll. Cardiol.*, Vol. 45, 2005, pp. 312–315.

[3] Lin, Z. C., and Denison, A., "Nitinol Fatigue Resistance—A Strong Function of Surface Quality," *Proceedings of the Materials and Processes for Medical Devices Conference 2003*, 8–10 September 2003, Anaheim, CA, pp. 205–208.

[4] Harrison, W. J., and Lin, Z. C., *SMST-2000: Proceedings of the International Conference on Shape Memory and Superelastic Technologies*, S. M. Russell and A. R. Pelton, Eds., (Pacific Grove, CA: International Organization on SMST, 2001) pp. 391–396.

[5] Pelton, A. R., Gong, X. Y., and Duerig, T., "Fatigue Testing of Diamond-Shaped Specimens," *Proceedings of the International Conference on Shape Memory and Superelastic Technologies*, 5–8 May 2003, Asilomar Conference Center, Pacific Grove, CA.

SECTION II: ANALYSIS, CHARACTERIZATION AND STANDARDS

Journal of ASTM International, Vol. 3, No. 6
Paper ID JAI13581
Available online at www.astm.org

Kyle C. Koppenhoefer,[1] *Jeffrey S. Crompton,*[1] *and James R. Dydo*[1]

Prediction of Failure in Existing Heart Valve Designs

ABSTRACT: Artificial heart valves must be designed to survive greater than 109 cycles over 40 years of operation. Thus, fatigue represents one of the primary driving forces for safe operation of these devices. The inability to maintain the long term performance of critical devices in the future may lead to catastrophic failure and patient loss of life. The Bjork-Shiley convexo-concave (BSCC) heart valve provides an excellent case study in heart valve design. Approximately 86 000 valves were implanted from 1979 to 1987 and approximately 1 % of the valves experienced failure due to fatigue. Failures of this type are likely to yield a 70 % mortality rate in patients. To understand the conditions that produced failure, a detailed engineering assessment was conducted to determine valve designs, manufacturing processes, and physiologically related loading conditions that gave rise to an increased risk of failure. The material used in constructing the valve, Haynes 25, possesses good long crack threshold fatigue properties (ΔK_{th}=4.5 MPa$\sqrt{m}$). However, continued operation of the valves produced cracking under certain physiological circumstances. These assessments indicate that a small subset of valves may operate under conditions that are close to the boundary between continued safe operation and catastrophic failure. These findings should be considered when using materials with inherently lower threshold fatigue properties. Crack growth data show that Nitinol has a threshold stress intensity factor ≈2 MPa$\sqrt{m}$, or less than half that of Haynes 25. Thus, current heart valve designs that use Nitinol should incorporate lessons learned from analyses of the BSCC heart valve to assess the likelihood of premature valve failure due to repeated loading.

KEYWORDS: Bjork-Shiley, short cracks, Haynes 25, Nitinol, threshold, heart valves

Introduction

In the year 2000, approximately one million artificial heart valves were operating in the United States. This number continues to grow as every year more than 80 000 adults undergo surgical procedures to repair or replace damaged heart valves [1]. Engineers that design and manufacture these valves must consider the need for these valves to survive extremely large cycle counts. The human heart beats approximately 38 million times per year. Thus, valves experience 10^6 cycles, typically specified as the endurance limit for most engineering materials, in less than one year of operation. Fatigue loadings with cycle counts greater than 10^6 cycles occur in many engineering structures. However, these systems often are designed with large safety factors, and have more opportunities for inspection than an artificial heart valve. Size constraints, complex loadings, and inaccessibility require these designs to operate outside of typical practices for traditional engineering structures.

Cardiologists adopted the Bjork-Shiley convexo-concave (BSCC) heart valve, as shown in Fig. 1, for general use in 1979. During the eight years that the valve was on the market, approximately 86 000 valves were implanted in patients. Six hundred and fifty-seven valves (or 0.76 %) experienced outlet strut fracture (OSF), as of October 31, 2005. These failures produced a mortality rate of approximately 70 %. Inspections of valves that experience OSF indicate progressive crack growth across the base of the outlet strut that resulted in complete separation of the outlet strut from the valve support ring. All OSFs occurred in designs manufactured prior to design changes implemented in 1984.

This paper provides an overview of a detailed investigation into the loading mechanisms that produced OSF in this valve design. In addition to providing an overview of the failure mechanism in the BSCC, this paper enumerates lessons learned from this case study in an effort to reduce the likelihood of repeating these errors in future heart valve designs.

Manuscript received November 8, 2005; accepted for publication March 2, 2006; published online May 2006. Presented at ASTM Symposium on Fatigue and Fracture of Medical Metallic Materials and Devices on 7–11 November in Dallas, TX; M. R. Mitchell and K. L. Jerina, Guest Editors.
[1] Principal, Advanced Computational & Engineering Services, 750 Cross Pointe Road, Columbus, OH 43230.

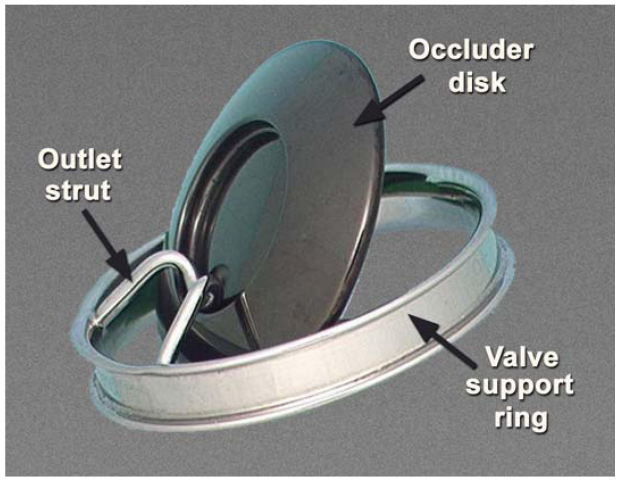

FIG. 1—*Bjork-Shiley convexo-concave heart valve.*

Fatigue Life Estimation

Current fatigue life estimation techniques fall into two broad categories: stress/strain life methodologies, and damage tolerant approaches. Although both techniques have been used to assess the fatigue life of the BSCC valve, the work presented in this paper focuses on a damage tolerant approach. This methodology assumes immediate crack initiation and that the remaining life can be computed from the number of cycles for the largest undetected flaw to grow to failure. During crack extension, the rate of growth depends on the stress intensity factor of the crack as specified by

$$K = \sigma\sqrt{\pi a} f(g) \tag{1}$$

where $f(g)$ is a function of the geometry of the part. This equation holds within the bounds of linear elastic fracture mechanics. During cyclic loading of the crack, extension per cycle, da/dN, occurs as a function of the change in stress intensity factor, ΔK, according to Paris' Law [2]

$$\frac{da}{dN} = C\Delta K^m \tag{2}$$

where C and m are constants that depend on the material, environment, and stress intensity range. This equation describes fatigue crack extension over the range $10^{-2} \leqslant da/dN \leqslant 10^{\circ}$ μm/cycle. As shown in Fig. 2, this region is typically referred to as Stage B (or II). At extremely low crack growth rates, where $da/dN \leqslant 10^{-3}$ μm/cycle, Paris' Law becomes conservative as cracks exhibit negligible growth. This region, typically referred to as Stage A (or I), is dominated by the threshold response of the material specified by ΔK_0, as shown in Fig. 2.

The concept of a threshold ΔK applies to cracks that are large compared with the microstructure of the metal and the crack tip plastic zone. For cracks that are small relative to these length scales, additional analysis must be conducted to determine crack extension. These analyses may utilize S/N data to include the effects of samples with vanishingly small cracks. Thus, threshold ΔK becomes a function of crack size for these small cracks,

$$\Delta K_0(a) = \Delta\sigma_e\sqrt{\pi a} f(g) \tag{3}$$

where $\Delta\sigma_e$ is the endurance limit of the material determined by S/N testing to $>10^6$ cycles.

This damage tolerant methodology provides the basis for determining the remaining life of the BSCC valve. The following sections describe the techniques developed to implement this methodology for a structure with significant geometric variability subjected to complex loadings.

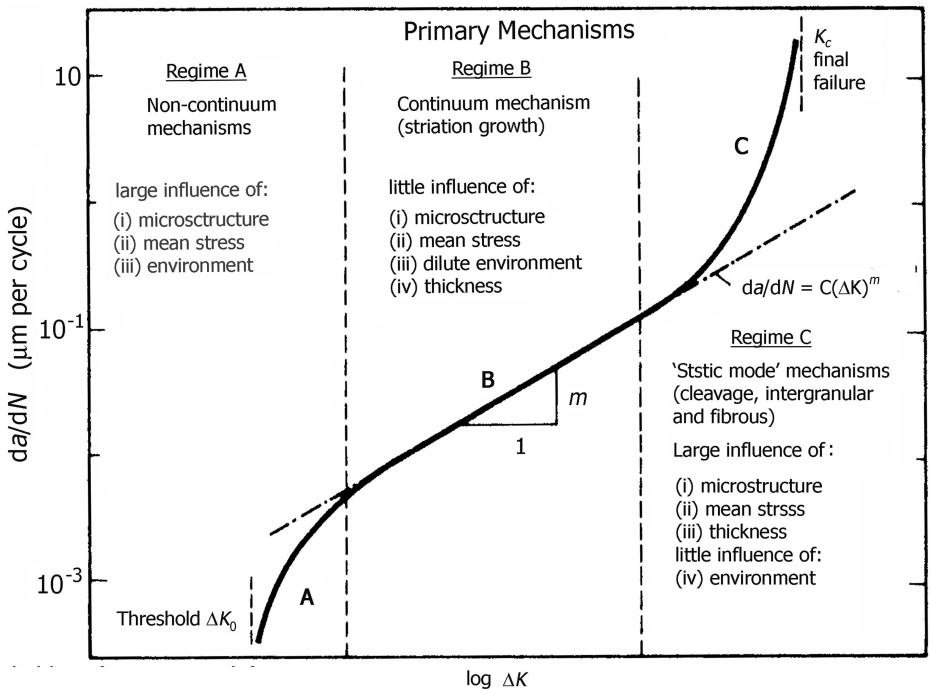

FIG. 2—*Typically fatigue crack extension response of materials.*

Load Mechanism

Experimental work on the BSCC valve [3] indicates loading of the outlet strut occurs during closing of the occluder disk. This work suggests that "over-rotation" of the disk causes the disk to contact the outlet strut. The term "over-rotation" defines the response of the disk measured by proximity detectors located on the end of the disk furthest from the outlet strut. Measurements from this sensor indicate this point on the disk has a larger displacement during the closing event than the final resting displacement of the valve. Detailed finite element analyses of the closure event show the displacement and rotation of the disk follows a complex path that could not be fully understood by measuring displacement at a single point. Figure 3 shows a simple rigid bar representation of the displaced shape calculated from the FEA. These shapes are consistent with experimental measurements. However, these results show that "over-rotation" only accounts for a part of the disk motion, and that disk "rebound" from contacting the inlet strut accounts for contact with the outlet strut that produces stress at the base of the outlet strut.

The significant difference in diameter between the inlet and outlet struts suggests designers may have assumed the inlet strut alone would support the closing of the disk. However, experimental and numerical work indicates a significant load on the outlet strut due to disk rebound during the closing event. This work shows that the rebound load is sufficient to produce cracking of the outlet strut that leads to separation from the valve ring.

Variables Affecting Loading

The load magnitude produced on the outlet strut due to disk rebound depends on patient physiology and details of the valve design that changed over time. Compliance of the material supporting the valve and blood flow properties represents two of the most critical physiological variables. The compliance of the surrounding tissue changes with age and affects outlet strut loading in two ways. First, decreasing the compliance of the support increases the stresses on the outlet strut. Secondly, compliance changes in the

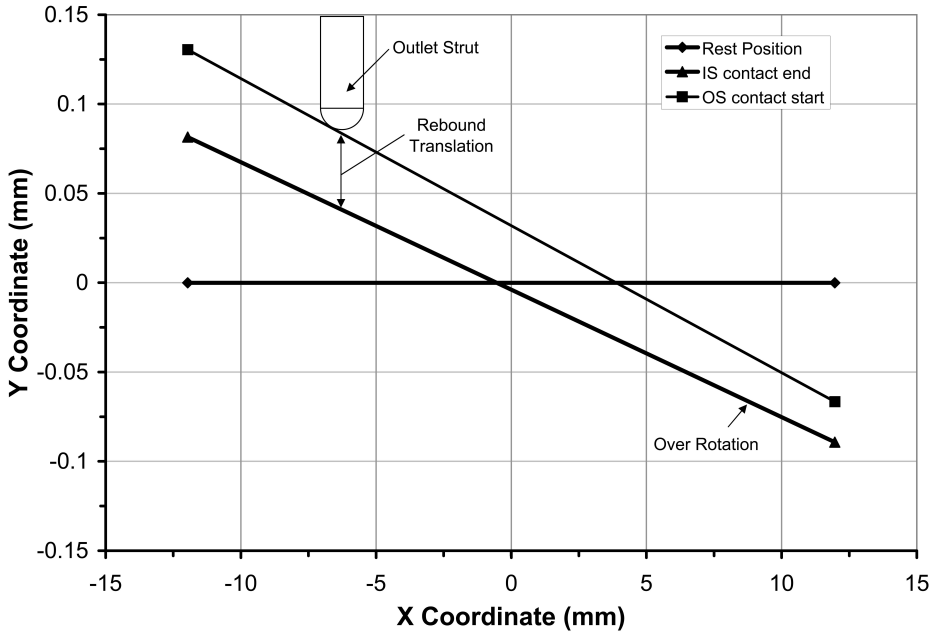

FIG. 3—*Line diagram representation of disk motion during closure event as calculated from detailed finite element analysis. The disk over rotates beyond the rest position prior to rebounding from the inlet strut (IS). Translation due to rebounding generates contact with tip of outlet strut (OS).*

vessels supplying blood flow to the valve affect the mass of blood that is arrested due to disk closure; highly compliant systems will absorb the back pressure created when flow is stopped, the momentum of the closure will be reduced and result in lower stress on the outlet strut. The force of impact of the occluder disk with the outlet strut is proportional to the closing velocity of the disk. The closing velocity is affected by the pressure of the blood flow causing disk closure which in turn can be affected by a number of patient specific factors. The local flow conditions will also produce differing impact of the disk on the strut depending on whether the valve is in the aortic or mitral position.

In addition to these physiological factors, several changes to the valve design during production strongly influence the stress on the outlet strut. The valve design underwent a large number of design changes from 1979 to 1984. Analyses conducted in this work indicate two changes significantly reduced stress at the base of the outlet strut. In 1982 the distance between the tip of the outlet strut and the corresponding contact point in the occluder disk was increased from 0.076 mm to a "visible gap" of approximately 0.25 mm. Then, in 1984 the position of the strut legs were moved closer to the center of the stiffener ring.

The distance between the "hook" of the outlet strut and the "well" in the occluder disk influences the loading of the outlet strut. A large distance between these two features reduces the stress on the outlet strut, because the blood pressure operates against the disk and conducts more work on the rebounding disk as this distance increases. If the distance the rebounding disk must travel prior to contacting the outlet strut hook is sufficiently large, then the occluder disk contacts the base of the outlet strut prior to contacting the hook. In this case, the stress at the base of the outlet strut decreases significantly. Thus, design changes that move the outlet strut closer to the closed position of the disk operate in conjunction with the hook-to-well distance to decrease stress on the outlet strut.

Stress in Failure Region

Finite element modeling that used intimately coupled fluid-structure interactions to represent the closure event indicates that typical physiological loading of the outlet strut can produce stresses at the base of the

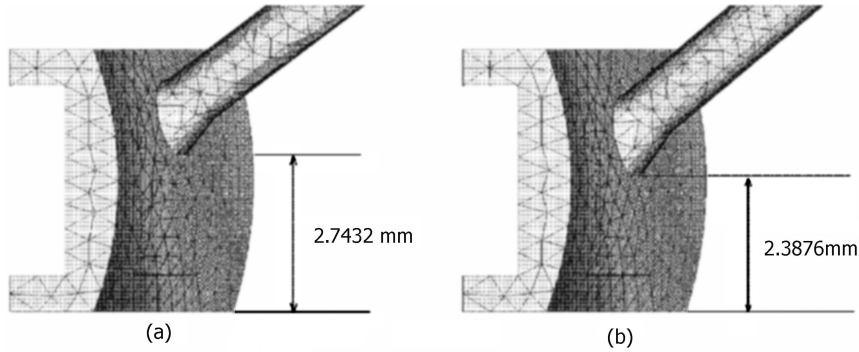

FIG. 4—*Location of outlet strut on valve support ring with legs located in the (a) high and (b) low positions.*

outlet strut that range from 5 to 400 MPa. Details of the valve construction and rigidity of the supports generate this large variation in stress, as indicated previously. The location of the outlet stress along the width of the valve support ring produces the most significant variation in stress. As the valve design evolved during the manufacturing process, the outlet strut position varied from 2.39 to 2.74 mm from the base of the ring, as shown in Fig. 4. This variation in strut position greatly affects the stress in the failure region. Figure 5 shows the variation of stress with hook-to-well distance for these two strut positions. For the lower outlet strut position, the occluder disk makes contact with the base of the outlet strut and reduces the force on the outlet strut tip. Sufficiently large hook-to-well gaps (>0.09 mm) produce a condition

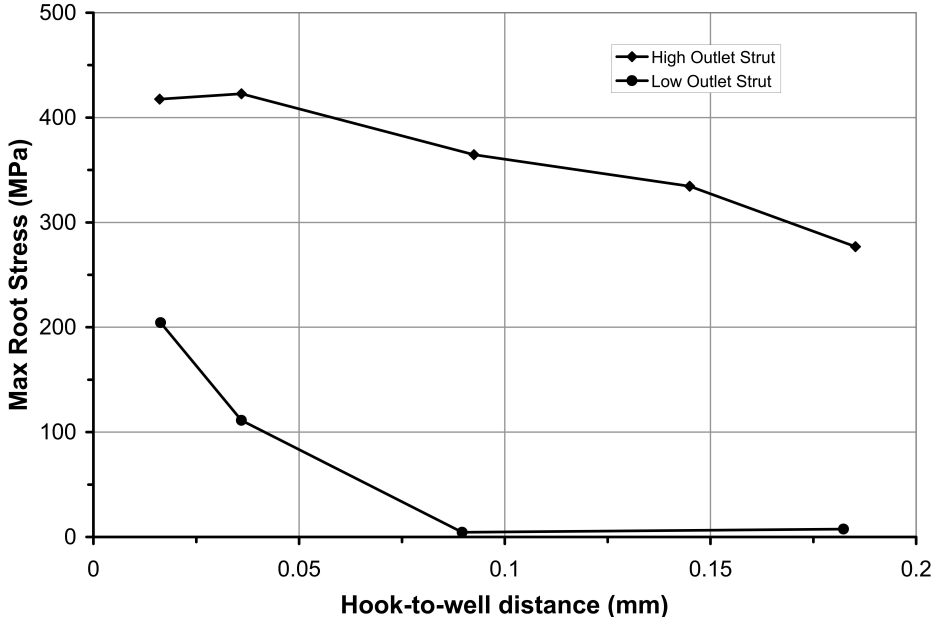

FIG. 5—*Effect of hook-to-well distance on stress at base of outlet strut—rigidly supported ring. The high outlet strut location is 2.74 mm above the base of the outlet strut. The low outlet strut position is 2.39 mm above the base of the outlet strut.*

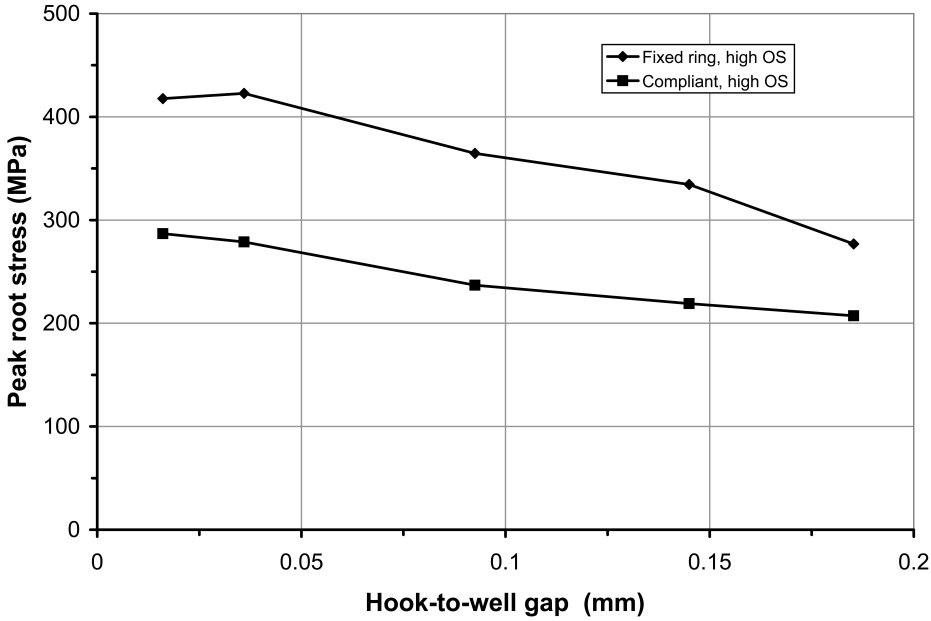

FIG. 6—*Effect of hook-to-well distance on stress at base of outlet strut for legs positioned high on support ring—compliant support* ($K_{total} = 8 \times 10^5$ *N/m).*

where the outlet strut tip remains unloaded by the occluder disk. Thus, small changes in the geometry of the valve generate significant differences in the stress at the location of cracking.

The stresses presented in Fig. 5 show the effect of hook-to-well distance for a rigidly supported valve. These results generally represent an upper bound for the specific conditions. Figures 6 and 7 show the effect of compliance on the peak stress at the region of failure. These results were generated using a total spring constant of 8×10^5 N/m. The 75 MPa stress observed for the compliant support condition in Fig. 7 develops due to the vibrational response of the outlet strut supported by a spring mass system. These stresses do not develop in the rigid support case due to the lack of vibrational response of the ring.

Thus, finite element analysis of the valve mounted within a compliant support indicates stresses at the base of the outlet strut may range from 75 to 300 MPa under typical physiological loading. These calculations represent the most accurate estimate of the stresses in the failure region.

Stress Intensity Factor

Equation 1 provides the general form for the stress intensity factor, K. To determine K for a specific crack size within a finite geometry, the geometry function $f(g)$ must be determined. Ng and Fenner [4] determined the functional variation of K over a range of crack size to diameter ratios (a/D) for a cylindrical geometry subjected to a bending load. These solutions do not consider $a/D < 0.1$. To determine K for these smaller cracks, solutions obtained by Raju and Newman [5] were used. By combining the solutions from these sources, the value of K can be calculated over the full range of typical crack sizes.

Initial Flaw Size

To determine the typical initial flaw size in the failure region, a detailed metallurgical investigation was conducted. Figure 8 shows a typical observed flaw. These cracks occur in the weld at the base of the outlet strut. Typical lengths range from 10–100 μm (or $0.009 \leq a_i/D < 0.09$ for $D = 1.1$ mm). These flaws develop due to cracking of the interdendritic regions in the intermetallic compounds formed during solidi-

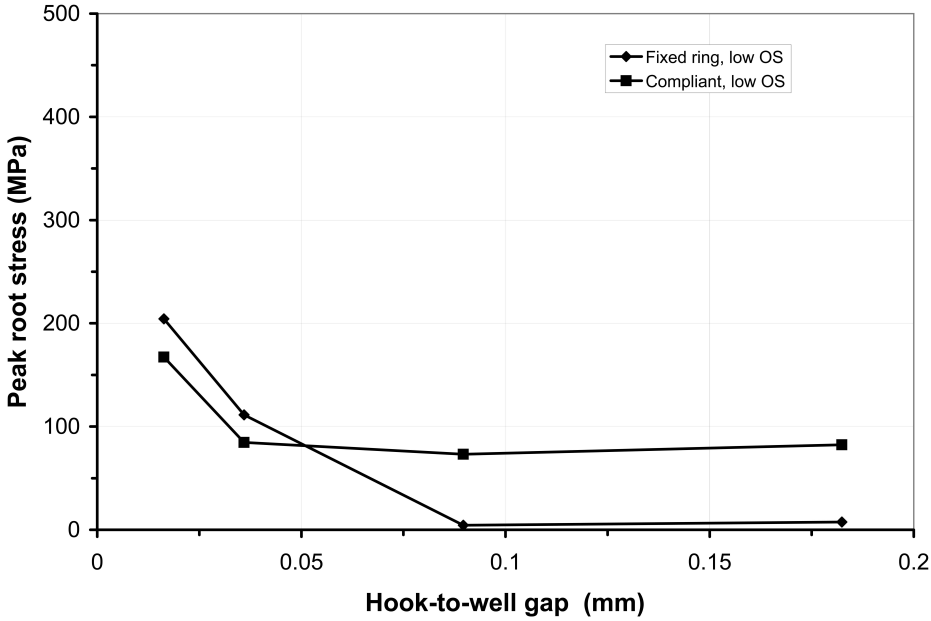

FIG. 7—*Effect of hook-to-well distance on stress at base of outlet strut for legs positioned low on support ring—compliant support* ($K_{total} = 8 \times 10^5$ *N/m).*

fication after welding. This range of flaw sizes, when combined with the applied stress and stress intensity solutions, provide the basis for assessing the likelihood of fatigue crack extension.

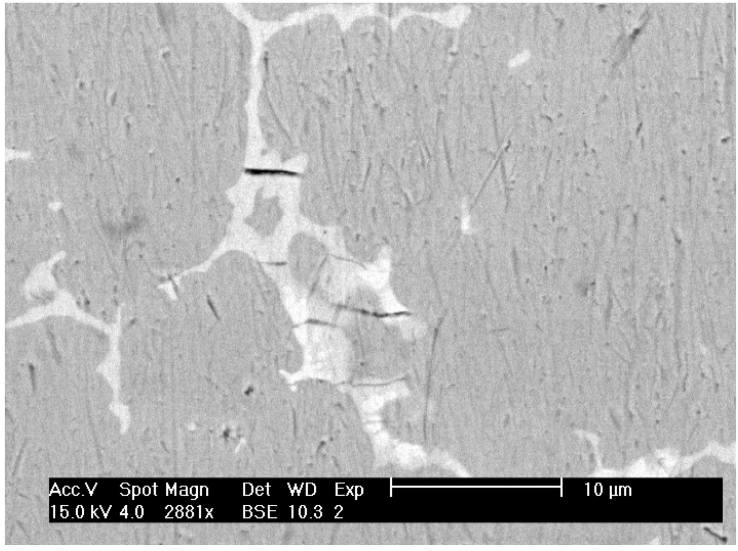

FIG. 8—*Typically observed pre-existing flaws in weldment at the base of the outlet strut.*

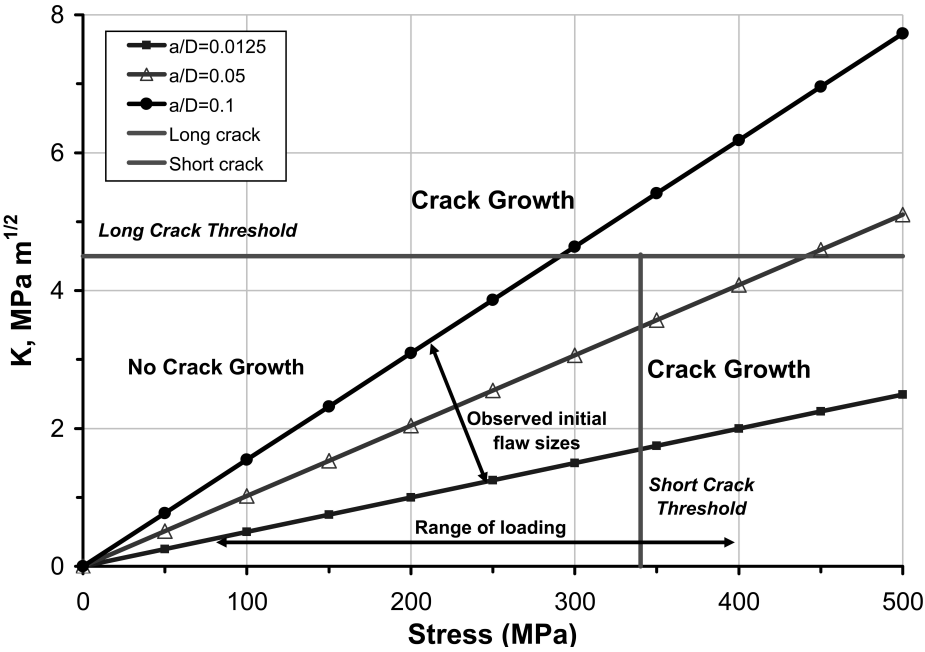

FIG. 9—*Regions of safe and unsafe operation for the 29 mm BSCC valve.*

Fatigue Crack Growth Behavior

A detailed understanding of the fatigue response of the outlet strut may be developed by using the fatigue crack propagation methodology specified in Eqs 2 and 3. This methodology requires the applied stress range, K solution, initial flaw size, and material properties. The previous sections specify the inputs for stress, K solution, and initial flaw size. Experiments conducted by Ritchie and Lubock [6] indicate that for the material of construction, Haynes 25 alloy, $\Delta K_{th}=4.5$, $C=7.1e^{-20}$, and $m=12.2$ in units of MPa$\sqrt{\text{m}}$ and m/cycle. To address the issue of short cracks, experimental work conducted by Green et al. [7] indicates $\Delta\sigma_e=340$ MPa. Thus, the failure envelope for the specified loading, materials, and geometry appears in Fig. 9. Alternating stresses in excess of 340 MPa should produce crack extension for any initial flaw size. Stresses between 275 and 340 MPa produce crack extension for initial flaw sizes of $a_i/D>0.075$. For stresses less than 275 MPa, crack extension should not occur over the range of measured initial flaw size.

Valve Life

Available records indicate 657 outlet strut failures as of October 31, 2005 [8]. Of these total failures, 123 valves where designated as having a diameter of 29 mm. A statistical analysis of 29 mm valve failures indicates three outlet strut fractures within the first year after implantation. These failures may be attributed to typical operating stresses generating crack extension from flaws of typically observed sizes. Records indicate the shortest valve operating time prior to failure was approximately three months. This time frame appears consistent with a near threshold crack growing due to typical operating stresses assuming long crack fracture mechanics [9]. Outlet strut fractures between three and twelve months are consistent with crack extension from short cracks subjected to typical operating stresses in excess of 275 MPa.

In the time frame of two to ten years after implantation, approximately ten 29 mm valves failed per operation year. Failure data indicate one failure a year over the operating lives of 20 to 23 years. The most recent failure occurred in 2004 after 23 operating years. Due to the large cycles per year experienced by these valves (~38 million), typical cycles must generate stresses less than 275 MPa. Thus, these cycles do not damage the outlet strut through fatigue. The damaging cycles in these failures must be associated with

atypical, short term load excursions and not continued loading associated with typical physiological conditions. Damage accumulated during these extreme cycles extends small cracks until they obtain a flaw size that grows under typical operating conditions. At this point, the outlet strut fractures within one year of typical operation.

Design changes implemented in 1984 reduce the stress on the outlet strut below 250 MPa under all loading conditions considered in this work. Thus, initial flaw sizes less than 100 μm should not extend and mechanical damage should not accumulate during the lifetime of the valve. These results are consistent with epidemiological work that indicates no failures for valves manufactured after 1984.

Summary and Conclusions

The Bjork-Shiley convexo-concave (BSCC) heart valve experienced fracture of the outlet strut due to fatigue cracking from initial weld defects. These initial flaws grew under fatigue loading generated from contact forces necessary to stop the occluder disk during closure. Initial designs may not have accounted for the contact between the outlet strut and disk during closure. However, computational analyses indicate the disk rebounds from initial contact with the inlet strut to generate significant contact forces with the outlet strut during normal operations. For the most severe cases considered, stress intensity factors at the base of the outlet strut exceed the threshold ΔK (i.e., largest nominal load and largest observed crack size). These conditions may account for the outlet strut fractures observed within the first several years of operation. For the pre-1984 design, a range of different flaw size and loading combinations indicates failure may occur after extremely large operating times, i.e., greater than 20 years. These conditions indicate fatigue damage accumulates only during occasional cycles with loads significantly larger than nominal conditions. This damage accumulates over many years until the crack grows to a size where ΔK exceeds threshold for nominal loading. At this point, fracture of one outlet strut leg occurs within a year of operation.

Design changes implemented in 1984 appear to reduce ΔK values at the base of the outlet strut below threshold values for all loading conditions and initial flaw sizes considered in this work. This design change generates contact at the base of the outlet strut instead of the tip. Thus, the bending moment that produces high stress in the failure region decreases significantly and the corresponding ΔK decreases.

The outlet strut of the BSCC valve is constructed from Haynes 25. This material has a $\Delta K_{th} = 4.5$ MPa$\sqrt{\text{m}}$. The threshold stress intensity factor for Nitinol is approximately 2 MPa$\sqrt{\text{m}}$, or less than half that of Haynes 25. Thus, greater diligence must be exercised in designing and manufacturing heart valve components constructed with Nitinol than valves constructed from Haynes 25.

Previous experience with the BSCC valve suggests that engineers must seek to fully understand the operation of these complex biomechanical devices. These efforts must be expended due to the repercussions associated with heart valve designs. The necessary service life of these valves combined with the risk of explantation generates long lasting consequences for poor designs. Thus, advanced engineering tools and methods must be employed to address all possible loading scenarios, and to determine the likelihood of significant alternating stresses for parts constructed from Nitinol, or any other engineering material. The high cycle count of even infrequent loadings requires engineers to design for fatigue due to loadings several standard deviations from the mean loading. These fatigue assessments should be conducted using long crack, short crack, and stress-life methodologies. Finally, engineers should consider methods of inspecting future designs using minimally invasive procedures. Parts that have been identified as experiencing fatigue loadings should include some characteristic consistent with the health of the part that can be identified by an external probe.

Acknowledgment

The authors wish to thank the The Bowling-Pfizer Supervisory Panel and the Trustees of the Bowling-Pfizer Settlement Fund for support and permission to publish this work.

References

[1] Lankford, J., "Assuring Heart Valve Reliability," *Tech Today*, SWRI, 1999.
[2] Paris, P., and Erdogan, R., "A Critical Analysis of Crack Propagation Laws," *ASME J. Basic Eng.*, Vol. 85D, 1963, pp. 528–534.
[3] Eberhardt, A. C., Ward, M. A., Lewandowski, S. J., Inderbitzen, R., and Wieting, D. W., "Relationship Between Closure Delay, Pressure, Velocity and Outlet Strut Forces of the Bjork-Shiley Heart Valve," *Adv. Bioeng.*, Vol. 26, 1993, pp. 547–550.
[4] Ng, C. K., and Fenner, D. N., "Stress Intensity Factors for an Edge Cracked Circular Bar in Tension and Bending," *International Journal of Fracture*, Vol. 36, No. 4, 1988, pp. 291–303.
[5] Raju, I. S., and Newman, J. C., "Stress-Intensity Factors for Circumfrential Surface Cracks in Pipes and Rods under Tension and Bending Loads," *Fracture Mechanics: 17th Volume, ASTM STP 905*, J. W. Underwood, et al., Eds., ASTM International, West Conshohocken, PA, 1986, pp. 789–805.
[6] Ritchie, R. O., and Lubock, P., "Fatigue Life Estimation Procedures for the Endurance of a Cardiac Valve Prosthesis: Stress/Life and Damage-Tolerant Analyses," *J. Biomech. Eng.*, Vol. 108, May, 1986, pp. 153–160.
[7] Green, A., Sieber, H., Wells, D., and Wolfe, T., Technical Documentary Report No. ML-TDR-64-116, Air Force Systems Command Wright-Patterson Air Force Base, OH, October, 1964.
[8] Personal Communication with Dr. Donald Harrison, Bowling-Pfizer Supervisor Panel.
[9] Dydo, J., Koppenhoefer, K., Yushanov, S., Mohr, W., and Khurana, S., "Outlet Strut Fracture of BSCC Heart Valves," The Bowling Pfizer Supervisory Panel, 2001.

Journal of ASTM International, Vol. 4, No. 6
Paper ID JAI100390
Available online at www.astm.org

Mitesh M. Patel[1]

Characterizing Fatigue Response of Nickel-Titanium Alloys by Rotary Beam Testing

ABSTRACT: Fatigue information has been reliable in predicting wire critical structural integrity. The aim of this study is to expound on the characterization technique of rotary beam fatigue testing (RBT). By alternating tension and compression stress states through RBT, it is possible to determine the life expectancy of Nitinol monofilament round wires. Fatigue testing has been employed to characterize the influence of subtle changes in inclusion content, chemistry variations of raw material, ingot transformation temperatures of Nitinol (NiTi), and surface finish conditions for implant grade wires. Currently, an ASTM standard does not exist that concentrates solely on fatigue testing shape memory alloys. By exploiting part geometry, this testing technique serves to compliment other characterization methods. Evaluation of fracture surfaces has proven useful in diagnosing the factors influencing failures. The utilization of fatigue data and fracture mechanics compliments tensile testing in providing information to the design engineer. Results from studying flexural endurance, statistical Weibull life assessment analysis, fracture analysis, and a determination of stress/strain levels at the site of failure have proven useful in determining desired material properties for next generation medical devices.

KEYWORDS: Nitinol, round wire, rotary beam, fatigue, fracture, $R=-1$, controlled strain

Introduction

Some common fatigue test methods include axial, bending, and torsion. In 2000, a study was conducted using a wire diameter of 0.267 mm to investigate the impact of melt origin on fatigue performance [1]. This research compared the melting practices, final workings, and final shape-setting heat treatment in the metal; however, fatigue lives did not differ for each supplier through bending strains of 0.72, 0.84, 1.0, 1.2, 1.7, and 2.5 %. Figures 1(*a*) and 2(*a*) show the comparison of inclusions found in Supplier A and Supplier B, two common Nitinol material vendors, utilizing scanning electron microscopy (SEM). Longitudinal mounts along the drawing direction were completed on nominal wire diameters of 2.03 and 2.16 mm, for Suppliers A and B, respectively. Energy dispersive X-ray spectroscopy (EDS) spectra shown in Figs. 1(*b*) and 2(*b*) suggest the inclusions are titanium-rich. While some defect particles reside in the bulk of the material, they have also been attributed to the use of contaminated feedstock. These melt-related defects often cause nonhomogeneous microscopic discontinuities that may inhibit slip and act as stress raisers.

Another study utilized a tabletop testing device that oscillates forces, creating a mean strain state of Nitinol materials [2]. It was found that fatigue life of Nitinol diamond-shaped specimens increased for mean strains above 1.50 % at the same alternating strain. In a rotary beam strain-controlled study, varying heat treatments and various test temperatures were imposed [3]. It was proven that in an isothermal strain-controlled environment, superelastic Nitinol was superior to stainless steels. Yang mentioned that fatigue-crack propagation analysis may be used complementary to the results from fatigue testing [3]. A cyclic frequency of 1000 revolutions per minute (r/min) was used in a system equipped with wire fracture detection, cycle counting, and over-temperature protection. The use of fracture surface analysis can be used in conjunction with these types of models.

Through experimentation, one may survey various alloys, suppliers, and processes utilized in the production of medical-grade fine wire. By controlling testing parameters and environments, tensile testing of medical grade Nitinol wires provides ancillary data to *in vitro* RBT analysis. In a similar light, this tool may be used as a quality check prior to shipment to device manufacturers during process validation. Due

Manuscript received October 5, 2005; accepted for publication May 6, 2007; published online June 2007. Presented at ASTM Symposium on Fatigue and Fracture of Medical Metallic Materials and Devices on 7–11 November 2005 in Dallas, TX; M. R. Mitchell and K. L. Jerina, Guest Editors.
[1] Shape Memory Engineer, Fort Wayne Metals Research Products Corporation, Fort Wayne, IN 46809.

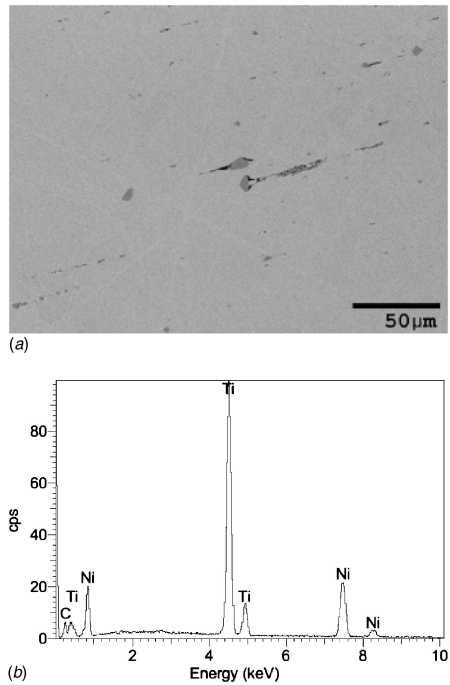

FIG. 1—*1(a) and 1(b)—Typical bulk material from Supplier A at 2.03 mm.*

to the strain gradient in this type of test, any surface anomalies will be dominant in ultimate fatigue failures. The results from RBT may aid in the development of medical device focused safety factors, material development, and process evaluation. Intrinsic and extrinsic attributes, along with variation in processing routes, may all influence the comparison of cycles to failure [4].

The fabrication chain of Nitinol prior to RBT is: melting, hot working, cold working, and shape-setting heat treatment. Altering any chain segment affects final material properties. By using materials with equivalent thermomechanical processing with Ti49.2 at %, Ni50.8 at % as a baseline, derivations of the differences between in NiTi wire properties and performance are possible. As will be explained subsequently in detail, the greatest tensile and compressive normal forces are exerted at the outermost fibers of a round wire during RBT. The testing modus operandi does not solely focus on the end use of Nitinol products; it is regularly implemented as standardization of material quality.

Throughout RBT, the mechanical deformation that takes place in a solid wire may be studied as a member in pure bending. In this light, the wire contains a plane of symmetry and is exposed to equal and opposite couples (M and M′) acting in the plane of symmetry at the ends of the wire. As depicted in Fig. 3, the solid wire will bend concave upward and uniformly under the action of the couples, but will remain symmetric with respect to that plane. The wire is curved due to bending forces, analogous to the means of reaction flexure occurs when a wire experiencing forces in the cardiovascular system. The upper surface is in compression, while the lower surface is in tension. A dashed line through the core of the wire presents the neutral axis (NA), shifted to the compressive side.

At any point a finite distance from the neutral axis is under flexural loading, and there is a state of uniaxial stress from the σ_x component. In Fig. 4, segment AB shortens, while A′B′ lengthens as $M > 0$. The upper face of the wire is in compression with ε_x and σ_x being negative (−). The lower face, with ε_x and σ_x being positive (+), indicates a tension state. The neutral surface, the surface parallel to the upper and lower faces of the wire, has $\varepsilon_x = \sigma_x = 0$. The distance from any point to the neutral surface is noted as "y," ρ signifies the radius of arc *DE* (*NA*), and the central angle to *DE* is θ, knowing that the length $DE = L$ [5].

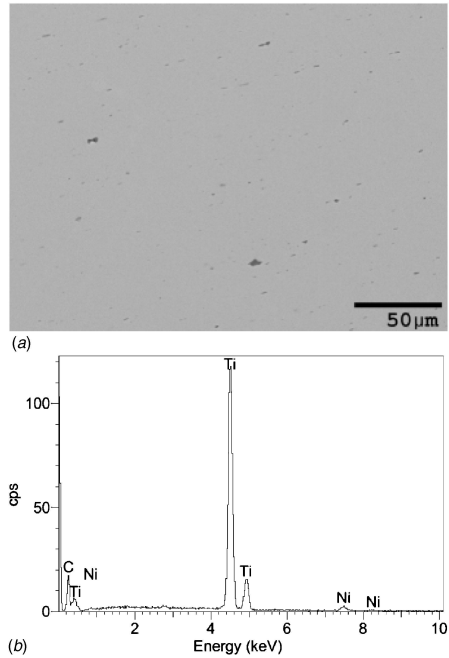

FIG. 2—*2(a) and 2(b)—Typical bulk material from Supplier B at 2.16 mm.*

Rotating the wire samples causes a reversing cyclic stress, where the wire surface experiences an alternating tension and compression state. Figure 5(*a*) shows a strain waveform indicating peak-to-peak variation during a controlled flexure mechanical test through time. At any transition point on the curve, the material is at maximum strain amplitude with an equal amplitude about a zero mean strain ($R=-1$). During testing, the stresses in the material remain below the superelastic limit, as referenced in Fig. 5(*b*); permanent set is nonexistent as the round wire is not yielding.

Materials and Methods

The Valley Instrument Company, Rotary Beam U-Bend Wire Spin Fatigue Tester (10-040) as shown in Fig. 6 may be utilized to test Nitinol wire in the superelastic condition above the Active Austenitic Finish temperature (Active A_f). Rotary beam fatique testing may be conducted in a temperature-controlled ambient air or in a liquid environment. Solvent baths used in experimentation include reverse-osmosis water (RO H_2O), saline, or Ringer's solution [4].

Testing instrument construction involves a motor-driven chuck and an adjustable bushing support that allows variable positioning of the free end of the specimens. The various holes in the bushing-bar provide strain adjustment for the specimen. Using a calculated distance from the chuck to form an arch, the design

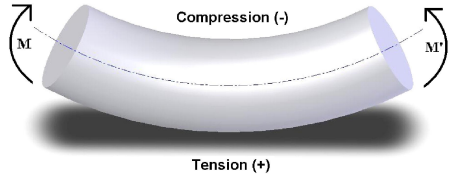

FIG. 3—*Solid wire in pure bending.*

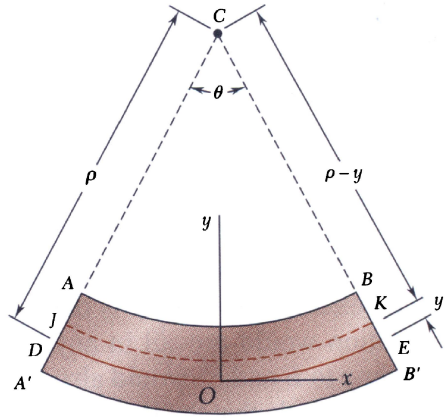

FIG. 4—*Neutral axis DE with radius of curvature ρ as noted [5].*

allows the axis of the chuck and the axis of the loose wire end in the bushing to be exactly parallel, as shown in Fig. 7. The specimen, with a known length, is mounted into the drive chuck system while the "nondriven" end is inserted into the free bushing. To prevent vibration, two support guides are positioned on the radius of the specimen, but outside of the apex, such that the guides do not affect the region of maximum strain.

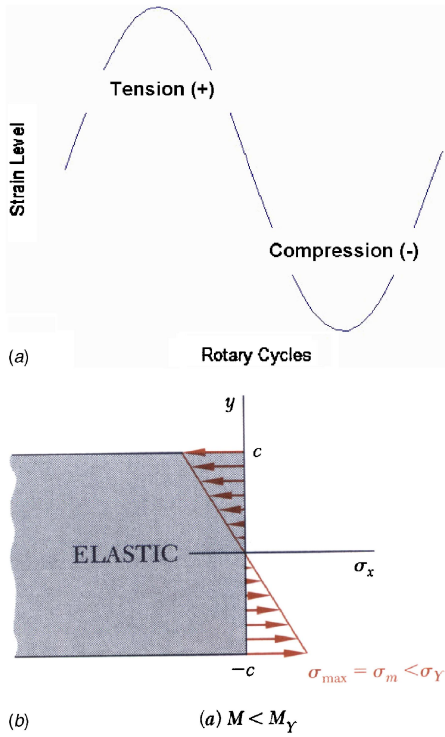

FIG. 5—*(a)—Rotary cycle waveform [3]; (b)—No permanent deformation in the wire taking place [5].*

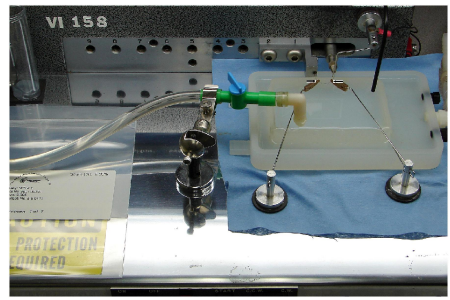

FIG. 6—*Valley instruments rotary beam spin fatigue tester.*

The material is cycled in the chuck by a motor at a constant frequency of 3600 revolutions per minute, synchronous to an electronic clock with a resolution of 1/100th of a minute, thus giving the apparatus a resolution of 36 revolutions each minute [4]. Testing a planned grouping with a randomization of samples is an essential feature of a well-executed experiment. Attempt should be made to balance potentially detrimental effects of variables such as laboratory humidity, while accommodating for possible test equipment malfunction during the test program. The number of specimens, or sample size required, depends on the type of test conducted. Preliminary and exploratory research testing demands a minimum number of specimens to be from six to twelve [6]. Typical strain values may range from 0.60 % to 2.50 %; a strain level is considered low or high if it lies below or above the SIM (stress-induced martensite) strain level, respectively. The SIM appears where a volume of the parent phase of the material, austenite, transforms to martensite due to the application of a stress above that active A_f temperature. At high strain levels twelve samples are typically chosen, due to the expected shortness of the fatigue life; in contrast, six samples are tested at low strain levels. It is worth mentioning that at extremely low levels of strain, the time to failure is long ($N_f \sim > 10^7$ cycles) in relation to high strain levels ($N_f \sim 10^3$ cycles). In addition, it is recommended to set up testing to capture and evaluate data scatter experienced near the SIM strain level. A test protocol may include using multiple strains that are calculated by using the starting bend radius and increasing the center distance.

The reversible force that is incurred on the test sample is constant and stationary with the device. A cycle is counted as the number of turns the chuck completes during testing. The material is cycled to fracture, or continues to a predetermined number of cycles as a runout. At fracture, the instrument electrically grounds the test sample and thus terminates the test automatically. Through comparison of materials, some material or processes may show significant differences regarding cycles to rupture. In regards to lower strain levels, a desired runout time expectancy determination becomes of concern. Reinoehl et al.

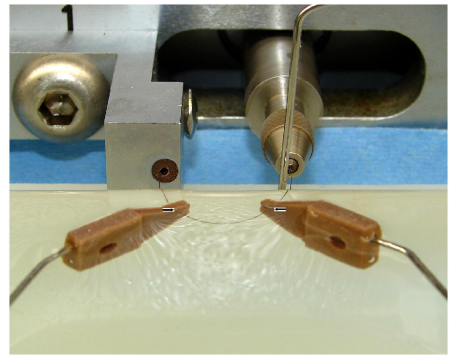

FIG. 7—*U-bend of Nitinol wire mounted within rotary chuck and bushing.*

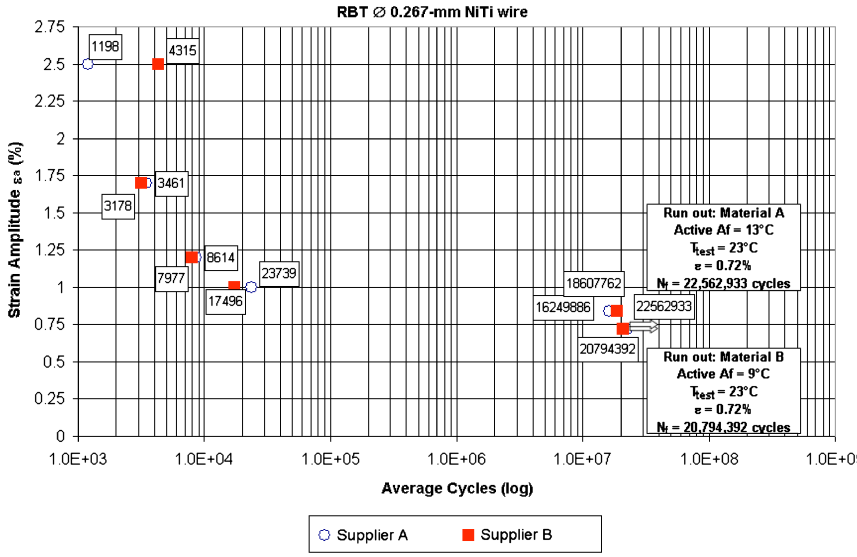

FIG. 8—*Rotary beam fatigue testing (RBT) data presented with ε-N curve with runout values noted.*

set 20 000 000 cycles, that is approximately 3.9 days, as runout [1]. In today's testing scheme, 400 million cycles (77.16 days at 3600 r/min) seems to be more representative of long-term testing. As follows in Eq 1, dimension analysis yields the number of cycles a specimen is subjected to:

$$\frac{3600 \text{ revs}}{1 \text{ min}} \cdot \frac{60 \text{ min}}{1 \text{ h}} \cdot \frac{24 \text{ h}}{1 \text{ day}} \cdot \quad \#\,\text{days} = \quad \#\,\text{cycles} \tag{1}$$

Upon completion of rotary beam testing, fractured specimens are measured for length. If fracture has occurred, and the two pieces are of unequal length, the actual stress/strain state at the point of fracture can be extrapolated. The fracture ends are then studied using SEM analysis. Miyazaki found that fractures occur at both inclusions and grain boundaries [7]. Those which nucleated at grain boundaries were found in samples of electron beam melted material.

Fractured surfaces that revealed TiC inclusions were found in material that was melted in a carbon crucible. Large stress concentrations are expected to occur at both grain boundaries as well as inclusions [7]. EDS analysis is used to determine the composition of the foreign particles.

Experimental Results

Nitinol fatigue test data are traditionally presented in the form of an ε-N (strain-life) diagram as shown in Fig. 8 [1]. The data show 20 000 000 cycles as the runout parameter. From the data shown, it is evident that both suppliers' product yielded similar fatigue life at various strain levels for 0.267-mm round wire. The dependent variable, fatigue life N_f, in cycles is plotted on the logarithmic scale abscissa. The independently controlled variable, the strain amplitude (ε_A), is plotted on the ordinate with an arithmetic scale. A regression analysis line, or similar techniques, may be fitted to the data. As the fatigue life curve approaches a slope near zero, the line now represents the fatigue limit designated as a runout. Replicate tests are designed to ensure distribution in data acquisition. This type of frequency distribution curve of fatigue lives, taken at a given strain for an array of samples, permits the variation of fatigue characteristics throughout a volume of material to be extensively studied [6].

By creating survival probability plots, one is able to determine fatigue life for a specific parameter. Figure 9 is an example of specific strain level testing. In compliance with the proximity of data points in Fig. 8, the overall apparent trend is that both suppliers exhibited similar fatigue survival probability at

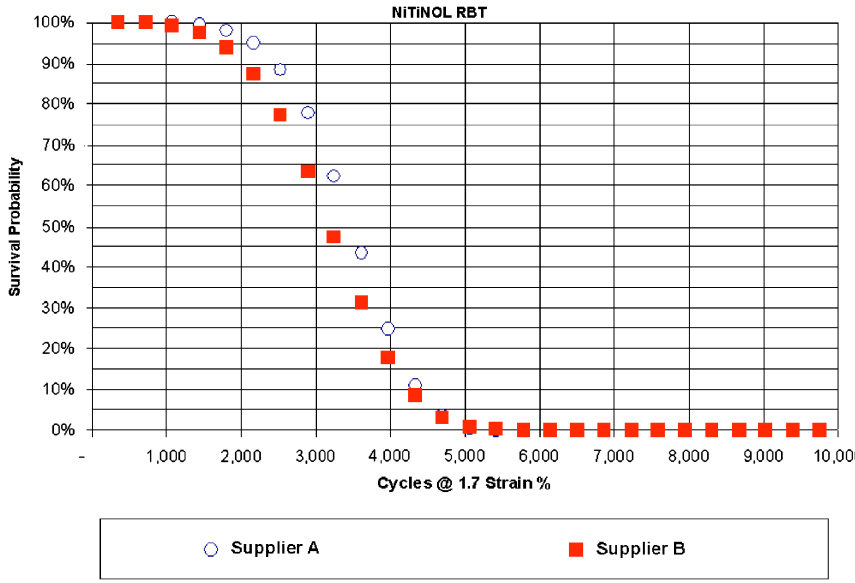

FIG. 9—*Survival plot studying 1.7 % strain amplitude.*

various cycles for 1.7 % strain. Weibull analysis is a method for modeling datasets, such as fatigue failure data. In this case, being applied to Nitinol fatigue data, Weibull analysis can be employed to determine wire endurance in use. A reliability goal must be defined properly in order to choose the ideal wire for a particular application.

Postmortem investigations of RBT samples include metallographic examination of the failed specimens; moreover, fracture surfaces may be analyzed using SEM and EDS analysis, or other comparable microscopy techniques [8]. Figures 10(*a*)–10(*e*) represent two wire segments with mating fracture surfaces; Fig. 10(*f*) displays the resulting chemical analysis of the nonmetallic inclusion found at the initiation site (marked in side A) for Supplier A. The fatigue fracture area comprised about 55 % of the wire cross section. The inclusion had an angular shape and was of approximately 4.4 μm across. Figures 11(*a*)–11(*e*) characterize the mating initiation site of an RBT wire fracture found in material from Supplier B. Furthermore, Figure 11(*f*) shows the characteristic peaks of the defective region through EDS. In this case, the fatigue fracture area comprised of 42 % of the wire cross section. The nonmetallic inclusion is located at the wire surface of the initiation site (side A) and has an angular shape of relatively 3.2 μm across. Fracture surfaces are generally on a flat and transverse plane while the stress is concentrated with striations evident in the material. For both suppliers, EDS analysis of the melt intrinsic defects indicate a variant of a titanium, carbon, nitrogen, and oxygen compound residing at the initiation zone; these results are in correlation with those found by Reinoehl. Figure 12 shows a grain boundary as the suspect stress raiser at failure found by Miyazaki [7].

Discussion

By understanding the cornerstones of material science relationships, this method of testing characterizes the interwoven properties of Nitinol alloys. Creating a designed experiment allows the examination and subsequent characterization for an array of material in the functional condition. As described, appearances of defects near the surface are easily exposed and their effects become magnified through RBT.

There is a clear dependence of stress and strain with temperature change in Nitinol. This mechanical-thermal property link is well documented by the Clausius-Clapeyron relationship:

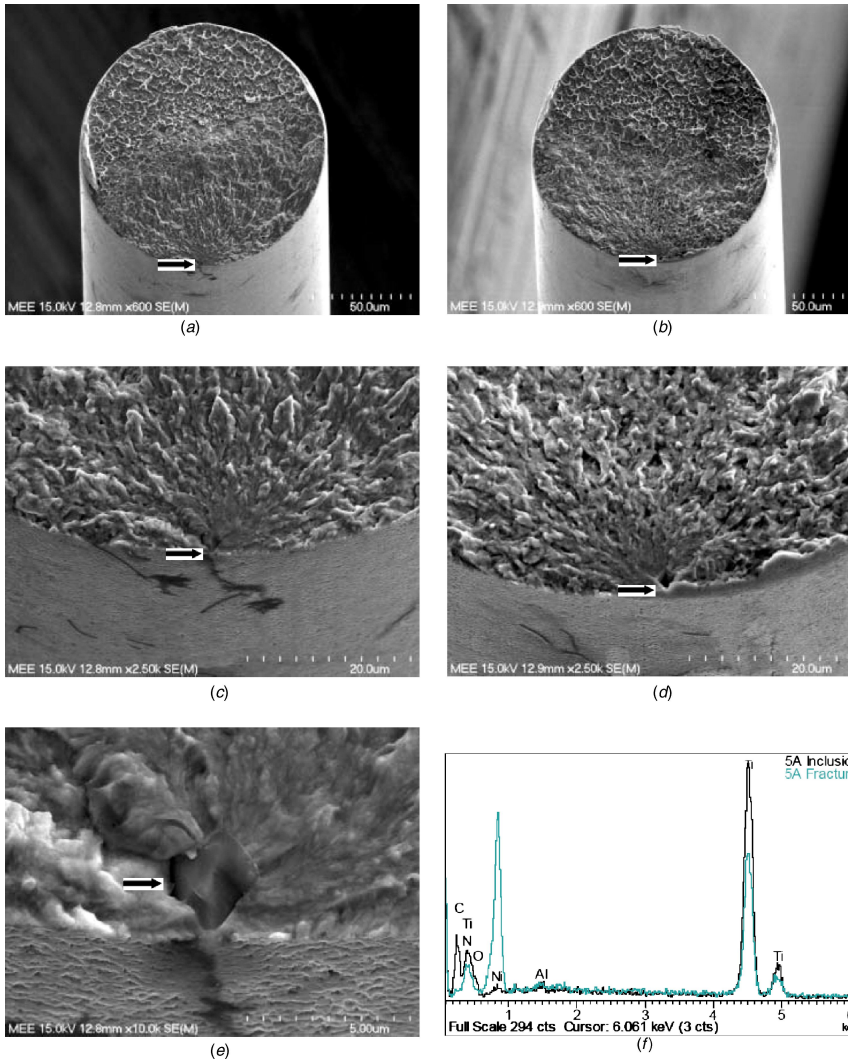

FIG. 10—*(a–e) Supplier A 0.127 mm fracture site.*

$$\frac{d\sigma}{dT} = -\frac{\Delta S}{\varepsilon} = -\frac{\Delta H}{\varepsilon T} \tag{2}$$

In this expression, σ is the uniaxial stress, ε is the transformational strain, ΔS represents the entropy of transformation per unit volume, and ΔH signifies the enthalpy of the transformation per unit volume [9]. The difference in testing temperature to Active A_f must be taken into account when heat treating samples as well as during testing. The tensile testing environment is critical; concern must be placed to ensure similar environments for RBT. After a shape-setting heat treatment, testing of the final Active A_f should be completed using a variation of the bend and free recovery test [10]. This method should be employed to provide the final Active A_f value, instead of differential scanning calorimetry. Essentially, one should aim to test with the difference in test temperature and Active A_f as shown in Eq 3 below:

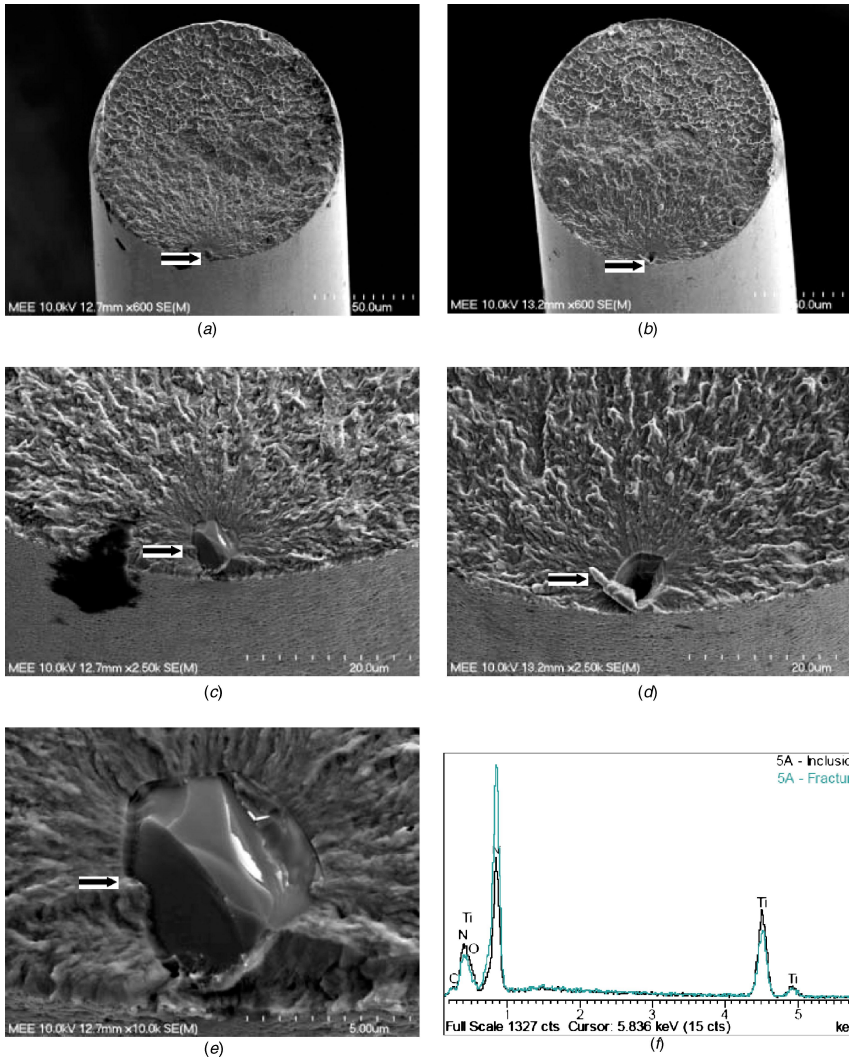

FIG. 11—*(a–f) Supplier B 0.127 mm fracture site.*

$$\Delta T = (|T_{test} - Active\ A_f|) \tag{3}$$

Prior to experimentation, test termination criterion should outline (at a minimum) temperature limits, desired cycle runout, and wire breakage.

Conclusions and Recommendations

Fatigue information is considered a steadfast means for determining wire life in dynamic utility. To serve as a quality index, the fatigue behavior profiles and endurance limit values can be obtained through RBT. Of interest to both the wire manufacturer and the consumer, RBT offers a means for production quality control and makes possible the measurement of material performance on the basis of statistical models.

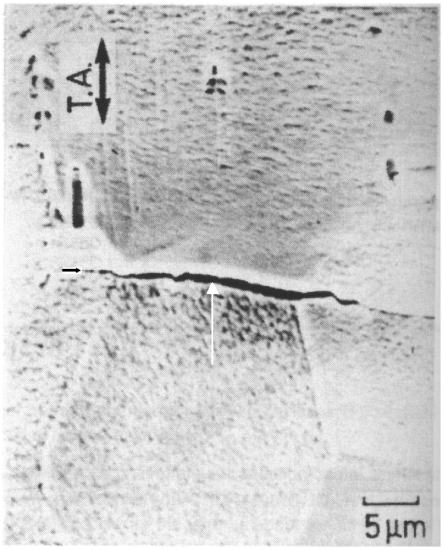

FIG. 12—*Grain boundary failure [7].*

Continuing studies should not be limited to solid NiTi wire but should encompass DFT®[2] on the single-chuck design [11]. Strands and cables should be tested on a dual-chuck system and fracture surfaces should be studied for strain distribution through the cross section. If needed in future testing, a more advanced time meter display with an extended counter would aid in prolonged studies. There is also a limitation on strain imparted and center distance due to design of machine and having difficulty reaching small chuck-to-bushing distances for very high strain levels. Some testing protocols should be designed to study crack nucleation and propagation with partial testing conducted through a fraction of the predicted material lifetime. When testing, there should be a focus on subjecting samples to strain levels above and below the approximated SIM as hinted by the onset of the upper loading plateau from the tensile test data. This value is where an expected reversible martensitic phase transformation takes place.

Particular importance should be placed on micro-cleanliness and homogenizing melt practices as inclusions were found to be possible fracture initiation points. Particle morphology may affect crack propagation behavior and should be studied in detail. A correlation study should explore the orientation of inclusion particles and how they may have an effect on fatigue life. Since grain boundaries have also been known as suspect for stress concentrations, a relationship of grain sizes and length of grain boundaries to fatigue life may be studied to attempt to draw conclusions in relation to homogeneity and possible anisotropy effects. It must be mentioned that metallurgical limitations exist due to localized transformations of the material phase as a results of sample preparation. Using FEA, one may also determine the strain conditions evident in the material prior to and during fracture using RBT. By studying the various surface finishes of Nitinol wire, a window may be opened to the medical device engineer as far as material performance goes in a tailored product.

As aforementioned, rotary beam fatigue testing setup includes the equipment setup, initial strain calculations, sample preparation, monitoring of specimens during testing, and recording length of time for the duration of the test. The number of cycles the specimen experiences is subsequently calculated, thus providing invaluable insight on material response. The fractured specimens are further characterized and fracture surfaces are evaluated. The chemical composition of extrinsic defects may shed light on upstream processing avenues.

Comprehensive fatigue test reports encompass ε-N diagrams, survival plots, and include highlights of the notable features, anomalies, and trends.

[2]DFT (Drawn Filled Tube) is a registered trademark of Fort Wayne Metals Research Products Corporation, Fort Wayne, IN.

References

[1] Reinoehl, M., Bradley, D., Bouthot, R., and Proft, J., in *SMST-2000: Proceedings of the International Conference on Shape Memory and Superelastic Technologies*, S. M. Russell and A. R. Pelton, Eds., International Organization on SMST, Pacific Grove, CA, 2001, pp. 397–403.

[2] Pelton, A., Gong, X., and Duerig, T., in *SMST-2003: Proceedings of the International Conference on Shape Memory and Superelastic Technologies*, A. R. Pelton and T. W. Duerig, Eds., International Organization on SMST, Pacific Grove, CA, 2004, pp. 293–302.

[3] Yang, J., *SMST-1997: Proceedings of the 2nd International Conference on Shape Memory and Superelastic Technologies*, A. R. Pelton, D. E. Hodgson, S. M. Russell, and T. W. Duerig, Eds., International Organization on SMST, Pacific Grove, CA, 1997, pp. 479–484.

[4] Operating manual, *Rotary Beam U-Bend Wire Spin Fatigue Tester Model 10-040*, Valley Instrument Company, Brunswick, OH, 2007.

[5] Beer, F. P., Johnston, Jr., E. R., and DeWolf, J. T., *Mechanics of Materials*, 3rd ed., McGraw-Hill, New York, 2002, pp. 213–219.

[6] ASTM Standard E 739-91, "Standard Practice for Statistical Analysis of Linear or Linearized Stress-Life (S-N) and Strain-Life (ε-N) Fatigue Data," *Annual Book of ASTM Standards*, Vol. 3.01, ASTM International, West Conshohocken, PA, 2004.

[7] Miyazaki, S., *Engineering Aspects of Shape Memory Alloys*, T. W. Duerig, K. N. Melton, D. Stöckel, and C. M. Wayman, Eds., Butterworth-Heineman Ltd., London, 1990, pp. 394–411.

[8] ASTM Standard E 606-04, "Standard Practice for Strain-Controlled Fatigue Testing," *Annual Book of ASTM Standards*, Vol. 3.01, ASTM International, West Conshohocken, PA, 2005.

[9] Otsuka, K. and Wayman, C. M., *Shape Memory Materials*, Cambridge University Press, New York, 1998, p. 25.

[10] ASTM Standard E 2082-03, "Standard Test Method for Determination of Transformation Temperature of Nickel-Titanium Shape Memory Alloys By Bend and Free Recovery," *Annual Book of ASTM Standards*, Vol. 13.01, ASTM International, West Conshohocken, PA, 2004.

[11] Schaffer, J. and Gordon, R., in *SMST-2003: Proceedings of the International Conference on Shape Memory and Superelastic Technologies*, A. R. Pelton and T. W. Duerig, Eds., International Organization on SMST, Pacific Grove, CA, 2004, pp. 109–118.

Journal of ASTM International, Vol. 3, No. 9
Paper ID JAI100388
Available online at www.astm.org

J. Eaton-Evans,[1] *J. M. Dulieu-Barton,*[2] *E. G. Little,*[1] *and I. A. Brown*[1]

Experimental Studies of NiTi Self-Expanding Stent Designs

ABSTRACT: Preliminary investigations to apply thermoelastic stress analysis (TSA) to Nitinol self-expanding stents are described. Tests conducted at high resolution indicated that a viable thermoelastic signal can be obtained from the fine stent structure. It is shown that it is possible to digitally compensate for errors arising from motion at this high resolution. High variability in Nitinol's material properties with stress and temperature result in a complex thermoelastic response. Correction strategies are proposed to account for variation in material properties and to minimize errors due to thermal variations in order to derive calibration factors for the austenite and martensite material phases. The greatest challenge is identified as calibrating the thermoelastic response from the radially loaded stent structure where it is likely the material is highly inhomogeneous.

KEYWORDS: Nitinol, thermoelastic stress analysis, stent

List of Notations

Symbol		Units
A	calibration constant	MPa/U
C_p	specific heat at constant pressure	J/kg K
E	Young's modulus	Mpa
K	thermoelastic constant	1/MPa
S	thermoelastic signal	U
T	absolute temperature	K
U	uncalibrated signal unit	…
α	coefficient of linear thermal expansion	1/K
ρ	density	kg/m^3
σ	direct stress	MPa
υ	Poisson's ratio	…

Introduction

Interventional cardiologists and vascular surgeons regard atherosclerosis as their greatest challenge. The condition is a type of vascular disease that is characterized by the focal accumulation of plaque on the inner arterial wall causing narrowing of the vessel and ischemia of local tissue [1]. The condition can occur at locations throughout the arterial network but if plaques form in vessels that supply blood to vital organs such as the heart or brain it is of greatest concern. A stenosis located in the carotid artery can cause what is known as a stroke, or similarly a stenosis located in one of the coronary arteries may lead to a heart attack. The World Health Organization (WHO) estimates that more people have died from coronary heart disease than from any other causes [2]. Hypertension, hypercholesterolemia, and cigarette smoking are considered high-risk factors, but other factors include obesity, sedentary lifestyle, stress, family history, and diabetes mellitus [3].

Manuscript received October 11, 2005; accepted for publication June 14, 2006; published online August 2006. Presented at ASTM Symposium on Fatigue and Fracture of Medical Metallic Materials and Devices on 7–11 November 2005 in Dallas, TX; M. R. Mitchell and K. L. Jerina, Guest Editors.

[1] Research Student and Professor, respectively, Department of Mechanical and Aeronautical Engineering, University of Limerick, Ireland.
[2] Reader in Experimental Mechanics, School of Engineering Sciences, University of Southampton, SO17 1BJ, UK.

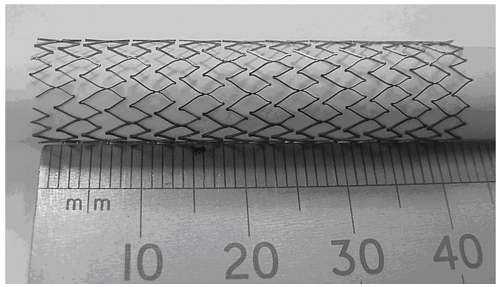

FIG. 1—*Self-expanding stent.*

The development of the percutaneous transluminal angioplasty by Grüntzig in the 1970s was a significant advancement in the treatment of atherosclerosis [4]. During an angioplasty procedure endovascular techniques are used to navigate a device known as a balloon catheter through the vascular network to the site of the occlusion. When in position the balloon is inflated to dilate the vessel and restore patency. A fine mesh cylindrical component known as a vascular stent may be implanted as a follow-up procedure to an angioplasty to act as a scaffold maintaining the patency of the vessel and reducing the risk of restenosis.

Two principal categories of stents exist: balloon expandable and self-expanding. The former are plastically deformed into position using an angioplasty balloon and are typically constructed from a stainless steel alloy. The latter, self-expanding stents (the subject of current investigations, see Fig. 1) are deployed from the tip of a catheter and expand elastically into position, providing support to the vessel wall. Self-expanding stents are constructed from a NiTi alloy commonly known as Nitinol, which has superelastic and shape memory capabilities that facilitate the elastic deployment from the catheter.

After implantation, a stent is subjected to continuous cyclic loading induced by systole/diastole blood pressure within the vessel. The medical device industry is strictly regulated and new designs must undergo lengthy fatigue testing to replicate ten years of in vivo loading [5]. Fatigue testing is a regularity requirement for FDA/CE certification and tests are conducted at accelerated rates of 40–60 Hz; lasting 16.5–11 weeks.

The current stent design process relies heavily on finite element analysis (FEA) to investigate new designs, with often the only form of validation available for these numerical models being the results of the fatigue tests. It is proposed to use thermoelastic stress analysis (TSA) [6] as a design tool that would act as a precursor to fatigue tests. Provision of a rapid analysis at the prototype stage may obviate lengthy and costly fatigue tests on designs that would ultimately fail. Furthermore, many FEA studies of stents have been carried out [7–9], without experimental validation; the TSA data could be used for this purpose. Other experimental stress analysis techniques have been considered for use with stents; however, their fine mesh construction would make it difficult to mount strain gages or produce an accurate photoelastic model. It should also be noted that other optical strain measurement techniques would not have the necessary resolution or would be unable to handle the out-of-plane deformations that the stent experiences.

TSA is a well established noncontacting technique that provides full-field stress information, [6,10]. The test specimen is cyclically loaded within its elastic range and a highly sensitive infrared detector is used to measure small changes in temperature on the surface of the specimen. Since TSA is essentially an elastic technique it is deemed suitable for the self-expanding stents as they are constructed from Nitinol, which has an extensive elastic range. Nitinol's superelastic response is, however, derived from a stress-induced crystallographic transformation from a parent austenite phase to a martensite phase. The thermoelastic response from each material phase must be characterized and the possible effect of inhomogeneities in the material during transformation must be considered.

In the current paper, preliminary work to use TSA to examine stresses in radially-loaded stents is described. Results of tests at two levels of resolution are presented and the use of motion compensation software is described. In addition, the variation in the material properties of Nitinol is discussed with view to characterization and calibration of the thermoelastic signal.

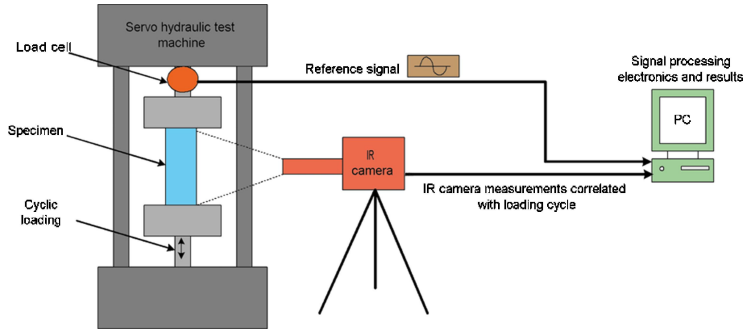

FIG. 2—*Schematic of generic TSA testing equipment arrangement.*

Thermoelastic Stress Analysis

Thermoelastic stress analysis (TSA) is a noncontacting technique providing full-field stress information [6]. The technique was developed in the mid-1980s, has been successfully applied at high resolution [11], and is suitable for analysis of complex geometries [12], making it a good candidate for stress analysis of stents.

The TSA technique is based on the well-documented thermoelastic effect [13] which states that for a linear elastic, homogeneous, isotropic material the change in temperature, ΔT, can be related to the changes in the sum of the principal stresses, $\Delta(\sigma_1+\sigma_2)$ as follows

$$\Delta T = -KT(\sigma_1 + \sigma_2) \tag{1}$$

where T is the absolute temperature and K is the thermoelastic constant, which is directly related to material properties of the body in the form

$$K = \frac{\alpha}{\rho C_p} \tag{2}$$

where α is the coefficient of linear thermal expansion of the body, ρ is the density, and C_p is the specific heat at constant pressure.

Equation 1 is derived based on the assumption that the temperature change occurs adiabatically. In practice, adiabatic conditions can be achieved (essentially) by cyclically loading the specimen at a frequency great enough to minimize heat conduction to within an area equivalent to that of a projected detector element. Typically, a cyclic frequency of 10 Hz is sufficient for most materials and stress states [14]. A further assumption is that the elastic properties (Young's modulus and Poisson's ratio) are independent of temperature. This is a reasonable assumption for most engineering materials at room temperature; however, work presented by Wong et al. [15] identified that this assumption is not valid for some titanium alloys. Nitinol is also a titanium alloy and the validity of this assumption has been examined experimentally [16] and is summarized in this paper.

TSA uses a highly sensitive infrared detection system to measure the small changes in temperature in a solid due to the thermoelastic effect. ΔT is obtained in the form of a voltage output from the infrared detector. This output signal, S, can be directly related to the sum of the changes in the principal stress on the surface of the material as follows

$$\Delta(\sigma_1 + \sigma_2) = AS \tag{3}$$

where A is a calibration constant that can be obtained experimentally [17] and is dependent on the detector properties and the properties of the material.

In the current work a Stress Photonics Deltatherm system 1400 [18] was used to collect the thermoelastic data. The system comprises a cryogenically cooled 256 by 256 Indium Antimonide photon detector array operating over a wavelength of 2 to 5 μm. A schematic of a generic TSA experimental arrangement is given in Fig. 2. A cyclic load is applied to the test specimen using a servo-hydraulic test machine. The detector system is positioned in front of the component and focused on the area of interest

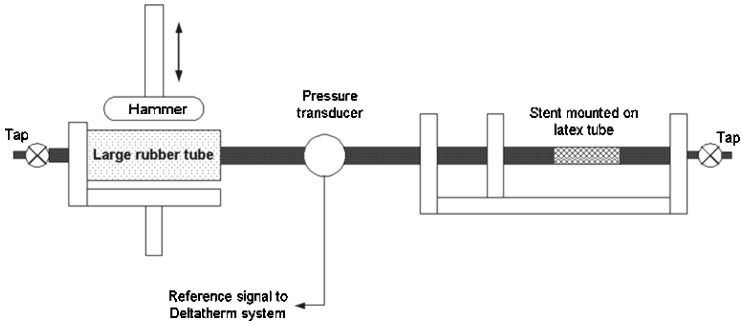

FIG. 3—*Schematic of radial loading test rig.*

using a lens system. The detector collects photons over a preset time period and simply adds up the number of photons detected over this period and normalizes them with respect to the framing rate of the system. A reference signal is obtained from the test machine load cell signal generator. The detector signal is correlated to the reference signal and rectified by the signal processing electronics. The voltage signal is then converted to a logic signal that is displayed by the computer in the form of a full-field pseudo color image of the area of interest. The correlation allows in-phase, out-of-phase, magnitude and phase data to be displayed. This means that both positive and negative stresses can be identified. Correlating the signal at the loading frequency eliminates all other inputs to the detector and permits the measurement of ΔT. This simple procedure makes TSA very attractive as high resolution images can be obtained in a matter of seconds from the actual component. The only surface preparation that is necessary is the addition of a high emissivity paint coating to specimens with reflective surfaces; this is standard practice in infrared thermography.

Experimental Arrangements for TSA of Stents

To obtain an adiabatic thermoelastic response from a test specimen it is necessary to apply a cyclic load to the stents. The stents offer no resistance to deformation axially so it was decided that a loading system, similar to that which they experience in-service, should be used. Physiological conditions can be successfully replicated by installing the stent within a mock artery and cycling the internal pressure—thereby applying an external radial load to the stent. This type of loading apparatus, however, would prevent the infrared detector from viewing the areas of interest. Therefore, to achieve the cyclic loading necessary for TSA, a test rig was designed that applied a radial internal pressure load to a stent. The rig is shown in Fig. 3 and consists principally of two latex tubes, one larger than the other. The stent was mounted on the outside of the smaller latex tube so that a load could be applied. The system was filled with water and in the process of doing so all air was bled. The large tube was compressed using a hammer mounted in a servohydraulic test machine. This action caused the smaller latex tube to expand, thereby applying a cyclic radial load to the stent. It is accepted that physiological conditions would require that the stent be mounted within the latex tube. For the purposes of this preliminary investigation it was decided to mount the stent on the outside of the tube and apply an internal pressure load to the device to examine if a thermoelastic signal could be obtained at the necessary level of resolution. Furthermore, it is proposed that if results of a FEA model of the arrangement were correlated with results obtained using TSA, then a similar model of a stent within a tube would also be valid.

The test machine control system was used to control the pressure loading rate and amplitude. However, as compressibility and lag were considered to be significant, a pressure transducer was installed in the system to provide a reference signal for the Deltatherm system and an accurate reading of the applied cyclic pressure.

The Deltatherm infrared detector was used in conjunction with a two setting zoom lens. The lens could be set so that the entire array focussed over an area 15 by 15 mm^2 corresponding to a spatial resolution of

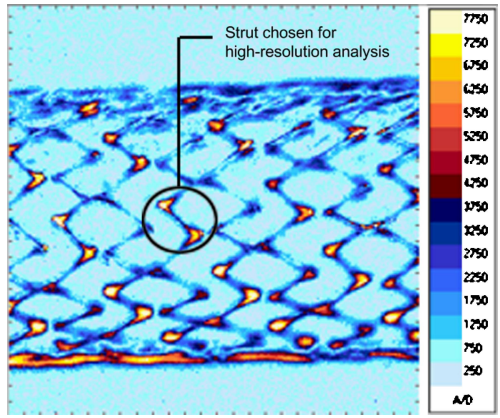

FIG. 4—*TSA image of stent under radial loading.*

3.433 μm^2 and denoted as zoom setting 1 or over an area 3 by 3 mm^2 that corresponds to a resolution of 0.137 μm^2 denoted as zoom setting 2.

Preliminary Experimental Work

Preliminary experiments were conducted to determine if it is possible to obtain a thermoelastic signal from a self-expanding Nitinol stent. As the structure of the stents is a fine mesh (see Fig. 1), resolution of the infrared optics and motion due to cyclic loading were key considerations for the preliminary studies. In this work the same stent was used during all testing and was in its expanded state. The stent was coated with two passes of RS matt black paint to provide uniform surface conditions, increase emissivity, and minimize reflection.

To begin preliminary testing, a conservative mean pressure of 0.103 MPa was first applied to the stent. Next, the pressure in the rig was cycled by displacing the hammer at increasing amplitudes to determine the required pressure range necessary to obtain thermoelastic measurements from the stent structure. Figure 4 shows an image captured for a pressure range of 0.024 MPa. The structure of the stent is clearly visible with localized areas of high thermoelastic signal (which may correspond to high stress) identifiable at the strut joins. This is as one would expect for radial loading and is encouraging. The struts situated towards the outer edges of the image appear thicker compared to those situated in the center portion of the image. This is due to effects of out-of-plane motion that are greatest at the edges of the tube for the radial loading.

A strut with a viable signal and situated in the center portion of the stent was identified for use in further higher resolution tests. Figure 5(*a*) shows a TSA image captured under identical loading pressure range as that for Fig. 4, but at zoom setting 2. On first inspection there seems to be an excellent thermoelastic signal obtained from the structure; however, closer examination indicates the signal gradient seen across the strut results from the doubling effect produced by motion. Using specialist motion compensation software built into the Deltatherm software the motion in the strut was identified as being equivalent to four pixels in an approximately up/down motion. Using the motion compensation tool, this offset was applied to the temperature plots obtained at the maximum and minimum loading cycle range using the Deltatherm system. A motion compensated version of Fig. 5(*a*) is given in Fig. 5(*b*). Much of the image doubling associated with the movement of the stent has been abbreviated but some does remain in the elbow region. The radial loading applied to the stent produced a complex movement pattern that makes full motion compensation difficult, but a significant improvement has been achieved. It is important to note that recalibration of the thermoelastic signal is required after motion compensation has been undertaken. This is because the motion compensation process works on two single datasets rather than the addition of those accumulated over a period of time. This requires further investigation and at present it is sufficient to highlight that the scale in Fig. 5(*b*) is not comparable to previous images.

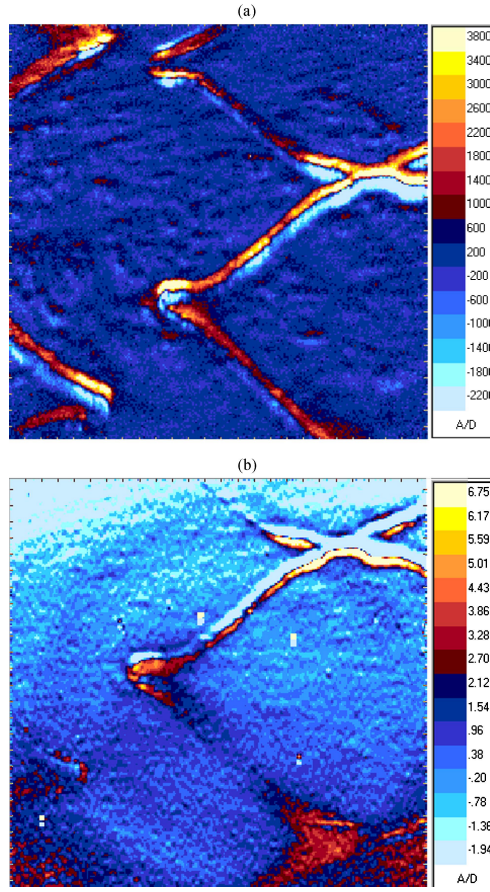

FIG. 5—*High resolution TSA image of stent. (a) Before motion compensation. (b) After motion compensation.*

This part of the work has clearly shown that it is possible to obtain a thermoelastic response from the fine mesh structure of the stents and some interesting qualitative data have been obtained. It is now necessary to investigate the possibilities of obtaining quantitative stress data from Nitinol stents. This will require a calibration routine to be developed and is the object of the following section.

Thermoelastic Characterization of Nitinol

Equation 1 is developed for a linear elastic material; however, Nitinol is a nonlinear elastic material with both superelastic and shape memory capabilities. Nitinol's material properties are temperature dependent and stress dependent; therefore, it is the purpose of this section of work to determine if Eq. 1 can be used to approximate the stresses in the stents or if a new thermoelastic formulation is required to interpret the data.

The properties of Nitinol vary widely between different grades of the material and with different heat treatment processes. Thermoelastic characterization was conducted on tubes of Nitinol that are used to manufacture the stents tested. This material had been heat treated to exhibit a high-temperature austenite microstructure at room temperature and superelastic properties at body temperature to facilitate deploy-

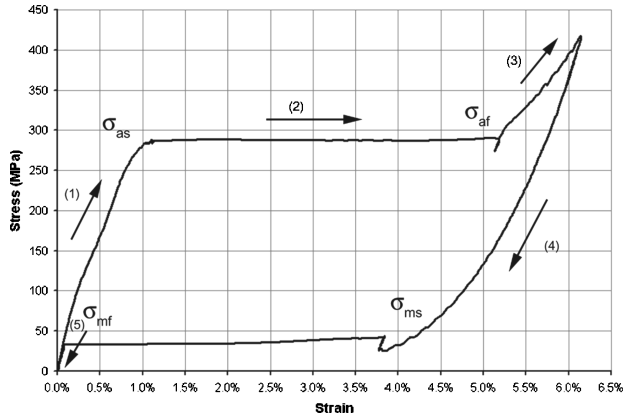

FIG. 6—*Nitinol nonlinear elastic stress-strain curve.*

ment of the device from the catheter. TSA was conducted on stents at room temperature and therefore the material characterization was also conducted at room temperature.

The manufacturer provided tubes of the stent material with an outside diameter of 3 mm and an internal diameter of 2.5 mm. It was decided to perform mechanical tests under quasistatic and cyclic axial tension loading to characterize the Nitinol. The tubes were cut into 150-mm lengths and were reinforced at either end by inserting steel rods of 25-mm length to prevent crushing in the test machine grips. Tests were conducted using an Instron servohydraulic test machine. Measurements of load were taken using a 0–10 kN load cell and strains were obtained using an extensometer.

To identify the transformation stresses specimens were mounted in the test machine and loaded to 420 MPa. Figure 6 shows the typical stress-strain relationship for the material. The transformation stresses were approximated from these data and are given in Table 1.

Upon loading the material initially behaves in a linear elastic manner while in its austenite phase (1) (see Fig. 6). As the stress is increased, the material begins a transformation into a martensite phase characterized by a plateau where the material has a low Young's modulus (2). The transformation stresses during this phase—σ_{as}, austenite start, and σ_{af}, austenite finish, are given in Table and are indicated in Fig. 6. During this transformation period the material undergoes substantial strains (in the order of 5–6 %) within a small range of stress. When the transformation to martensite is completed the material behaves in a linear elastic manner until a yield point is reached and plastic deformation occurs before failure (3). However, if loading is removed before yield the strain incurred is reversible. Transformation back to austenite occurs at a lower stress (4) and the material returns to a zero stress state with practically no permanent deformation along a closed stress-strain hysteresis loop (5). The transformation phase is indicated in Fig. 6 by σ_{ms}, martensite start, and σ_{mf}, martensite finish, with values seen in Table 1. Clearly Nitinol does not behave as a standard engineering material and therefore must be fully characterized thermoelastically prior to embarking on providing any quantitative data.

Preliminary TSA investigations were carried out with the material loaded in the austenite and martensite regions. Figures 7(*a*) and 7(*b*) show TSA images obtained from Nitinol tubes loaded in the austenite and martensite regions, respectively, while the material experiences a cyclic stress of 46 MPa. These images both show a uniform thermoelastic signal; however, the response is approximately 33 % greater in the austenite phase. Figure 7(*c*) shows a TSA image collected for a Nitinol specimen loaded during transition [location (2) shown in Fig. 6]. During transformation the material is inhomogeneous and the propagation of martensite bands is visible. These Lüder-like formations occur only when the material is

TABLE 1—*Transformation stresses at 20°C.*

Austenite to Martensite		Martensite to Austenite	
σ_{as}	286.9 (MPa)	σ_{ms}	30.4 (MPa)
σ_{af}	289.1 (MPa)	σ_{mf}	32.4 (MPa)

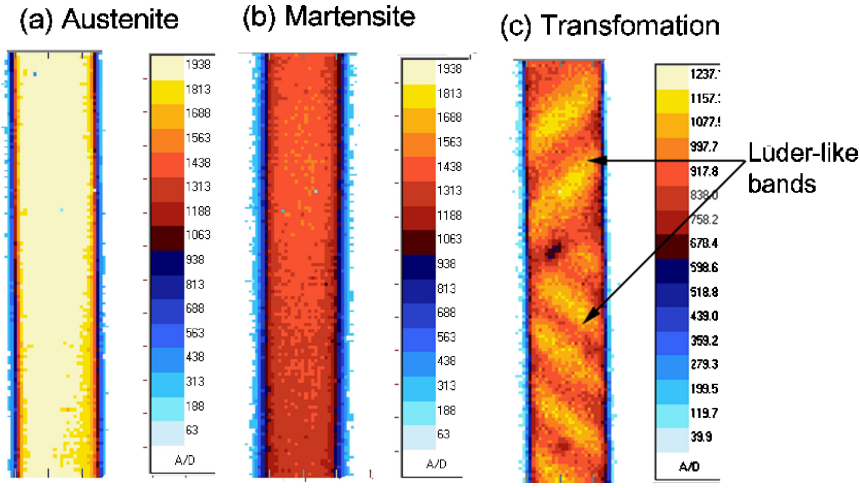

FIG. 7—*Nitinol thermoelastic response when loaded in (a) austenite phase, (b) martensite phase, and (c) during transformation.*

loaded in tension and are a well documented [19] transformation characteristic; however, as is evident in Fig. 7(*c*), the thermal variation associated with the bands affects the thermoelastic response. From Fig. 7 it can be seen that the response is different in all three regions and, therefore, interpretation of thermoelastic data from a structure such as a stent requires careful analysis. It is encouraging that the austenite region and the martensite region provide a uniform signal; however, each phase produces a different response for the same applied stress range. Therefore, knowledge of the material phase characteristics present throughout the loaded structure is necessary to interpret the thermoelastic response and derive quantitative stress data. Clearly, any data obtained from a material undergoing a transition will be unreliable.

From observing Fig. 6 it can be seen that the stress-strain response is approximately linear in regions (1) and (4). To investigate the linearity of the thermoelastic response a preliminary test was conducted in region (1)—the austenite phase, for a Nitinol specimen loaded in simple tension. The mean stress has held constant and the cyclic amplitude was incrementally increased in the range 10–100 MPa. The thermoelastic response is directly proportional to the applied stress range (Eq. 3) and the experimental results shown in Fig. 8 confirm this relationship.

In developing Eq. 1, the temperature dependence of the elastic constants was neglected and thus an expression that shows that ΔT is dependent on the stress changes alone is obtained. A significant consideration is that Young's modulus for austenitic Nitinol is highly dependent on temperature. An increase in temperature results in an increase in the concentration of austenite present and corresponding increase in the magnitude of the E value. It has been shown [20] for some engineering materials loaded to their elastic

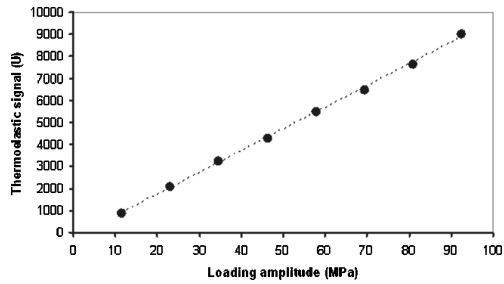

FIG. 8—*Linear relationship between thermoelastic signal and loading amplitude for the austenite phase.*

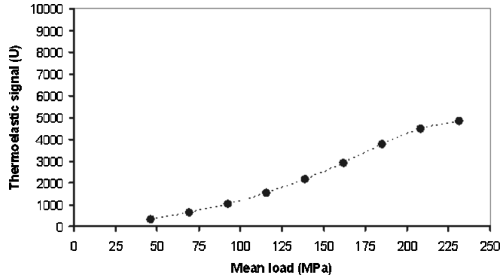

FIG. 9—*Mean load dependence of thermoelastic signal in the austenite phase.*

limits there is a dependence of the thermoelastic response on the mean stress as well as the applied stress range. Wong et al. [21] presented a revised theory that includes the mean stress term. For a uniaxial loading system the theory can be stated as follows

$$\Delta T = -\frac{T}{\rho C_\varepsilon}\left(\alpha - \frac{1}{E}\frac{\partial E}{\partial T}\sigma_m\right)\Delta\sigma \tag{4}$$

where σ_m and $\Delta\sigma$ are the mean value and the range of the applied stress cycle and $\partial E/\partial T$ is the change in Young's modulus with temperature.

In order to investigate the mean load dependence of Nitinol a specimen was loaded with constant stress range at increasing mean loads from 46 to 230 MPa. The response of the material is shown in Fig. 9. A significant mean stress dependence is evident as the material is loaded through the austenite range with an approximate increase in signal of 26.1 U per 1 MPa increase in mean stress.

To further investigate the mean stress effect a series of uniaxial tensile tests were conducted at increasing temperature in the austenite phase to derive a value for the change in Young's modulus with temperature. The results are shown in Fig. 10 and indicate that there is a significant relationship at room temperature (approximately 2230 MPa/°C), but that the relationship is nonlinear and at temperatures above 30 °C where the material approaches its fully austenitic state and the magnitude of the $\partial E/\partial T$ term decreases.

Wong et al. [22] demonstrated that Eq. 4 can satisfactorily account for the relationship between the thermoelastic signal and the mean stress for a range of engineering materials. Further analysis has been conducted to examine if Eq. 4 is valid for Nitinol [16]. In summary, it has been shown that the mean stress dependence seen in Nitinol is a result of the variation of the material's Young's modulus with temperature.

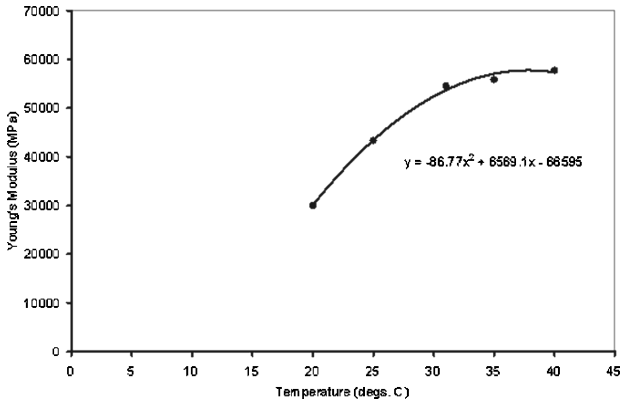

FIG. 10—*Variation of E with temperature in the austenite phase.*

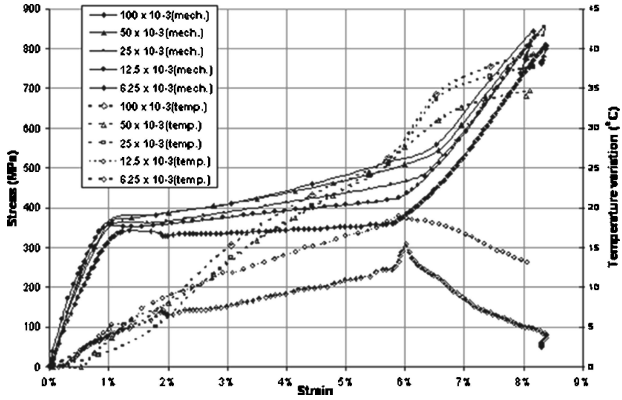

FIG. 11—*Strain rate dependence and associated thermal variation during loading.*

The effect may be eliminated by conducting tests at elevated temperatures (corresponding approximately to body temperature); however, this is currently under investigation and will be the subject of future publications.

A further consideration that must be accounted for is the thermal variation associated with the microstructure phase change. Temperature increases on the order of 30°C are possible during stress-induced martensite formation [23]. The temperature variation is repeated during unloading to austenite; however, during the reverse transformation it is endothermic in nature. The magnitude of thermal variation is strain rate dependent with less variation occurring at low strain rate as more time is available for thermal diffusion. This is illustrated in Fig. 11 where uniaxial tensile tests were conducted on a Nitinol specimen at increasing strain rates and thermal variation across the strain range is plotted. Critically thermal variation is present in the austenite region as the loading approaches the transformation stress. It is likely that this is due to heat released by localized transformation prior to departure to the transformation plateau region.

Work conducted by Emery et al. [24] examined the effect of heating caused by viscoelasticity in cyclically loaded composite specimens on the thermoelastic signal. It was demonstrated that the heating effects could be effectively corrected out using a correction factor R defined as

$$R = \left(\frac{T_0}{T} \right)^n \tag{5}$$

where T_0 and T are the absolute temperature prior to heating and the current specimen temperature, respectively, and n is a constant dependent on the detector properties (for the Deltatherm system it has been numerically approximated to 11.16 [25]). A correction factor could be developed to account for heating generated by localized transformation in the austenite/martensite phases. This is the subject of current investigations.

Conclusions

A successful preliminary study of the application of TSA to Nitinol self-expanding stents has been carried out. Tests on a stent loaded with an internal stress found that it is possible to obtain meaningful high resolution thermoelastic data from Nitinol stents. Further work is required to compensate fully for the effects of motion but preliminary results are encouraging.

Calibration of Nitinol's thermoelastic response across its nonlinear elastic loading range was considered and correction strategies were presented for errors due to variation in material constants with temperature and thermal variations not associated with the thermoelastic effect. It may be possible using these correction regimes to derive calibration constants for both austenitic and martensitic forms of the material

but it is unlikely that TSA can be successfully applied during the material transformation phase due to the inhomogeneous properties of the material and the significant heating (or cooling) effects associated with the transformation.

The greatest challenge, however, lies in the interpretation of the thermoelastic signal from a radially loaded stent, as it is unclear at what radial load and where in the stent structure martensite formation will begin to occur. It is likely that martensite will form locally at high stress points, making calibration of the resulting inhomogeneous structure a very complex challenge. Possible strategies to surmount this problem include controlling loading to prevent martensite formation or possibly heat treating the material to maximize the transformation stress and inhibit martensite formation; this is the subject of current work.

Acknowledgments

This work was funded by the Irish Research Council for Science Engineering and Technology (IRCSET) under the Embark Initiate. The Deltatherm system used in this work was loaded from the UK Engineering and Physical Sciences Research Council (EPSRC) equipment loan pool.

References

[1] DePalma, R. G., "Atherosclerosis—Pathology, Pathogenesis and Medical Management," *Vascular Surgery*, W. S. Moore, Ed., Saunders Co., Philadelphia, 1998, pp. 85–93.

[2] Mackey, J., and Mensah, G., *The Atlas of Heart Disease and Stroke*, World Health Organization publications, Washington, DC, 2004, p. 48.

[3] Fuchs, J. C., "Atherogenesis and the Medical Management of Atherosclerosis," *Vascular Surgery*, R. B. Rutherford, Ed., W. B. Saunders, Philadelphia, 1995, pp. 222–233.

[4] Gruntzig, A. R., "Percutaneous Transluminal Coronary Angioplasty," *Vascular and Interventional Radiology*, 3rd Ed., Adams, H. L. Ed., Little, Brown and Co., Boston, 1983, pp. 2087–2097.

[5] European Standard EN12006-3, "Nonactive Surgical Implants—Particular Requirements for Cardiac and Vascular Implants—Part 3: Endovascular Devices".

[6] Dulieu-Barton, J. M., and Stanley, P., "Development and Applications of Thermoelastic Stress Analysis," *J. Strain Anal. Eng. Des.*, Vol. 33, No. 2, 1998, pp. 93–104.

[7] Etave, F., Finet, G., Boivin, M., Boyer, J. C., Rioufol, G., and Tollet, G. J., "Mechanical Properties of Coronary Stents Determined by Using Finite Element Analysis," *J. Biomech.*, Vol. 34, No. 8, 2001, pp. 803–811.

[8] Migliavacca, F., Petrini, L., Colombo, M., Auricchio, F., and Pietrabissa, R., "Mechanical Behavior of Coronary Stents Investigated Through the Finite Element Method," *J. Biomech.*, Vol. 35, No. 6, 2002, pp. 803–811.

[9] Tan, L. B., Web, D. C., Kormi, K., and Al-Hassani, S. T., "A Method for Investigating the Mechanical Properties of Intracoronary Stents Using Finite Element Numerical Simulation," *Int. J. Cardiol.*, Vol. 78, No. 1, 2001, pp. 51–67.

[10] Pitarresi, G., and Patterson, E. A., "A Review of the General Theory of Thermoelastic Stress Analysis," *J. Strain Anal. Eng. Des.*, Vol. 38, 2003, pp. 405–418.

[11] Calvert, G., Smith, G., and Thomson, B., "The Use of Thermoelastic Stress Analysis to Identify Defects in Polymeric Materials," *Insight*, Vol. 46, No. 9, 2004, pp. 550–553.

[12] Refior, H. J., Schidlo, C., Plitz, W., and Heining, S., "Photoelastic and Thermoelastic Measurement of Stress on the Proximal Femur Before and After Implantation of a Hip Prosthesis with Retention of Femoral Neck," *Orthopedics*, Vol. 25, No. 5, 2002, pp. 505–511.

[13] Thomson, J. R., (Lord Kelvin), "On the Dynamical Theory of Heat," *Trans. R. Soc (Edinburgh)*, Vol. 20, 1853, pp. 261–283.

[14] Quinn, S., and Dulieu-Barton, J. M., "Identification of the Sources of Non-adiabatic Behaviour for Practical Thermoelastic Stress Analysis," *J. Strain Anal. Eng. Des.*, Vol. 37, No. 1, 2002, pp. 59–71.

[15] Wong, A. K., Jones, R., and Sparrow, J. G., "Thermoelastic Constant or Thermoelastic Parameter," *J. Phys. Chem. Solids*, Vol. 48, 1987, pp. 749–753.

[16] Eaton-Evans, J., Dulieu-Barton, J. M., Little, E. G., and Brown, I. A., "Thermoelastic Studies on Nitinol Stents," *J. Strain Anal. Eng. Des.*, in press.

[17] Dulieu-Smith, "Alternative Calibration Techniques for Quantitative Thermoelastic Stress Analysis," *Strain*, Vol. 31, 1995, pp. 9–16.

[18] Lesniak, J. R., Boyce, B. R., and Sandor, B. I., "Thermographic Stress analysis/NDE Via Focal Plane Array Detectors" NASA Contract Report CR-NASA-19262, 1991.

[19] Sittner, P., Liu, Y., and Novak, V., "On the Origin of Luder-Like Deformation on NiTi Shape Memory Alloys," *J. of Mech., and Phys. of Solids*, Vol. 53, 2005, pp. 1719–1746.

[20] Machin, A. S., Sparrow, J. G., and Stimson, M.-G., "Mean Stress Dependence of the Thermoelastic Constant," *Strain*, Vol. 23, 1987, pp. 27–29.

[21] Wong, A. K., Jones, R., and Sparrow, J. G., "Thermoelastic Constant or Thermoelastic Parameter," *J. Phys. Chem. Solids*, Vol. 48, 1987, pp. 749–753.

[22] Wong, A. K., Sparrow, J. G., and Dunn, S. A., "On the Revised Thermoelastic Effect," *J. Phys. Chem. Solids*, Vol. 49, 1988, pp. 395–400.

[23] Pieczyska, E. A., and Nowacki, W. K., "Thermomechanical Aspects of Martensite and Reverse Transformations—TiNi Shape Memory Alloys Subjected to Tension," *12th International Conference on Experimental Mechanics*, Bari, Italy, McGraw Hill, 2004, pp. 685–686.

[24] Emery, T., Dulieu-Barton, J. M., and Cunningham, P. R., "Identification of Damage in Composite Structures Using Thermoelastic Stress Analysis," *6th International Conference on Damage Assessment of Structures*, Gdansk, Poland, Key Engineering Materials, 2005, pp. 583–590.

[25] Dulieu-Barton J. M., Quinn S., Eyre, C., and Cunningham, P. R., "Development of a Temperature Calibration Device for Thermoelastic Stress Analysis," *Applied Mech., and Mat*, Vol. 1, No. 2, 2004, pp. 197–204.

Journal of ASTM International, Vol. 3, No. 6
Paper ID JAI100384
Available online at www.astm.org

Kenneth J. Cavanaugh, Jr.,[1] *Vivianne M. Holt,*[2] *Jennifer L. Goode,*[1] *and Evan Anderson*[3]

FDA Recommendations for Nitinol Stent and Endovascular Graft Fatigue Characterization and Fracture Reporting[1]

ABSTRACT: Intravascular stents and endovascular stent-grafts provide a minimally invasive option for treating vascular disease and injury. Medical device manufacturers typically conduct radial pulsatile fatigue testing of intravascular stents and endovascular grafts to demonstrate that these devices will maintain their durability for ten years of implant life. While they are useful indicators of device performance, these test regimens do not always predict device durability in the clinical setting with perfect accuracy. In this paper, we address some of the common issues that should be considered in the design of fatigue tests, including appropriate sample sizes for fatigue testing, sample selection, loading conditions, and test setup issues. We also discuss finite element analysis of long-term cyclic fatigue. In addition, we describe appropriate methods for reporting the incidence of stent fractures after implantation. Our goals are to assist manufacturers and test laboratories in refining their in vitro fatigue testing methods to allow more accurate prediction of clinical device fractures, and to maximize the amount of useful data contained in clinical fracture reports.

KEYWORDS: medical device, stent, stent-graft

Introduction

The use of intravascular stents is one of the cornerstones of modern endovascular intervention. A typical stent consists of a metal substrate such as stainless steel or a nickel-titanium alloy (nitinol), and is designed to provide structural support and to improve the luminal patency of blood vessels. Stent designs vary in complexity from cylindrical braided wire meshes to laser-cut, drug-coated slotted metal tubes. Physicians also regularly implant endovascular stent-grafts, which are stents covered with a fabric shell to create a synthetic lumen for blood flow in vessels that have been damaged due to aneurysms, dissections, or other injuries. Both stents and stent-grafts allow treatment of vascular disease and improvement in blood flow with less morbidity and risk than open surgical repair.

Engineering and *in vitro* bench testing can be important indicators of stent and stent-graft performance in the implanted state, especially with respect to device durability. Clinical observations of device durability are also important tools for assessing improvements to device designs. Despite the utility of these assessment methods, not every testing facility or physician conducts these evaluations in an optimal manner. In this paper, we hope to clarify our perspective on finite element analysis (FEA), fatigue testing, and fracture reporting for nitinol stents and endovascular grafts, as gained from the review of applications to the U.S. Food and Drug Administration (FDA). Unless otherwise indicated, use of the word "stent" in this paper refers to both uncovered vascular stents and the metal stent components of endovascular stent-grafts.

In general, we believe that test reports submitted to the FDA should include at least as much detail as

Manuscript received November 9, 2005; accepted for publication March 11, 2006; published online April 2006. Presented at ASTM Symposium on Fatigue and Fracture of Medical Metallic Materials and Devices on November 7–11, 2005 in Dallas, TX; M. R. Mitchell and K. L. Jerina, Guest Editors.

[1] Biomedical Engineers, Division of Cardiovascular Devices, Office of Device Evaluation, Center for Devices and Radiological Health, U.S. Food and Drug Administration, Rockville, MD 20850.

[2] Mechanical Engineer, Division of Cardiovascular Devices, Office of Device Evaluation, Center for Devices and Radiological Health, U.S. Food and Drug Administration, Rockville, MD 20850.

[3] Medical Device Fellowship Program Participant, Division of Cardiovascular Devices, Office of Device Evaluation, Center for Devices and Radiological Health, U.S. Food and Drug Administration, Rockville, MD20850. Current affiliation: Research Engineer, Guidant Corporation, Santa Clara, CA 95054.

[1]The views presented in this paper are those of the authors and do not necessarily reflect the views of the U.S. Food and Drug Administration as an agency.

test results submitted to a peer-reviewed journal. The information should be of sufficient detail that a person knowledgeable in the field could duplicate the tests and come to the same conclusions as the authors. The sections of this paper following the introduction point out some of the areas that manufacturers and testing laboratories should consider in any detailed report of fatigue and FEA analysis for stents, whether that report is for the FDA or meant for publication to a wider audience. This paper is not meant to be a comprehensive analysis of issues associated with fatigue and FEA testing of nitinol stents; we intend merely to point out some common areas of concern for the FDA and for industry in medical device submissions. There are many other issues that should be considered when developing a stent testing program, and anyone embarking on such a task should consult with relevant subject matter experts for advice.

It should be noted that this paper is only intended to address aspects of mechanical testing of the nitinol stent substrate and not with the issues surrounding any coatings or drugs that might be applied to the stent. In coronary applications, it appears that drug-eluting stents have replaced bare metal stents as the primary stenting option, but the safety and effectiveness issues associated with mechanical performance of the bare metal substrate still exist and should be evaluated for any stent system.

A Brief Overview of Intravascular Stenting

According to most accounts, stents derive their name from Dr. Charles Stent, an English dentist who invented a dental impression compound in 1856. Similar compounds were later used for various purposes such as rebuilding of damaged tissues. The first recorded use of the term "stent" in its "modern" form dates to 1916 [1]. Current intravascular stent designs were first developed by Dr. Charles Dotter in the 1960s and later by Dr. Julio Palmaz in the 1980s. Stents have been used in human arteries since the 1980s [2], and the first self-expanding nitinol stent was implanted in the human cardiovascular system in the early 1990s [3]. Covered stent-grafts with nitinol components have been in human use since the 1980s.

A typical use of intravascular stents is treatment of stenoses, which are narrow places in blood vessels. The desired result of stent implantation is generally increased blood flow through the stenotic region. In addition, stents are placed in certain vessels, most notably the carotid arteries in the neck, to decrease the risk of particle embolization from the stenosis by both covering the particle-producing lesions and potentially by reducing the flow velocity through the stenosis. Embolized particles can obstruct blood flow downstream and result in ischemic injury to important end organs, such as the brain or kidneys.

Stents are placed in the body using a "minimally invasive" approach. The stent and its associated delivery system are typically threaded through an incision in the groin area into the vasculature and are tracked over a wire to the region of interest. Once in place, the stent is deployed using one of two methods. Balloon-expandable stents are premounted onto a balloon catheter, and during deployment the balloon is expanded to plastically deform and release the stent. Alternatively, self-expanding stents, most often constructed of nitinol, are originally radially compressed and held in place on the delivery system via a sheath. This type of stent is deployed by releasing the sheath, whereupon the stent expands elastically until it conforms to the vessel wall. Once the stent is deployed, the delivery system is removed.

Due to their superelastic properties, nitinol stents are resistant to crushing and plastic deformation. As a result, nitinol stents are commonly used to treat stenoses in anatomic locations in which the stent is likely to be flexed or crushed, such as in the legs and in the carotid arteries. By contrast, balloon-expandable stents are primarily used in the coronary vasculature and other areas where they are not expected to encounter such forces, such as the renal arteries.

History of the FDA Stent Guidance

The FDA did not publish a guidance document or a draft guidance document for testing of stents until May 1995, at which time a draft guidance was produced that contained a section on stent testing. This draft guidance was recently removed from the FDA web site (www.fda.gov). In January 2005, the FDA published a new guidance specific to nonclinical testing and labeling of intravascular stents and their associated delivery systems [4]. This guidance was developed based on the FDA's experience with review of stents in the ten years since the draft guidance was published. The guidance includes recommendations for testing of nitinol stents, including recommendations for testing and reporting of nitinol material properties.

The following sections describe some considerations when reporting the results of fatigue and FEA testing of nitinol stent and endovascular grafts. Most of these considerations are true for any stent or graft with metallic components; however, this paper is intended to show how such reporting can be tailored to nitinol implants.

Durability Testing Considerations

Sample Sizes for Durability Testing

Stents are commonly tested in durability testers that can hold anywhere from one to approximately 24 specimens. Sample size is a critical issue due to the cost of the testers and the cost of running tests on large quantities of devices over the necessary extended periods of time, which can be as long as 3–4 months for some devices. Stents that experience a typical durability test either break or crack during the run, or stay intact until the end of the test run. Cracks that do not propagate through the entire width of the strut may or may not be considered failures, depending on the test parameters and the indicated use of the device. Such go/no go results mean that data from a durability test can be considered as attribute (pass/fail) data. For this case, a passing result would be recorded if the stents are intact after cycling that approximates ten years of implant life (e.g., 400 million cycles might approximate ten years of pulsatile flow, if this is the primary loading condition on the stent). Means and standard deviations cannot be calculated from the test results because the results are in the form of a binomial distribution. In other types of test applications, binomial results can be evaluated using the statistical concepts of confidence and reliability. However, use of such a method in this case would necessitate an impractically large sample size. For example, if one wanted to run a test whose results would, if there were no failures, result in a 95 % confidence and 99 % reliability that the failure rate of the batches of stents represented by samples is less than 1 %, one would need to test 298 samples [5]. Given that it will usually not be possible to test such a large number of samples, the challenge for the experimentalist is to determine a sample size that provides some insight into the behavior of the stent, while understanding the limitations of a go/no go test using a limited number of specimens.

It is important for the experimentalist to consider the results of other tests, such as animal studies and finite element analyses, when attempting to interpret the results of a durability test on a small number of samples. Failure of a stent during durability testing may indicate the need for further evaluation, although, with a small number of samples, lack of failures does not guarantee the robustness of the device. This is especially true for nitinol where finishing techniques can greatly affect the durability of the device.

Sample Selection

As mentioned above, durability testing of finished products is especially critical for nitinol stents because they are prone to surface crack formation during initial processing, and unfinished nitinol has low fatigue resistance compared to other implantable metal alloys [6]. In addition, machining can leave behind surface stress concentrations and slag that contribute to poor fatigue life. These imperfections often can be mitigated by polishing. Therefore, it is important to test nitinol stents that have been finished per finalized manufacturing instructions to ensure that the manufacturing process is adequate with respect to making stents that have a smooth surface with as few crack initiation sites as possible. It is also important to include a full discussion of the effects of all manufacturing and finishing processes on the durability test results of a nitinol stent design in the final test report.

Loading Conditions

Nitinol stents are commonly used in various vascular beds, including the carotid, femoral, femoropopliteal, renal, and iliac arteries. Each of these anatomic locations, and even the individual lesions, presents different mechanical challenges. The lower limbs may be particularly difficult, as evidenced by recent articles regarding the incidence and clinical effects of stent fractures in the femoropopliteal artery [7,8].

The loading conditions present in proposed clinical stent deployment locations should be carefully considered when designing a nitinol stent durability test. The oversizing of the stent to the arterial wall and

the worst-case strains with respect to fatigue life should be considered. The experimentalist should carefully consider the strain amplitude that is applied to the stent and decide whether it reflects real-life conditions [9].

Durability Test Setup Issues

The stent testing community has not yet optimized fatigue test methods that consider certain potential loads and boundary conditions present in the intended use, such as stent overlapping and flexure, for general application, such as in a published international standard. Durability testing of nitinol stents is often particularly difficult because these stents are primarily used in implant locations where they are subjected to a multitude of nonradial loads such as axial tension, compression, bending, and torsion. No perfect test setup exists for modeling all anatomically relevant fatigue loading conditions. All of the existing tests have advantages and disadvantages depending on the environment one wishes to test. Ideally, engineers should account for their inability to mimic *in vivo* conditions by ensuring that their test setups challenge the devices using more rigorous conditions than are likely to be found in the body. Doing so requires the engineer to determine the most critical fatigue loading conditions and to model them. The conditions that need to be modeled will vary depending on the intended anatomic location or locations of the subject device.

In addition to modeling worst case *in vivo* conditions, durability testing of stent-grafts requires attention to specific issues related to the design of the metallic components and their physical relationship to the nonmetallic portions of the graft and the testing machine. For example, a sample of a stent-graft design that includes barbs will either need to be modified to prevent the barbs from prematurely eroding fixture tubing in a standard pulsatile radial fatigue test, or a different test fixture for the device will need to be designed that can properly test an unmodified sample to the desired number of cycles without excessive wear to the test fixture.

Finite Element Modeling of Long-Term Cyclic Fatigue

In the January 2005 stent guidance, the FDA recommends that submissions for nitinol stents include a finite element model of the stent that evaluates both acute (predeployment crimping and deployment in a vessel) and long-term (fatigue over ten years) failure modes. The results of such modeling can be used to support the results of bench testing and to provide additional assurance of the ability of the device to withstand fatigue during its expected life.

Material Inputs

The strains, stresses, and safety factors calculated from an FEA model are only as good as the model inputs. Important inputs to consider and report on include, but are not limited to, appropriate characterization of material properties (including austenitic finish temperature [A_f], stress-strain curve, temperature-dependence of properties, and hysteresis), the exact geometry including an accurate strut profile or reasoning why the given geometry is accurate enough to allow fatigue characterization of the device, the element type, and the number of elements in the model. It is particularly important to ensure that the model contains a sufficient number of elements to converge to a single accurate mathematical solution.

There are several ASTM standards that can aid in development of material inputs, such as ASTM Standard Specification for Wrought Nickel-Titanium Shape Memory Alloys for Medical Devices and Surgical Implants (F 2063). It is important to consider the limitations of the tests used to gather material properties when running a finite element model. For example, the difference between material properties gathered from a thin nitinol wire and the actual properties of a nitinol stent that is cut from a hypotube and then expanded, annealed, and applied to a delivery system can be considerable, as these manufacturing steps can significantly affect the long-term fatigue life of the device. It is important that the FEA test report acknowledges the limitations of the tests used to gather the material properties.

FEA Model Verification and Validation

The analyst should consider reporting all validations and verifications of the model, because such activities increase confidence in the model's ability to mimic real-life stent performance. It should be noted that verification and validation, while similar in their scopes and goals, are in fact different processes that should both be conducted for every analysis performed.

Verification of a finite element model involves testing the FEA program using benchmark problems to ensure that the FEA code provides accurate results. Best engineering practice is to verify any FEA program through the use of simple benchmark models before investing time and other resources on development of a sophisticated model of a stent. Verification is most crucial when using a custom code, especially when dealing with the intricacies of modeling nitinol. Off-the-shelf codes may not need such extensive verification by the end user, but it is important to mention in the FEA test report any previous verifications by the software developer of which the analyst is aware.

Validation involves testing the FEA model of the stent deployment history to ensure that the model accurately represents the actual history of a stent deployed in the body. Validation of FEA models for nitinol stents is critical, because modeling programs and programmers vary in their ability to adequately capture the unique properties of nitinol. As of this writing, not all of the commercially available FEA programs include code written to specifically model nitinol. It is important for the analyst to consider whether a particular FEA program can produce a reasonably accurate representation of the behavior of a nitinol medical device before committing to use of the program.

In addition to these steps, the analyst should fully understand the sources of error present in both the modeling program and the model before attempting to make meaningful conclusions from the results of the analysis.

FEA Model Outputs and Calculation of Safety Factors

The FEA test report should include a clear description of the FEA model outputs with a discussion of how the FEA results support the durability of the device. FEA model outputs can take many forms: equivalent strains/stresses, principal strains/stresses, or von Mises stresses at specific locations on the stent are commonly reported. Once the model is run and results extracted, safety factors can be calculated and presented both as numerical values in tabular format and in comparison to a constant-life curve formulated from an appropriate stress-based or strain-based relationship. Color plots of the critical area of the stent are helpful to show the locations at which fatigue is most likely to occur under extreme conditions. The critical locations determined from the FEA and the safety factors can then be compared to the results of bench-top fatigue testing.

Reporting of Stent and Stent-Graft Fractures

Advantages of Clinical Fracture Reporting

While preclinical testing is a valuable tool for characterizing the performance of a medical device, it alone is not a definitive method to predict device durability. The *in vivo* milieu often cannot be completely reproduced on the bench due to limitations in equipment or measurement methods, or due to incomplete knowledge of the chemical and mechanical stresses that affect an implanted device. Therefore, it is also important to examine the clinical performance of an implant to determine whether it can withstand the physicochemical environment present at the intended implant location for a reasonable amount of time.

Device durability is especially sensitive to physiological challenges. *In vitro* testing of these parameters often does not fully model the complexities of the *in vivo* mechanical environment, resulting in test conditions that can produce informative, but not entirely biofidelic, data. For example, as mentioned above, the superficial femoral artery may experience significant tension, compression (both axial and radial), torsion, and bending every day [7,8]. In addition, other peripheral vessels such as the carotid and renal arteries have been shown to undergo significant nonradial deformations under normal conditions [10,11]. Despite this published evidence, such loading conditions are not always considered in a typical fatigue test for a device intended for use in these locations.

While more complete modeling of loading conditions during benchtop durability testing is one way to obtain a more accurate estimate of the fatigue life of a stent, often times these loading conditions are not definitively known, especially for relatively complex stenting indications such as in the superficial femoral artery. Even in established anatomic locations for which the mechanical environment is more well known, such as the coronary vasculature, stent fractures can still occur in devices that have successfully passed benchtop fatigue testing [12]. With these considerations in mind, a complementary method of assessing the

TABLE 1—*Appropriate elements of a clinical fracture report.*

Type of Information	Examples
Identity of patient	Patient identifier number
Time of fracture detection with respect to implantation	12 months post-implantation
Imaging modality used to detect fracture	Flat-plate X-ray; IVUS
Identity[a] of fractured stent	…
Vessel in which device was implanted	Left internal carotid artery; saphenous vein graft
Other implants present (identity,[a] location, and size)	Overlapped stent; 1 cm left limb extender
Device location within vessel, referencing landmarks	1 cm distal to bifurcation
Number of observed fractures	Single strut; multiple struts
Locations of observed fractures	2 mm from distal end; 2 mm from overlapped region
Types of observed fractures	Transverse; spiral
Any observed stent dislocation	2 mm gap observed between stent segments at fracture
Diagram of device showing fracture locations	…
Reportable clinical events	Stent migration
Clinical sequelae	Restenosis; myocardial infarction; aneurysm
Explant information, if available	…

[a]Include manufacturer, model, and size (including length and diameter).

as-implanted durability of the device is to monitor the incidence and location of device fractures in implanted stents. If sufficiently detailed, this information should provide the manufacturer with real-world feedback on how the stent performs in its as-implanted state when subjected to the repeated and complex deformations imposed by real-world conditions.

Fracture Reporting for Stents

A clinical fracture report should provide appropriate background regarding the implantation, characterize the location and extent of the fracture (including narrative and diagrams), and describe any consequences of the fracture. Table 1 contains a list of some types of relevant information that can be included in fracture reports. Depending on the nature of the device, inclusion of additional information or nonreporting of certain data elements may be appropriate. For example, endovascular grafts used to treat abdominal aortic aneurysms are often modular in nature, and the configuration of all ancillary implanted devices used to treat the aneurysm should be described. Additional types of information may also be appropriate for coated products, including drug-eluting stents.

Fracture reports based on multiple incidences of stent fracture in a clinical study should also include a table that identifies the number of patients at risk during each follow-up interval specified in the clinical protocol. In addition, for each follow-up interval, the number of patients with reported fractures and the number of fractures should be reported. For this information, both cumulative and newly reported fracture data should be reported separately.

Optimal reporting of stent and stent-graft fractures can be a powerful tool in stent and stent-graft design. The real-world feedback offered by clinical data can help the research engineer to improve device durability and enhance the relevance of benchtop fatigue test methods.

Conclusion

While often similar in principle, stent and stent-graft designs vary greatly in design and mechanical and clinical performance. Although accurate assessment of the durability of these devices can be a challenge, proper fatigue testing, finite element analysis, and fracture reporting help ensure that only safe and effective designs reach consumers.

References

[1] Ring, M. E., "How a Dentist's Name Became a Synonym for a Life-Saving Device: The Story of Dr. Charles Stent," *J. Hist. Dent.*, Vol. 49, No. 2, 2001, pp. 77–80.

[2] Zollikofer, C. L., Antonucci, F., Stuckmann, G., Mattias, P., and Solomonowitz, E. K., "Historical Overview on the Development and Characteristics of Stents and Future Outlooks," *Cardiovasc.*

Intervent Radiol., Vol. 15, 1992, pp. 272–278.

[3] Beyar, R., Henry, M., Shofti, R., Grenedier, E., Globerman, O., and Beyar, M., "Self-Expandable Nitinol Stent for Cardiovascular Applications: Canine and Human Experience," *Cathet Cardiovasc. Diagn.*, Vol. 32, No. 2, 1994, pp. 162–170.

[4] FDA Guidance on Non-Clinical Tests and Recommended Labeling for Intravascular Stents and Associated Delivery Systems, URL: http://www.fda.gov/cdrh/ode/guidance/1545.pdf, 1 November 2005.

[5] Natrella, M. G., *Experimental Statistics*, Dover Publications, 2005.

[6] McKelvey, A. L. and Ritchie, R. O., "Fatigue-crack Propagation in Nitinol, a Shape-memory and Superelastic Endovascular Stent Material," *J. Biomed. Mater. Res.*, Vol. 47, No. 3, 1999, pp. 301–308.

[7] Scheinert, D., Scheinert, S., Sax, J., Piorkowski, C., Braunlich, S., Ulrich, M., Biamino, G., and Schmidt, A., "Prevalence and Clinical Impact of Stent Fractures After Femoropopliteal Stenting," *J. Am. Coll. Cardiol.*, Vol. 45, No. 2, 2005, pp. 312–315.

[8] Duda, S. H., Bosiers, M., Lammer, J., Scheinert, D., Zeller, T., Tielbeek, A., Anderson, J., Wiesinger, B., Tepe, G., Lansky, A., Mudde, C., Tielemans, H., and Beregi, J. P., "Sirolimuseluting Versus Bare Nitinol Stent for Obstructive Superficial Femoral Artery Disease: The SIROCCO II Trial," *J. Vasc. Interv Radiol.*, Vol. 16, No. 3, 2005, pp. 331–338.

[9] Pelton, A. R., Gong, X-Y., and Duerig, T., "Fatigue Testing of Diamond-Shaped Specimens," *Proceedings of the International Conference on Shape Memory and Superelastic Technologies (SMST)*, May 2003, pp. 293–302.

[10] Draney, M. T., Zarins, C. K., and Taylor, C. A., "Three-dimensional Analysis of Renal Artery Bending Motion During Respiration," *J. Endovasc. Ther.*, Vol. 12, 2005, pp. 380–396.

[11] Floris Vos, A. W., Linsen, M. A. M., Marcus, J. T., van den Berg, J. C., Vos, J. A., Rauwerda, J. A., and Wisselink, W., "Carotid Artery Dynamics During Head Movements: A Reason for Concern with Regard to Carotid Stenting?," *J. Endovasc. Ther.*, Vol. 10, 2003, pp. 862–869.

[12] Chowdhury, P. S. and Ramos, R. G., "Coronary-stent Fracture," *N. Engl. J. Med.*, Vol. 347, 2002, p. 581.